University of California
Santa Barbara

Floquet Engineering with Ultracold Lithium in Optical Lattices

A dissertation submitted in partial satisfaction
of the requirements for the degree

Doctor of Philosophy
in
Physics

by

Kevin Singh

Committee in charge:

Professor David Weld, Chair
Professor Andrea Young
Professor Chetan Nayak

March 2019

The Dissertation of Kevin Singh is approved.

Professor Andrea Young

Professor Chetan Nayak

Professor David Weld, Committee Chair

January 2019

Floquet Engineering with Ultracold Lithium in Optical Lattices

by

Kevin Singh

To my mother

Jo Bole So Nihal ... Sat Sri Akal!

Acknowledgements

First things first, I must thank my parents. The two of you taught me the importance of willpower and work ethic. Applying these two traits has been the key to progress throughout my entire life and especially during graduate school. Furthermore, I can't possibly thank you enough for immigrating to this country and giving me the opportunity to climb the ladder of the American dream.

When I first joined the Weld lab, I was given a simple mission: to amplify. This mission applied to all aspects of the laboratory including but not limited to constructing AOM drivers to amplify radio-frequency signals, building tapered amplifiers to amplify laser light, and working on my personality to amplify the culture of the Weld lab. All of this culminated in my four senior students giving me a nickname: Increase.

If I have been able to see further and *increase* our understanding of the unknown, it is only because I stand on the shoulders of the original four giants: Zach, Ruwan, Shankari, and Cora. The four of you taught me the fundamentals of atomic physics. I have wonderful memories of Zach teaching me about lasers and electronics, Ruwan teaching me about optics and Hubbard models, Shankari teaching me about optical fibers and vacuums, and Cora teaching me about magnetic and optical traps (after all, what is a spatially dependent energy but a trap?). I've had so many hilarious and fun moments with each of you that have made graduate school an amazing experience. Zach - that time we spent an entire week only communicating to each other in our highest possible Mickey Mouse voices helped me to forget about our struggles trying to optically plug the magnetic trap. I think that was also around the same time we started religiously listening to Justin Bieber's Purpose album. Ruwan - I'll never forget the time you and I cleaned out the inside of the water chiller and got covered in brown slime. As they say, if you're brown make a sound. Also, I'll always remember that time we got our hands

on that Wannier function code and we basically spent a week plotting wave functions and calculating tunneling rates for different lattice depths for fun. Good times. Shankari - I'll never forget the time you were assembling the strontium chamber and taught me how to tighten CF flanges for the first time. Star pattern! Also thank you for sharing my love of Drake and Beyonce songs. After you introduced me to DJ Khaled's Shining ft. Jay Z & Beyonce, I listened to it non-stop for a month. It's still in my workout playlist. Also, you have an uncanny ability to exert exactly 144 in-lbs of torque without the use of a torque wrench. If that's not spooky action at a distance I don't know what is. Cora - You are the F to my S. I'd like to take this moment to *not* apologize for all the times I said "I don't know, can I?" after you would ask me to do something starting with "Can you...". Your Matlab skills are intimidating and your ability to rapidly calculate Floquet quasienergy spectra even more so. I'll never forget the time you modified the analysis code so that after every experimental run the speakers would randomly blast popular phrases such as "It's over 9000!" or "For you" or "Yeah" in the style of Lil Jon. But of all the memories I have from graduate school, the one I remember most vividly is the night all of us celebrated getting our first lithium BEC and our first strontium BEC within two weeks of each other. That feeling of triumph after years of struggling in the dark is the greatest feeling I've ever felt. I am beyond honored to have shared that with all of you.

Peter Dotti. Peter - I have yet to determine which one of us is actually real. Am I your imaginary friend or are you mine? Are we the same person? I will always cherish the numerous gedanken experiments we've had. Thank you for teaching me about Jones matrices and for working with me to understand Landau-Zener transitions. I wish you the best as you work to study the Kitaev Hamiltonian with an army of ducks. If anyone can do it, it's me....er...you?...I forget who's who.

Misha Lipatov. Misha - Over the course of two years of data taking, I think you and

I watched literally every gym fail video on YouTube. I won't ever forget our numerous discussions about proper posture, martial arts, and orienteering. I wish you the best as you continue your physics journey outside of atomic physics and as you master Aikido.

Toshihiko Shimasaki. Okay, I would like to take this moment to publicly apologize for all the times I tried to get a rise out of you by saying: "I wish Masayuki was my post-doc." Toshi, you're the best post-doc and housemate ever. Thank you for teaching me about doublets, phase lock loops, fast PIDs, solid state lasers, molecular photoassociation, buffer gas cooling, EDM experiments, rubidium, cesium, and everything else I forgot to include in this list. You're like a walking, talking, atomic physics encyclopedia. You'll be my [Optimum Nutrition] gold standard as I move on to become a post-doc as well.

Ethan Simmons. Quinn - I can't wait to see all the great things you're going to do on the lithium machine. It's only your second year and you've built a feedback circuit for the strontium magnets, figured out how to operate the digital mirror device, built an oven nozzle and performed an oven bake. I've really enjoyed talking to you about bichromatic driving and topological frequency conversion. Keep on rocking it. I know you will.

Roshan Sajjad. Our time together has been very short, but I'm excited to see you start your atomic physics journey! I'm not sure which of the experiments you'll be working on, but don't hesitate to adapt either machine to study physics that you're interested in! The beauty of these machines is that you can study a wide variety of physics with a combination of courage and the appropriate laser potential.

Alec Cao and Max Prichard. As Max would say, it has been such a pleasure working with you two. Alec - you've done an amazing job learning how to run and take data with the lithium machine. Max - you've done an amazing job building a laser tapered amplifier. I have no doubt the two of you will go on to do big things!

One of the best parts of being a graduate student has been working with many

excellent undergraduates who are now graduate students themselves: Eli Wolf, Krutik Patel, Ian Harley, Jacob Hines, Morgan Brubaker, Shuo Ma, James Chow, Yi Zeng, and Sean Frazier (though technically you were a post-bac). Each one of you would give me a burst of energy and optimism whenever you walked into the laboratory and I'm positive each of you is doing great in your graduate research.

André Eckardt and Markus Heyl. Thank you for teaching me about dynamical quantum phase transitions, periodic Gibbs ensembles, and prethermalization. I very much enjoyed all of our early morning Skype conversations and discussions. The two of you are absolutely brilliant. Be sure to keep checking your email inboxes. I'll be sending you guys more atomic physics data soon!

One thing I love about the UCSB physics department is the collaborative spirit between the various experimental physics groups. I can't count the number of times I've hopped over to the Mazin lab or the Sherwin lab or the Young lab or the Bouwmeester lab or the Jayich lab or the other Jayich lab to ask for advice, electronics, optics, or stupidly large metric screws. I have to give a special thanks to the Sherwin lab. The Weld lab graduate students and the Sherwin lab graduate students have been getting lunch together every Monday through Friday at 11:30 am for nearly four years now. Thank you guys for teaching me everything about free-electron lasers, terahertz science, and electron paramagnetic resonance. I have to give another special thank you to the Young lab students. They have been organizing a journal club every Friday where all graduate students can come together and discuss the most exciting recent results in condensed matter and atomic physics related fields. Also thank you to Andrea for being on my committee! And since we're talking about committee members, thank you Chetan for being on my committee and letting me pass out of statistical mechanics my first year as a graduate student. You really helped me jump straight into research!

Being a graduate student working on an atomic physics experiment requires signifi-

cant support from the purchasing department, building staff, and administrative offices. Thank you to Dave Prine, Dan Stack, Erin Ferguson, Dan Daniels, Lynne Leininger, Holly Woo, and Eva Deloa for always working to put our orders out as fast as possible. Thank you to Mike Deal, the building manager, for working tirelessly around the clock to keep everything in the building operating smoothly. I know all the recent forest fires and power outages have made life incredibly stressful for you. Also thank you to Jennifer Farrar, the graduate student administrator, for cheerfully helping every graduate student navigate through all the phases and paperwork associated with graduate school.

I decided I would save the best for last: Dr. David Weld. Thank you for introducing me to the wonderful world of atomic physics and to the beauty of quantum emulation. You taught me that cold atoms can be used as a tool to emulate the physics of condensed matter systems. The beauty of quantum emulation is not that it recreates the physics of condensed matter systems, but that the emulation serves as a starting point to then explore into the unknown. Because of this, I've noticed a paradigm shift in how I approach physics. I'm constantly trying to think of new ways to bridge my understanding between vastly different fields of physics. I owe this new vantage point to you. Putting the science aside, you have been an incredible advisor. You are compassionate, fair, idealistic, and kind - all qualities I aspire to have. I have had two moments in my time as a graduate student when I felt that the world was coming down around me. Both of these times I met with you in your office and you gave me the advice I needed to hear to get myself back on track. The world needs more people like you, sir. I'm honored to have been your graduate student and I'm excited to spend the rest of my life reaching for new heights in my understanding of the world. And with that, sir, all I have left to say is: "Pardon my reach."

Curriculum Vitæ

Kevin Singh

Education

2019	Ph.D. in Physics (Expected), University of California, Santa Barbara.
2016	M.A. in Physics, University of California, Santa Barbara.
2013	S.B. in Physics, Massachusetts Institute of Technology

Publications

Controlling and characterizing Floquet prethermalization in a driven quantum system. K. Singh, K. M. Fujiwara, Z. A. Geiger, E. Q. Simmons, M. Lipatov, A. Cao, P. Dotti, S. V. Rajagopal, R. Senaratne, T. Shimasaki, M. Heyl, A. Eckardt, and D. M. Weld. arXiv:1809.05554 (2018).

Transport in Floquet-Bloch bands. K. M. Fujiwara, K. Singh, Z.A. Geiger, R. Senaratne, S. V. Rajagopal, M. Lipatov, and D.M. Weld. *Phys. Rev. Lett.* **122**, 010402 (2019).

Observation and Uses of Position-space Bloch Oscillations in an Ultracold Gas. Z. Geiger, K. M. Fujiwara, K. Singh, R. Senaratne, S. V. Rajagopal, M. Lipatov, T. Shimasaki, R. Driben, V. V. Konotop, T. Meier, and D. M. Weld. *Phys. Rev. Lett.* **120**, 213201 (2018).

Quantum Simulation of Ultrafast Dynamics Using Trapped Ultracold Atoms. R. Senaratne, S. V. Rajagopal, T. Shimasaki, P. E. Dotti, K. M. Fujiwara, K. Singh, Z.A. Geiger, and D.M. Weld. *Nature Communications* **9**, 2065 (2018).

Experimental Realization of a Relativistic Harmonic Oscillator. K.M. Fujiwara, Z.A. Geiger, K. Singh, R. Senaratne, S.V. Rajagopal, M. Lipatov, T. Shimasaki, and D.M. Weld. *New J. Phys.* **20**, 063027 (2018).

Quantum Emulation of Extreme Non-equilibrium Phenomena with Trapped Atoms. S.V. Rajagopal, K.M. Fujiwara, R. Senaratne, K. Singh, Z.A. Geiger, and D.M. Weld. *Ann. Phys.* **529**, 1700008 (2017).

Fibonacci Optical Lattices for Tunable Quantum Quasicrystals. K. Singh, K. Saha, S.A. Parameswaran, and D. M. Weld. *Phys. Rev. A* **92**, 063426 (2015).

Search for a Light Higgs boson in the Z boson plus a Photon Decay Channel. Bornheim, A. et al. CMS Physics Analysis Summary, CMS PAS HIG-12-049 (2012).

Abstract

Floquet Engineering with Ultracold Lithium in Optical Lattices

by

Kevin Singh

Floquet engineering is a versatile tool that uses periodic driving of a quantum system to build novel many-body quantum states with drive-dependent properties. In this thesis I will detail experiments performed in the Weld group which explore a many-body Floquet system consisting of tunably-interacting ultracold atoms in an optical lattice amplitude-modulated at up to a thousand percent. I will discuss experiments in which we use Floquet engineering to coherently control long-range quantum transport in hybridized Floquet-Bloch bands. I will also discuss our use of a double quench protocol to experimentally control and quantitatively characterize Floquet prethermalization associated with a periodic generalized Gibbs ensemble.

Contents

Chapter 1

Introduction

"Never trust an atom, they make up everything." - Anonymous

The experimental study of atoms played an enormous role in developing the foundations of modern quantum mechanics [1]. Every student of modern physics can remember the feeling of triumph when first applying the fundamentals of quantum mechanics to solve the hydrogren atom. Today, rather than studying atoms themselves, there is significant effort in using ensembles of atoms to construct phases of matter that have never been observed before. With quantum mechanics in hand, scientists and engineers have developed technologies that allow experimentalists the ability to manipulate atoms with extraordinary precision and control [2, 3]. In particular, with the development of laser technology, atoms can now be cooled to a billionth of a degree above absolute zero [4]. In this ultracold regime, a predominately quantum mechanical theory is necessary to explain observed phenomena, enabling experiments that continue to push the boundaries of our quantum mechanical understanding. Additionally, using electric and magnetic fields, an experimentalist can tune the properties of the atoms and engineer exotic many-body quantum systems [5, 6, 7, 8, 9, 10], allowing investigation of new problems and the

discovery of unknown physics.

Dilute atomic gases can be trapped in a wide variety of optical traps [6]. It is now common practice to trap atoms in standing waves of laser light called optical lattices. There has been significant effort to use ultracold atoms in optical lattices to emulate the physics of the Hubbard model, which is a Hamiltonian used in solid-state physics to describe transitions between conducting and insulating systems. One of the major milestones in the ultracold atomic physics context of the Hubbard model was the observation of the superfluid to Mott insulator transition using bosonic rubidium atoms in an optical lattice in 2002 [11]. In addition to bosons, fermions can also be laser cooled to produce degenerate Fermi gases. A recent experiment demonstrated many-body localization [12], which is the disorder induced localization of interacting particles, using ultracold interacting fermions in a quasiperiodic lattice. Presently, one of the hottest topics in atomic physics is in the application of quantum gas microscopes. Quantum gas microscopes are experiments where a high-resolution imaging system is used to image single lattice sites and single atoms in an optical lattice [13, 14].

In this thesis, I will discuss the steps taken in my time as a graduate student to trap and laser cool lithium atoms into the ground states of optical lattice potentials. The central tool in all of the experiments in this thesis is a lithium Bose-Einstein condensate (BEC) [15, 16, 17]. Bose-Einstein condensates give atomic physicists the ultimate control over the kinetic degrees of freedom of atoms. Namely, producing a BEC allows us to load a cloud of bosons directly into the absolute ground state of a variety of potentials. A list of all elements that have been cooled to Bose-Einstein condensation to date is shown in Figure 1.1. A BEC arises purely due to bosonic quantum statistics and can be understood as a thermal phase transition in equilibrium statistical mechanics. Because BECs are very well understood in the context of equilibrium statistical mechanics, they serve as excellent launching points to study non-equilibrium physics. In particular, a

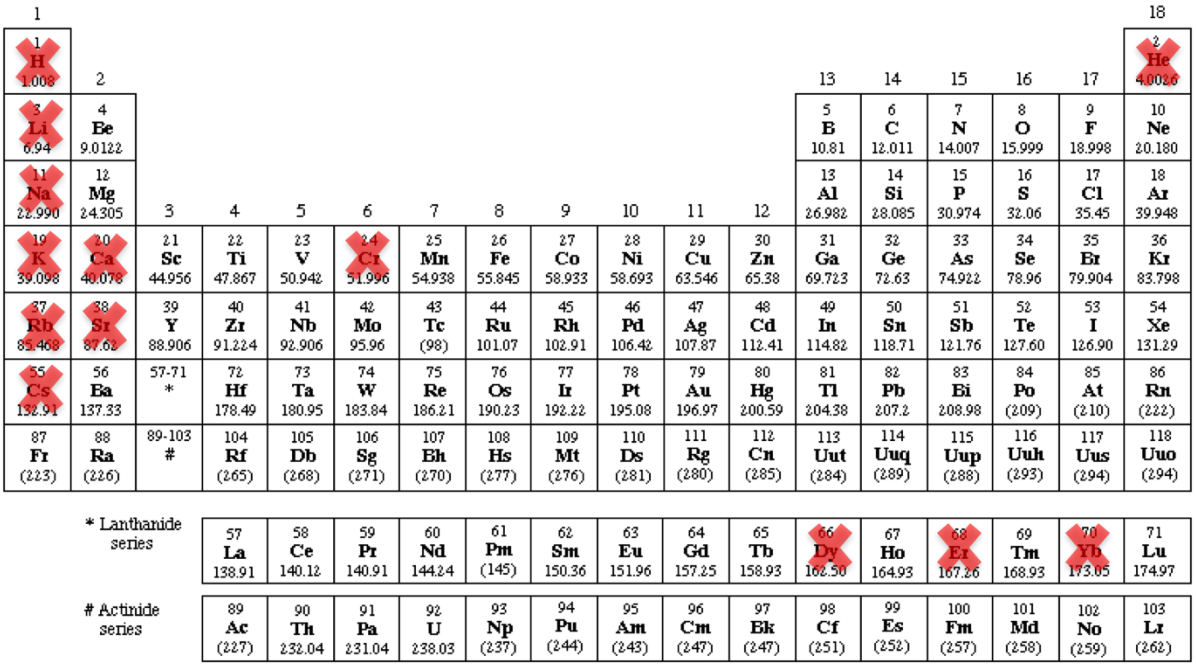

Figure 1.1: The periodic table of elements. Red Xs indicate elements that have been cooled to Bose-Einstein condensation at the time of this writing.

natural way to extend equilibrium statistical mechanics into the non-equilibrium case is with the addition of a periodic drive. Much of this thesis will be devoted to our use of periodic modulation of trapping potentials to engineer new quantum-mechanical behavior of our atoms. Engineering performed in this way is called Floquet engineering.

Lithium is a great choice for studying many-body quantum systems. Lithium is an alkali atom. It has two stable isotopes: ^{7}Li (a boson) and ^{6}Li (a fermion). Because lithium has a low mass, quantum dynamics and tunneling happen quickly on experimental time scales. Additionally, atomic lithium has several accessible optical transitions. The first two excited states have linewidths of roughly 6 MHz. The transition from the ground states to the first excited states is at 671 nm, which is an optical transition and is visibly red, making it easier to align the laser light needed to cool and trap lithium. There are plenty of solid state laser diodes available at 671 nm which means an experimentalist can construct an apparatus with plenty of laser power for an affordable

price. But arguably the most important attribute of lithium, and the feature that makes it worth all the trouble of making a machine that Bose-condenses it, is its broad magnetic Feshbach resonance [18]. The magnetic Feshbach resonance allows an experimentalist to tune the s-wave scattering length of atoms between strongly-interacting, non-interacting, and strongly repulsive regimes with relative experimental ease. The appeal of strongly interacting gases is not only to provide models for many-body systems, but to also allow investigation of new problems and discover unknown physics in the context of strongly correlated quantum matter.

In the next chapter, I will provide a brief review of the usual constructs of statistical mechanics and explain how to extend the concepts of thermalization to periodically driven systems using Floquet states and a time-periodic Gibbs ensemble. In chapters 3 and 4, I will discuss the laser cooling sequence and the experimental apparatus we use to cool ^{7}Li to Bose-condensation. In chapter 5, I will outline several experiments that demonstrate our ability to controllably engineer and manipulate Floquet states. In chapter 6, I will detail experiments that use strong periodic driving to construct periodic generalized Gibbs ensembles that are associated with Floquet prethermalization. In chapter 7, I will philosophize about exciting future directions and research avenues for the lithium experiment.

1.1 Permissions and Attributions

1. Much of the theoretical content of Chapters 2 and 3 is adapted from the following excellent textbooks: *Atomic Physics* by Christopher Foot, *Bose-Einstein Condensation in Dilute Gases* by C.J. Pethick and H. Smith, *Statistical Physics of Particles* by M. Kardar, and *Quantum Theory of Many-Particle Systems* by A. L. Fetter and J. D. Walecka.

2. Some of the content of chapter 5 is the result of a collaboration with C. J. Fujiwara, Zachary Geiger, Ruwan Senaratne, Shankari V. Rajagopal, Mikhail Lipatov, Toshihiko Shimasaki, Rodislav Driben, Vladimir V. Konotop, Torsten Meier, and David M. Weld and several of the figures have previously appeared in *Phys. Rev. Lett* [19]. They are reproduced here with the permission of *Phys. Rev. Lett*: `https://journals.aps.org/prl/abstract/10.1103/PhysRevLett.120.213201`.

3. Some of the content of chapter 5 is the result of a collaboration with C. J. Fujiwara, Zachary Geiger, Ruwan Senaratne, Shankari V. Rajagopal, Mikhail Lipatov, and David M. Weld and several of the figures have previously appeared in *Phys. Rev. Lett* [20]. They are reproduced here with the permission of *Phys. Rev. Lett*: `https://journals.aps.org/prl/abstract/10.1103/PhysRevLett.122.010402`.

4. The content of chapter 6 is the result of a collaboration with C. J. Fujiwara, Zachary Geiger, E. Q. Simmons, M. Lipatov, A. Cao, P. Dotti, S. V. Rajagopal, R. Senaratne, T. Shimasaki, M. Heyl, A. Eckardt, and David Weld and several of the figures have previously appeared on the ArXiv [21]. They are reproduced here with the non-exclusive distribution license: `https://arxiv.org/abs/1809.05554`.

5. The content of appendix B is the result of a collaboration with K. Saha, S. A. Parameswaran, and D. M. Weld, and some of the figures have previously appeared in *Phys. Rev. A* [22]. They are reproduced here with the permission of *Phys. Rev. A*: `https://journals.aps.org/pra/abstract/10.1103/PhysRevA.92.063426`.

Chapter 2

Equilibrium and Non-Equilibrium Statistical Mechanics

To contextualize our experiments on non-equilibrium dynamics, it is useful to first review the basic principles of thermodynamics and statistical mechanics. Statistical mechanics is built on two important concepts: equilibration and thermalization [23]. Equilibration is the approach of a thermodynamically large, closed system to a steady state. Thermalization occurs when the aforementioned steady state depends only on a small number of macroscopic quantities. Thermalization can occur in both integrable and non-integrable closed quantum many-body systems. In order to extend these concepts to periodically driven systems to create a framework to understand our experiments, I will first briefly review the central components of equilibrium statistical mechanics.

2.1 Thermodynamics

In this section, I will state and summarize the fundamental laws of thermodynamics using my notes from my graduate thermodynamics class with Mehran Kardar and quotes from

his excellent textbook [24].

2.1.1 The zeroth law

"*If two systems, A and B are separately in equilibrium with a third system, C, then they are also in equilibrium with one another.*"

The zeroth law establishes temperature. Systems in thermal equilibrium are at the same temperature T.

2.1.2 The first law

"*The amount of work required to change the state of an otherwise adiabatically isolated system depends only on the initial and final states, and not on the means by which the work is performed, or on the intermediate stages through which the system passes.*"

The first law establishes the conservation of energy for macroscopic bodies. For an adiabatic transform, we have:

$$\Delta W = E(\mathbf{X}_{\text{final}}) - E(\mathbf{X}_{\text{initial}}) \tag{2.1}$$

where ΔW is the amount of work needed to change the system from an initial state $\mathbf{X}_{\text{initial}}$ with internal energy $E(\mathbf{X}_{\text{initial}})$ to a final state $\mathbf{X}_{\text{final}}$ with internal energy $E(\mathbf{X}_{\text{final}})$.

For not adiabatic transformations, we have:

$$\delta Q = dE - \delta W \tag{2.2}$$

where δQ is the heat intake of the system and the δ indicates that the heat transfer and

work are not state functions because they depend on the means of applying work and not only on the initial and final states.

2.1.3 The second law

"*No process is possible whose sole result is the complete conversion of heat into work.* "

- William Thomson, 1st Baron Kelvin

"*No process is possible whose sole result is the transfer of heat from a colder to a hotter body.*"

- Rudolf Julius Emanuel Clausius

The second law establishes the direction of heat flow: from hotter to colder bodies. A nice way to understand the second law is to define heat engines and refrigerators. A heat engine takes in heat Q_H from a heat source, produces work W and dumps heat Q_C into a heat sink. A refrigerator uses work W to extract Q_C from a cold source and dumps heat Q_H at a higher temperature. In short, Kelvin's statement of the second law rules out a perfect engine and Clausius's statement of the second law rules out a perfect refrigerator. A useful tool in establishing a temperature scale is the Carnot engine.

Carnot Engine: "A Carnot engine is any engine that is **reversible**, runs in a cycle, with all of its heat exchanges taking place at a source temperature T_H, and a sink temperature T_C. A reversible process is one that can be run backward in time by reversing its inputs and outputs."

In combination with the two statements of the second law, it can be shown that the Carnot engine is the most efficient possible engine operating between two reservoirs

at temperature T_H and T_C. Additionally, this means that all Carnot engines and thus all reversible engines have the same universal efficiency $\eta(T_H, T_C)$. We can establish a temperature scale using the Carnot engine because the universal efficiency of such an engine is only dependent on the temperatures T_H and T_C. In most references and textbooks, a temperature scale is derived by using a Carnot engine constructed from an ideal gas. By this convention, one can derive that the efficiency of a Carnot engine is:

$$\eta \equiv \frac{W}{Q_H} = 1 - \frac{Q_C}{Q_H} = 1 - \frac{T_C}{T_H}. \tag{2.3}$$

We are now in the position to define entropy. Combining equation 2.3 with the two statements of the second law gives us Clausius's theorem:

Clausius's Theorem: "For any cyclic transformation (reversible or not), $\oint \delta Q/T \leq 0$, where δQ is the heat increment supplied to the system at temperature T."

The equality in Clausius's theorem holds for a reversible cycle. This implies that the integral of $\delta Q/T$ between any two points A and B is independent of path. We can then construct the entropy state function S as:

$$S(B) - S(A) = \int_A^B \frac{\delta Q}{T}. \tag{2.4}$$

For reversible (and also quasi-static) processes, we are able to compute the heat from $\delta Q = TdS$ and the work from $\delta W = \sum_i J_i dx_i$ where the J_i are generalized forces and the x_i are corresponding displacements. The first law now implies the following for reversible processes:

$$dE = TdS + \sum_i J_i dx_i. \tag{2.5}$$

An important point is that Equation 2.5 holds generally because it is a relationship

between functions of state. It is the most fundamental thermodynamic relationship.

2.1.4 The third law

"*The entropy of all systems at zero absolute temperature is a universal constant that can be taken to be zero.*"

The third law establishes that:

$$\lim_{T \to 0} S(\mathbf{X}, T) = 0. \tag{2.6}$$

A neat consequence of the third law is that it is impossible to cool any system to absolute zero temperature in a finite number of steps. This doesn't bode well for us as cold atom experimentalists.

2.2 Statistical Mechanics and the Grand Canonical Ensemble

In this section we will review the basic formulas of statistical mechanics using the previous discussion and [25] as our guides.

For a single component system, the most fundamental thermodynamic relationship is equation 2.5 from above:

$$dE = TdS - PdV + \mu dN \tag{2.7}$$

which indicates that the change in internal energy E arises from changes in the entropy

S, the volume V and the number of particles N in a system. The energy of a system is thus a function $E = E(S, V, N)$. We can extract the temperature (T), pressure (P), and chemical potential (μ) with suitable partial derivatives of the energy:

$$T = \left(\frac{\partial E}{\partial S}\right)_{VN} \qquad P = -\left(\frac{\partial E}{\partial V}\right)_{SN} \qquad \mu = \left(\frac{\partial E}{\partial N}\right)_{SV}. \tag{2.8}$$

The internal energy is suitable for studying processes that are adiabatic and reversible. However, it's much better to work with the Helmholtz free energy $F = F(T, V, N)$ or the Gibbs free energy $G = G(T, P, N)$ because experiments are usually performed at a fixed T. We can make a Legendre transformation to these thermodynamic potentials by doing the following:

$$F = E - TS \qquad \rightarrow \qquad dF = -SdT - PdV + \mu dN \tag{2.9}$$

$$G = E - TS + PV \qquad \rightarrow \qquad dG = -SdT + VdP + \mu dN. \tag{2.10}$$

We now have two new expressions for the chemical potential:

$$\mu = \left(\frac{\partial F}{\partial N}\right)_{TV} = \left(\frac{\partial G}{\partial N}\right)_{TP}. \tag{2.11}$$

If we want to work with a system with variable N, then it is best to work with the thermodynamic potential $\Omega = \Omega(T, V, \mu)$:

$$\Omega = F - \mu N = E - TS - \mu N \qquad \rightarrow \qquad d\Omega = -SdT - PdV - Nd\mu \tag{2.12}$$

where S, P, and N can be obtained via suitable derivatives of the thermodynamic potential.

The set of variables (S, V, N) are extensive variables which are proportional to the

amount of matter in a system. We can now consider a scale change in which all extensive variables (which includes E, F, G and Ω) are multiplied by a factor λ. If we then differentiate with respect to λ and set λ equal to 1, we find:

$$E = TS - PV - \mu N \tag{2.13}$$

$$F = -PV + \mu N \tag{2.14}$$

$$G = \mu N \tag{2.15}$$

$$\Omega = -PV \tag{2.16}$$

We can relate the thermodynamic functions to the Hamiltonian of a many-body system using the grand canonical ensemble. The grand canonical ensemble is:

$$Z_G = \sum_N \sum_k e^{-\beta(E_k - \mu N)} = \sum_N \sum_k \langle Nk| \, e^{-\beta(\hat{H} - \mu \hat{N})} \, |Nk\rangle = \mathrm{Tr}(e^{-\beta(\hat{H} - \mu \hat{N})}). \tag{2.17}$$

It can be readily shown that:

$$\Omega(T, V, \mu) = -k_B T \ln(Z_G). \tag{2.18}$$

Moreover, for any operator $\hat{O}$, the ensemble average $\langle \hat{O} \rangle$ can be calculated using:

$$\boxed{\langle \hat{O} \rangle = \mathrm{Tr}(\hat{\rho}_G \hat{O}), \qquad \hat{\rho}_G \equiv Z_G^{-1} e^{-\beta(\hat{H} - \mu \hat{N})}}. \tag{2.19}$$

A system whose observables are describable by the above ensemble is said to be thermal or have thermalized.

2.3 Generalized Gibbs Ensembles and Prethermalization

The relaxation of an isolated quantum many-body system to thermal equilibrium is a fundamental question in physics [26, 27]. If a system is integrable, then it is generally expected to relax to a steady state described by a generalized Gibbs ensemble (GGE), which I'll define in a moment, where the conservation laws constrain the dynamics of the system [28, 29, 30]. If the system is not-integrable, then the quantum system is generally expected to undergo thermalization [27]. If only the total energy is conserved in this final thermalized state, then the local observables will relax to the grand canonical or Gibbs ensemble with an effective temperature, as discussed in the previous section. However, the fact that non-integrable systems are not integrable does not preclude the realization of steady states described by a generalized Gibbs ensemble prior to eventual thermalization. The realization of a steady state describable by a generalized Gibbs ensemble as a prelude to eventual thermalization (or another steady state) is called prethermalization. In the limit of vanishing inter-particle interactions between the components of a quantum system, the steady state attained with the generalized Gibbs ensemble is the final steady state.

As a concrete example, consider an integrable Hamiltonian $\hat{H}$ with observables $\hat{O}$ and initial state $|\psi(0)\rangle$. The initial state evolves in time as $|\psi(t)\rangle = \exp(-i\hat{H}t/\hbar)\,|\psi(0)\rangle$. The expectation values of the observables are given in the long-time limit by the generalized Gibbs ensemble [27, 31]:

$$\lim_{t\to\infty} \langle\psi(t)|\,\hat{O}\,|\psi(t)\rangle = \mathrm{Tr}[\hat{\rho}_{GGE}\hat{O}] \tag{2.20}$$

where

$$\hat{\rho}_{GGE} = \frac{1}{Z} \exp\left(- \sum_j \lambda_j \hat{I}_j \right). \tag{2.21}$$

In the above equation, $Z = \mathrm{Tr} \exp(-\sum_j \lambda_j \hat{I}_j)$ is the partition function and $\hat{I}_j$ are the conserved quantities. The Lagrange multipliers λ_m are fixed to maximize the entropy

$$S = -\mathrm{Tr}[\hat{\rho}_{GGE} \ln \rho_{GGE}] \tag{2.22}$$

under the constraint that the expectation values of the conserved quantities in the ensemble are equal to the initial values:

$$\mathrm{Tr}[\hat{I}_j \hat{\rho}_{GGE}] = \langle \hat{I}_J \rangle (t = 0). \tag{2.23}$$

As an important aside, in the case that only the energy and particle number are conserved, the generalized Gibbs ensemble becomes the typical grand canonical ensemble discussed in the previous section. In this case, the inverse temperature β plays the role of the Lagrange multiplier for energy and the chemical potential μ plays the role of the Lagrange multiplier for the particle number.

From theoretical and experimental studies [32, 28, 33, 34, 35], it is expected that nearly-integrable systems first relax to a metastable prethermal plateau describable by a generalized Gibbs ensemble. The amount of time spent in this prethermal plateau increases the closer the system is to integrability. In our experiments, we have the ability to tune the length of time spent in prethermal states with control of the s-wave scattering length with the Feshbach resonance in lithium. Figure 2.1 summarizes the various ways a quantum many-body system may approach a steady state or thermal state. It can be the case and is also mentioned in [27] that many-body localization (MBL) can also prevent a system from attaining ergodicity and reaching thermal equilibrium. As a response, it has

been suggested that a generalized Gibbs ensemble can be used to describe a many-body localized state by taking into account an external potential [36, 37]. Additionally, MBL only applies in the case of bounded energy, for example in single-band systems or in spin systems [38].

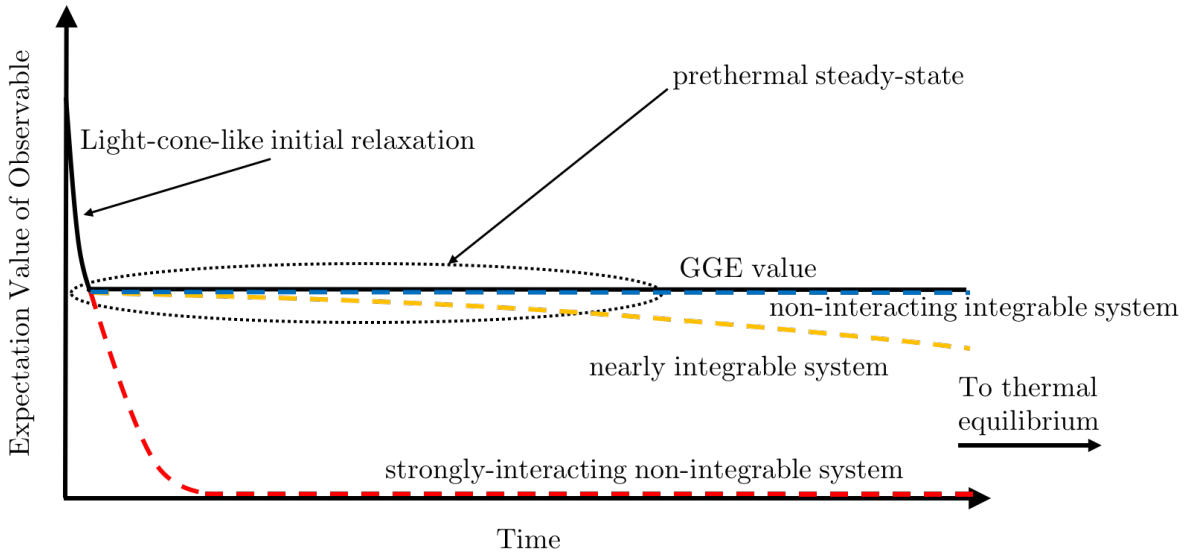

Figure 2.1: How a generic quantum many-body system can generally relax to a steady state or final thermal state. A typical observable for a non-interacting integrable system (blue) will relax to a value according to the conserved quantities that define the generalized Gibbs ensemble. A nearly-integral system (yellow) will first relax to a meta-stable prethermal plateau described by a generalized Gibbs ensemble before reaching thermal equilibrium. A strongly interacting non-integrable system (red) is typically expected to rapidly relax to thermal equilibrium.

2.4 Periodic Gibbs Ensemble

Building upon the previous framework, we now move into periodically driven systems. It is generally believed that any generic driven system that lacks temporal periodicity will heat to infinite temperature at infinite time [39]. This is due to the fact that energy is not conserved in a system that lacks continuous time-translation symmetry. However,

is has been established that periodically driven systems (where energy is conserved only modulo $2\pi/T$ with T being the drive period), can avoid heating for long-time scales and can relax to long-time steady states that are describable by a generalized statistical mechanical framework [39, 23, 40, 41, 42]. Importantly, these long-time steady states exhibit tunable properties that depend upon the characteristics of the drive. The goal of Floquet engineering is to create novel steady states with tailored properties that would be otherwise unattainable in the conventional static system.

An intuitive picture for the relaxation of an isolated time periodically driven quantum system can be given as follows [23, 40]. Consider a time-periodic Hamiltonian with period T:

$$\hat{H} = \hat{H}(t+T). \tag{2.24}$$

The time dependent Schrödinger equation of this driven system possesses quasi-stationary solutions, called Floquet states, which are of the form:

$$|n(t)\rangle e^{it\varepsilon_n/\hbar}, \tag{2.25}$$

with real quasienergy ε_n and time-periodic Floquet mode

$$|n(t)\rangle = |n(t+T)\rangle. \tag{2.26}$$

For each time t, the Floquet states form an orthogonal basis, so that for a given pure initial state $|\psi(0)\rangle$ the expectation value of an observable $\hat{O}$ evolves like

$$\langle\hat{O}\rangle(t) = \sum_{nn'} c_n^* c_{n'} \langle n(t)|\hat{O}|n'(t)\rangle e^{it(\varepsilon_n - \varepsilon'_n)/\hbar}, \tag{2.27}$$

with time-independent coefficients $c_n = \langle n(0)|\psi(0)\rangle$. The relaxation to a quasi steady

state (i.e. a time periodic state) in the long-time limit can be associated with the dephasing and averaging out of the off-diagonal terms, so that asymptotically

$$\langle \hat{O} \rangle(t) \simeq \sum_n |c_n|^2 \langle n(t)|\hat{O}|n(t)\rangle, \tag{2.28}$$

which corresponds to a Floquet diagonal ensemble described by a periodic density operator, namely

$$\hat{\rho}_{\text{dia}}(t) = \sum_n |c_n|^2 |n(t)\rangle\langle n(t)|. \tag{2.29}$$

The above two equations are the analogy to the equations in 2.19 for a periodically driven system. While in a many-body system, the diagonal ensemble is still characterized by an exponentially large number of probabilities $|c_n|^2$, it is believed that the quasi steady state is characterized by a generalized Gibbs ensemble, called periodic Gibbs ensemble (PGE),

$$\hat{\rho}_{PGE} = Z^{-1} \exp(-\sum_j \lambda_j \hat{I}_j(t)), \tag{2.30}$$

with $\hat{I}_j(t) = \hat{I}_j(t+T)$ denoting the integrals of motion of the system. For a non-interacting driven gas, we have an extensive number of integrals of motion given by the number operators $\hat{n}_j(t)$ of the single-particle Floquet modes $|j(t)\rangle = |j(t+T)\rangle$. The expectation values of these number operators determine the PGE so that the system is non-ergodic (i.e. localized). A generic interacting Floquet system should at sufficiently long times approach a fully ergodic infinite-temperature-like state $\rho_{\text{ergodic}} \propto 1$*. However, if the effect of interactions is weak, it is possible that the system responds to the interactions only on a very long time scale. In this scenario, the system can approach a prethermal

*An experimental example of a non-generic non-ergodic periodically driven many-body localized (MBL) system is discussed in [43].

steady state on intermediate time scales that is accurately described by the PGE. The attainment of this prethermal steady state and subsequent decay would constitute an observation of Floquet prethermalization [44]. An experimental observation of a PGE associated with Floquet prethermalization using lithium atoms in a strongly amplitude modulated optical lattice is the subject of Chapter 6.

2.5 Bose-Einstein Condensation

Before we jump into the laser cooling sequence and the experimental apparatus, let's first quickly discuss the phenomena of Bose-Einstein condensation since it is the most important tool in the experiments conducted in this thesis.

Bose-Einstein condensation can be understood rather straightforwardly. Let's consider the following scenario[†]:

(a) Bosons are non-interacting

(b) Bosons are put in a box of volume V

(c) Energy spectrum is given by $\epsilon_p = \frac{p^2}{2m} = \frac{\hbar^2 k^2}{2m}$

(d) Periodic boundary conditions are imposed on the single particle wavefunctions

We will find that a Bose-Einstein condensate arises in this scenario due purely to quantum statistics. Recall that the average occupation number for bosons is given by:

$$\langle n_k \rangle = \frac{1}{e^{\beta(\epsilon_k - \mu)} - 1} \tag{2.31}$$

For ease of calculation, we will replace the sums over single-particle levels with an

[†]The calculations that follow are adapted from the wonderful textbook by Fetter and Walecka [25].

integral over wavenumbers:

$$\sum_i \to g \int d^3n \to gV(2\pi)^{-3} \int d^3k \tag{2.32}$$

where g is the degeneracy of each single-particle momentum state. In three dimensions, the density of states can be written in terms of energy as:

$$gV(2\pi)^{-3} 4\pi k^2 dk = \frac{gV}{4\pi^2} \left(\frac{2m}{\hbar^2}\right)^{3/2} \epsilon^{1/2} d\epsilon. \tag{2.33}$$

Recall that for a gas of bosons, the thermodynamic potential is written as [25]:

$$\Omega(T, V, \mu) = k_B T \sum_{k=0}^{\infty} \ln(1 - e^{\beta(\mu - \epsilon_k)}). \tag{2.34}$$

Using equation 2.32 to replace the sum, we find:

$$-\frac{\Omega(T, V, \mu)}{k_B T} = \frac{PV}{k_B T} = -\frac{gV}{4\pi^2} \left(\frac{2m}{\hbar^2}\right)^{3/2} \int_0^{\infty} d\epsilon \ \ln(1 - e^{\beta(\mu - \epsilon)}) \epsilon^{1/2}. \tag{2.35}$$

A simple partial integration then gives:

$$PV = \frac{gV}{4\pi^2} \left(\frac{2m}{\hbar^2}\right)^{3/2} \frac{2}{3} \int_0^{\infty} d\epsilon \ \frac{\epsilon^{3/2}}{e^{\beta(\epsilon - \mu)} - 1}. \tag{2.36}$$

Using the thermodynamic potential and suitable derivatives, one can also write:

$$E = \frac{gV}{4\pi^2} \left(\frac{2m}{\hbar^2}\right)^{3/2} \int_0^{\infty} d\epsilon \ \frac{\epsilon^{3/2}}{e^{\beta(\epsilon - \mu)} - 1} \tag{2.37}$$

which tells us that the equation of state for an ideal Bose gas is:

$$PV = \frac{2}{3} E. \tag{2.38}$$

The average particle number is obtained via:

$$\langle N \rangle = \sum_{k=0}^{\infty} \langle n_k \rangle = \frac{gV}{4\pi^2} \left(\frac{2m}{\hbar^2} \right)^{3/2} \int_0^{\infty} d\epsilon \frac{\epsilon^{1/2}}{e^{\beta(\epsilon-\mu)} - 1}. \tag{2.39}$$

As the temperature of the system is brought closer to zero, more and more atoms begin to occupy the ground state. The mean occupation number in the ground state (ϵ_0) must approach N as $T \to 0$:

$$\lim_{T \to 0} \langle n_0 \rangle = \lim_{T \to 0} \frac{1}{e^{\beta(\epsilon_0 - \mu)} - 1} = N \tag{2.40}$$

Looking at equation 2.40, it must be the case that the exponential is greater than 1, which requires the chemical potential to be less than the ground state energy. However, in order to produce the macroscopically large number N, it must be the case that the exponential is very close to 1. This means the exponent must be small, allowing us to Taylor expand as follows:

$$\frac{1}{1 + (\epsilon_0 - \mu)/k_B T + ... - 1} \approx N. \tag{2.41}$$

Solving for μ gives us the relation:

$$\mu \approx \epsilon_0 - \frac{k_B T}{N}. \tag{2.42}$$

We see that the chemical potential approaches the ground state energy from below as we lower the temperature. The ground state energy is usually insignificant and we define the temperature at which μ becomes zero as the Bose-Einstein temperature or the characteristic temperature. Using the substitution $x \equiv \epsilon / k_B T_0$ where T_0 is the temperature

where μ vanishes, we have:

$$\frac{N}{V} = \frac{g}{4\pi^2}\left(\frac{2mk_BT_0}{\hbar^2}\right)^{3/2}\int_0^\infty d\epsilon \frac{x^{1/2}}{e^x - 1} = \frac{g}{4\pi^2}\left(\frac{2mk_BT_0}{\hbar^2}\right)^{3/2}\Gamma\left(\frac{3}{2}\right)\zeta\left(\frac{3}{2}\right). \quad (2.43)$$

Inverting this gives the characteristic temperature as:

$$\boxed{T_0 = \left(\frac{\hbar^2}{2mk_B}\right)\left(\frac{4\pi^2}{g\Gamma\left(\frac{3}{2}\right)\zeta\left(\frac{3}{2}\right)}\right)^{2/3}\left(\frac{N}{V}\right)^{2/3}} \quad (2.44)$$

Equation 2.44 demonstrates that the characteristic temperature can be thought of as the the temperature in which the thermal energy k_BT_0 becomes comparable with the only other intensive energy for a perfect gas, namely the zero-point energy $\frac{\hbar^2}{2m}(\frac{N}{V})^{2/3}$ associated with localizing a particle of mass m in a volume V/N. And that temperature is given here. The important thing to note here is that the critical temperature is inversely proportional to the mass and proportional to the density to the 2/3.

For temperature $T < T_0$, we may reasonably conclude that the chemical potential must be infinitesimally small, which allows us to compute the excited state population as follows:

$$\frac{N_{\epsilon>0}}{V} = \frac{g}{4\pi^2}\left(\frac{2mk_BT}{\hbar^2}\right)^{3/2}\int_0^\infty d\epsilon \frac{x^{1/2}}{e^x - 1} = \frac{N}{V}\left(\frac{T}{T_0}\right)^{3/2}. \quad (2.45)$$

This tells us the population of atoms in the ground state is given by:

$$\boxed{N_0 = N\left(1 - \left(\frac{T}{T_0}\right)^{3/2}\right)}. \quad (2.46)$$

The above equation tells us that the population in the ground state is of order N until $T > T_0$. It can also be readily shown that the energy of the Bose gas for $T \leq T_0$ is given

by:

$$E = \frac{\Gamma\left(\frac{5}{2}\right)\zeta\left(\frac{5}{2}\right)}{\Gamma\left(\frac{3}{2}\right)\zeta\left(\frac{3}{2}\right)} N k_B T \left(\frac{T}{T_0}\right)^{3/2} \tag{2.47}$$

with a corresponding heat capacity[†] of:

$$C_V = \frac{5}{2}\frac{\Gamma\left(\frac{5}{2}\right)\zeta\left(\frac{5}{2}\right)}{\Gamma\left(\frac{3}{2}\right)\zeta\left(\frac{3}{2}\right)} N k_B \left(\frac{T}{T_0}\right)^{3/2}. \tag{2.49}$$

In general, the exponent and the coefficient in front of the density in equation 2.44 and the exponent in equation 2.46 are modified by the trapping potential of the BEC as discussed in Chapter 2 of [6]. In our experiment, we trap our lithium condensate inside a three-dimensional harmonic trap called the crossed optical dipole trap. For a non-interacting Bose gas trapped harmonically in three dimensions, the characteristic temperature is

$$\boxed{k_B T_0 = \frac{\hbar\bar{\omega}}{[\zeta(3)]^{1/3}}\left(\frac{N}{V}\right)^{1/3}} \tag{2.50}$$

where $\bar{\omega}$ is the geometric mean of the three harmonic oscillator frequencies in each direction: $\bar{\omega} = (\omega_x\omega_y\omega_z)^{1/3}$. The number of particles in the condensate in the three-dimensional harmonic oscillator potential is given by:

$$\boxed{N_0 = N\left(1 - \left(\frac{T}{T_0}\right)^3\right)}. \tag{2.51}$$

[†]The pressure (for $T < T_0$) can also be readily obtained using:

$$P = \frac{2}{3}\frac{E}{V} = \frac{2}{3}\frac{2\sqrt{2}}{4\pi^2}\Gamma\left(\frac{5}{2}\right)\zeta\left(\frac{5}{2}\right)\frac{g m^{3/2}(k_B T)^{5/2}}{\hbar^3}, \tag{2.48}$$

which demonstrates that the pressure vanishes at zero temperature because all particles are in the zero-momentum state. Moreover, the pressure is independent of the density which I personally find incredibly cool.

The important take-away message is that for a dilute gas of bosons, **this temperature is typically in the nano-kelvin to micro-kelvin range, which means that laser cooling and trapping is essential to the production of Bose-Einstein condensates.** Onwards to laser cooling techniques!

Chapter 3

Laser Cooling Techniques

The wavenumber k of each lithium atom is an external quantum number that describes the momentum of each atom ($p = \hbar k$). In order to create low-entropy ground states, we need experimental control over both the external quantum numbers and the internal quantum numbers of the lithium atoms. These quantum numbers are controlled using a variety of laser cooling techniques. To understand the laser cooling steps we take to produce a lithium BEC, we have to first talk about the internal quantum numbers that identify the energy levels of lithium. Lithium has three electrons: two in a closed $1s^2$ shell and a single valence electron. In Figure 3.1, I have made what is known as a Russel-Saunders plot for ^{7}Li which indicates the quantum energy levels of that single valence electron. Atomic physicists use diagrams like these to figure out what frequencies and light polarizations they need to drive transitions within an atom. The terms on the left side of Figure 3.1 are known as spectroscopic term symbols. They are generally given by:

$$^{2S+1}L_J. \tag{3.1}$$

Landé g-factors		
State	F	g_F
$^2P_{3/2}$	3	2/3
	2	2/3
	1	2/3
	0	0
$^2P_{1/2}$	2	1/6
	1	1/6
$^2S_{1/2}$	2	1/2
	1	-1/2

Table 3.1: List of Landé g-factors for low magnetic field

The $(2S+1)$ number on the top left describes the total electronic spin, where S is the total electronic spin. The letter L indicates the total orbital angular momentum and is labeled with the letters $S, P, D, F, G...$ for total orbital angular momentum $0, 1, 2, 3, 4...$, respectively. The subscript J indicates the sum of the total spin and total orbital angular momentum. On the right side of Figure 3.1 is the quantum number F, which is the sum of the electronic spin, electronic orbital momentum, and the nuclear spin. We refer to the $F = 2$ and $F = 1$ states in the $^2S_{1/2}$ manifold as the ground states of lithium. The transition from $^2S_{1/2}$ to $^2P_{1/2}$ is called the D1 line and the transition from $^2S_{1/2}$ to $^2P_{3/2}$ is called the D2 line. A nice fact about lithium is that the energy difference between the D1 and D2 lines is only 10 GHz, which means it can easily be spanned with an electro-optic modulator (EOM) or with several acousto-optic modulators (AOMs). Additionally, the hyperfine splitting in the various orbital states are also in the tens or hundreds of MHz which can easily be addressed with AOMs. The D1 and D2 lines of lithium both have lifetimes of 27 ns corresponding to linewidths of 5.9 MHz. For small magnetic fields, the magnetic sublevels of the hyperfine states will vary in energy according to their Landé g-factors. A table of the Landé g-factors for low magnetic fields is included in Table 3.1.

In order to cool the lithium atoms, we must manipulate the population of the energy levels using a variety of laser cooling techniques. An overview of our full sequence of laser

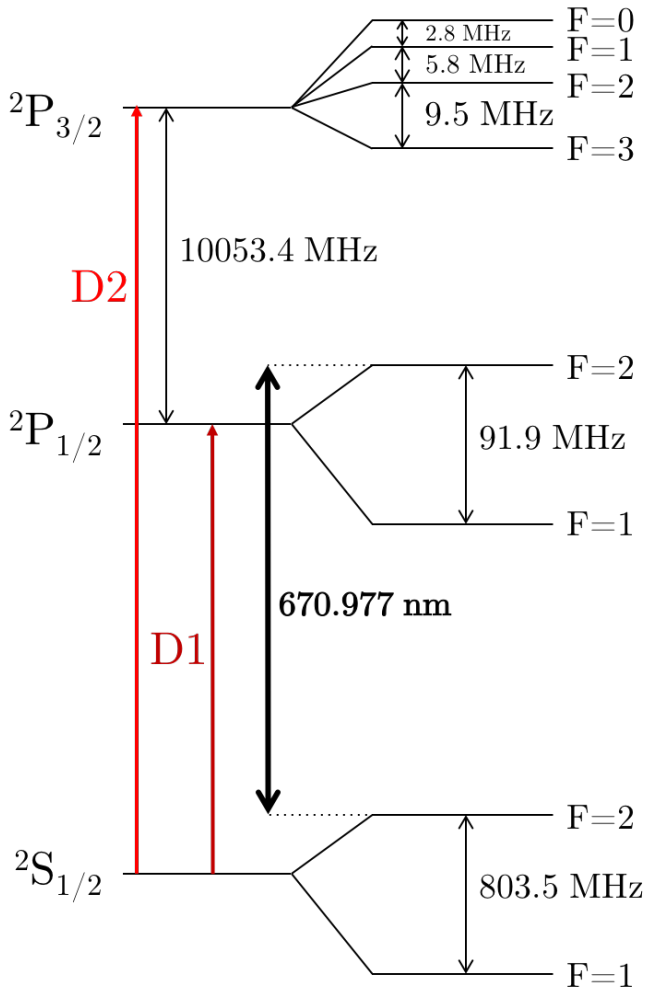

Figure 3.1: ^{7}Li level diagram using data from [45].

cooling to a BEC is shown in Figure 3.2. The majority of the cooling after gray molasses (GM) is done evaporatively. The scattering length between lithium atoms plays an essential role in this process. A large absolute value of the scattering length is necessary for atoms to scatter and reach equilibrium. To produce a large stable BEC, a large positive scattering length is necessary. A BEC can be formed with a negative scattering length, but it will be unstable and small [17]. Unfortunately, the bare zero-temperature scattering length in the magnetically trappable $|F = 2, m_F = 2\rangle$ ground state is -27 a_0 and the

bare zero-temperature scattering length in the magnetically trappable $|F = 1, m_F = -1\rangle$ ground state is $+5\ a_0$. The scattering length in the $|1, -1\rangle$ state is much too small to allow efficient evaporation and the formation of large BECs. The scattering length in the $|1, 1\rangle$ state can be tuned with a Feshbach resonance, but because this state is not magnetically trappable this requires loading atoms in a crossed optical dipole trap first before applying a large spatially homogeneous magnetic field to access the Feshbach resonance.

Our solution to all of the above problems is to take the following approach: we must efficiently cool as many atoms as possible into a crossed optical dipole trap and then use the Feshbach resonance in the $|1, 1\rangle$ state to increase the scattering length and optically evaporate to obtain a large BEC. To get a large number of cold, dense atoms into the crossed optical dipole trap, we must first radio-frequency evaporate in a magnetic trap. We choose to work with the $|2, 2\rangle$ state in the magnetic trap to have the highest bare scattering length and to avoid spin-changing collisions between atoms. Care must be taken with this state because the scattering length has a zero-point at a collisional energy of roughly 6 mK (see the discussion in Chapter 1 of [46]), which means evaporation must begin at a temperature much lower than that. Therefore, we have to have the atoms be colder than 6 mK at the onset of radio-frequency evaporation to avoid the thermal zero-crossing of the scattering length. Hence, it is necessary to apply a gray molasses to cool the atoms below the Doppler limit prior to loading of the magnetic trap. All of this will be discussed in detail in the following sections.

3.1 Scattering Force

The lithium atoms begin their life in our experiment as a solid. They are heated to 450 degrees Celsius and pass through a nozzle to form a collimated atomic beam, as indicated in Figure 3.3. Upon exiting the oven, the atoms are moving at about $v_0 = 1$ km/s.

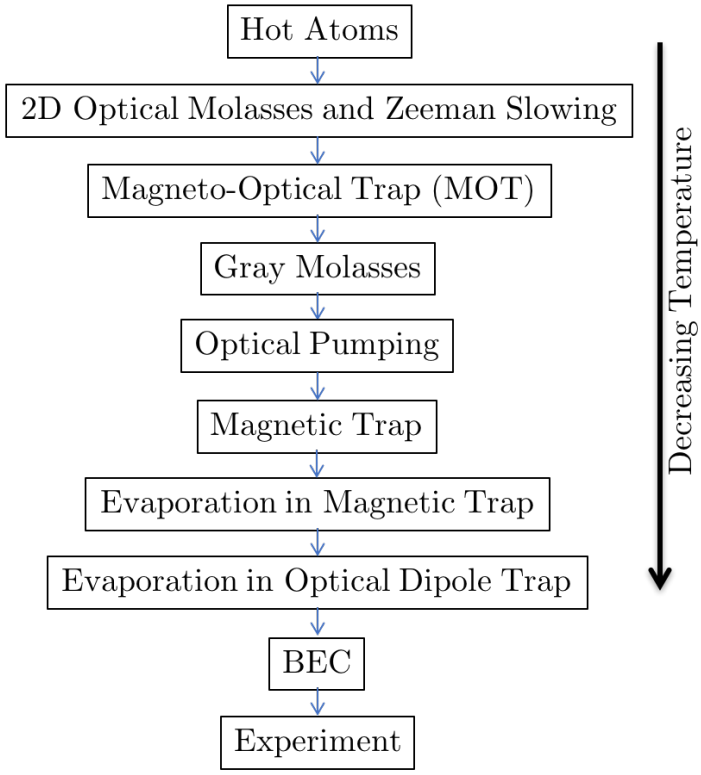

Figure 3.2: General overview of the cooling sequence.

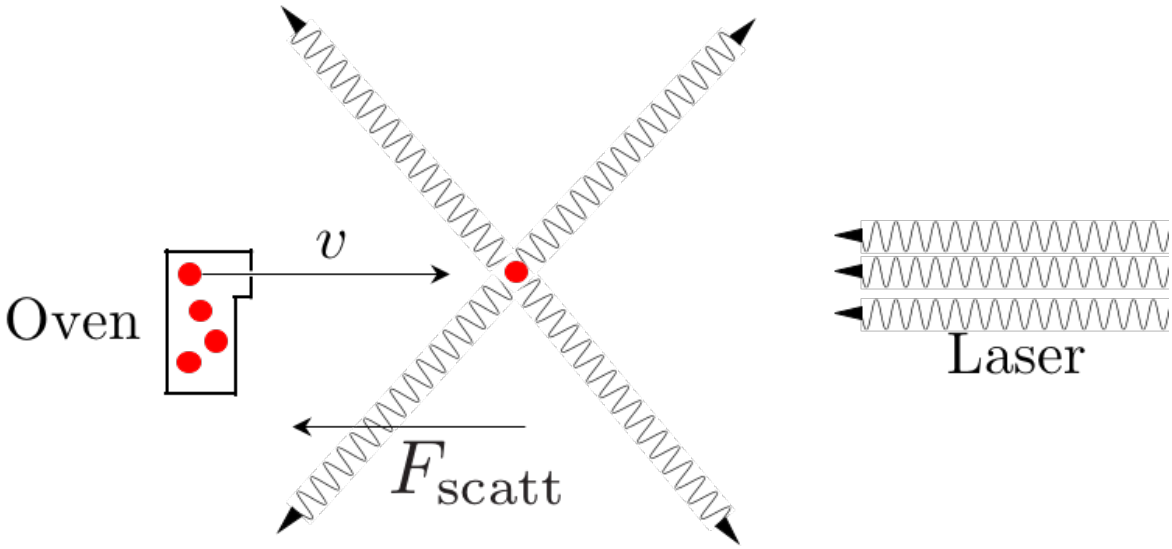

Figure 3.3: Diagram of scattering force.

To initially slow down the atoms, we apply counter-propagating laser light tuned to the D2 transition of the lithium atoms, going from the ${}^2S_{1/2}$ $F = 2$ to ${}^2P_{3/2}$ $F' = 3$ states. We call this the cooler or cycling light. If we have a beam of atoms traveling with velocity v into that laser beam, then the atom can absorb a photon and receive a momentum kick in the direction opposing the atom's velocity. Roughly 27 ns later, the lithium atom will then de-excite and release a photon in a random direction spontaneously. On average, the atoms' velocity in the direction of the laser beam is reduced.

The force that results from this scattering of photons is given by:

$$F_{scatt} = \hbar k \frac{\Gamma}{2} \frac{I/I_{sat}}{1 + I/I_{sat} + 4\delta^2/\Gamma^2}, \tag{3.2}$$

where $\hbar k$ is the momentum of a 671 nm photon, Γ is the linewidth, I is the intensity of the laser radiation, δ is the detuning of the laser frequency from the energy difference of the atomic levels and I_{sat} is the saturation intensity equal to 2.56 mW/cm^2.

Unfortunately, the ${}^2S_{1/2}$ $F = 2$ to ${}^2P_{3/2}$ $F' = 3$ transition is not a perfectly closed transition. Because the linewidth of the transition is 6 MHz and the hyperfine splitting to the $F' = 2$ state is 9.5 MHz, there is a large probability for the atoms to be pumped to ${}^2P_{3/2}$ $F' = 2$. In this case, the atoms can spontaneously decay down to the ${}^2S_{1/2}$ $F = 1$ state. To fix this, we need to apply repumping laser light on the ${}^2S_{1/2}$ $F = 1$ to ${}^2P_{3/2}$ $F' = 2$ transition. Experimentally, it is good to have the repumping laser light power be at least 20-25% of the cycling laser light power.

3.2 Zeeman Slowing

However, this isn't the complete picture. At higher velocities, the atom will see the laser beam at a higher frequency due to the Doppler shift. This is a major problem

because the Doppler shift for thermal atoms can be much greater than the linewidth of the transition and cause the light-scattering to turn off as the velocity is reduced. We have to exactly compensate for the Doppler shift using the Zeeman shift produced from a spatially varying magnetic field. This magnetic field is generated from a tapered solenoid. Figuring out the necessary magnetic field is rather straightforward. One sets the Zeeman shift of the transition energy equal to the Doppler shift of the laser light:

$$\omega_0 + \frac{\mu' B(z)}{\hbar} = \omega + kv. \tag{3.3}$$

where $\mu' = (m_{F'} g_{F'} - m_F g_F)\mu_B$ (here, g_F are the Landé g-factors), ω_0 is the frequency of the atomic transition and ω is the frequency of the laser. If one tries to keep the scattering force at its maximum value during the entirety of the Zeeman slowing process, then one typically needs a magnetic field profile that varies spatially as:

$$B(z) = B_0 \left(1 - \frac{z}{L_0}\right)^{1/2} + B_{bias} \tag{3.4}$$

where $B_0 = \hbar k v_0/\mu'$, $B_{bias} = \hbar(\omega - \omega_0)/\mu'$ and $L_0 = m v_0^2/F_{max}$. The lithium machine has a Zeeman slower that is about a meter long.

Our Zeeman slowing laser beam is 42 mW (20% repump) and is detuned by about 400 MHz.

3.3 Optical Molasses

Once the atoms exit the nozzle, they begin to spread out transversely. This is called beam explosion. To prevent this we use a combination of the Doppler effect and the laser detuning to damp the motion. Damping performed in this way is called optical molasses.

To understand optical molasses, imagine you have six laser beams pointed orthog-

onally around an atom at rest. Let all six laser beams be red-detuned of an atomic transition, which means that their energy is less than that of the atomic transition. If the atom moves in the direction of any laser beam, it will Doppler shift the laser beam to a higher frequency and become closer to resonance with the frequency of the laser beam. This results in a molasses force opposing the atomic motion in all directions.

This molasses force is generally given by:

$$F_{molasses} = -\alpha v \tag{3.5}$$

where

$$\alpha = 4\hbar k^2 \frac{I}{I_{sat}} \frac{-2\delta/\Gamma}{[1 + (2\delta/\Gamma)^2]^2}. \tag{3.6}$$

Molasses can be used to cool the atoms in all six directions. However, there is a limit to the temperature produced by this technique. After each spontaneous emission event, the atomic velocity changes by the recoil velocity in a random direction. This means the atom performs a random walk in velocity space and heats diffusively. The lowest temperature expected by optical molasses is called the Doppler cooling limit and is determined by balancing the rate of the diffusive heating to the rate of cooling. The Doppler cooling limit is given by:

$$k_B T_D = \frac{\hbar\Gamma}{2} \tag{3.7}$$

where k_B is Boltzmann's constant. The Doppler cooling limit for lithium is 140 μK. After the oven, the atoms are cooled in a direction transverse to the atomic beam flux using 2D optical molasses. This 2D optical molasses is performed once before the Zeeman slower and once after the Zeeman slower.

Unfortunately, one can not trap the atoms using a six beam molasses because the energy shift only depends on velocity and not on the spatial positions of the atoms.

3.4 Magneto-optical trap

Enter the magneto-optical trap (MOT). This is the quintessential neutral atom trapping technique. In a magneto-optical trap, one uses the combination of a magnetic quadrupole field and properly polarized optical molasses beams to produce a position dependent energy shift that traps the atoms. By using red-detuned laser beams on a transition whose energy level splitting decreases with magnetic field, atoms preferentially absorb photons from the laser beam that pushes them back towards the field zero of the magnetic trap. A great description of the MOT is given in [47]. The force produced by this combination of polarized optical molasses and magnetic fields results in a force given by:

$$F_{MOT} = -\alpha v - \frac{\alpha}{k}\frac{g\mu_B}{\hbar}\frac{dB}{dz}z \tag{3.8}$$

A diagram of our MOT is shown in Figure 3.4. To produce the magnetic quadrupole field, we use a pair of anti-Helmholtz coils that produce a field gradient of 20 G/cm. The magnetic fields point inward toward the center of the chamber along the horizontal plane and point outwards through the top and bottom windows. The laser beams are all circularly polarized to drive σ^- transitions on the $^2S_{1/2}$ $F = 2$ to $^2P_{3/2}$ $F' = 3$ transition. Recall that a weak magnetic field perturbs the atomic transition according to:

$$E = \mu' B = (m_{F'} g_{F'} - m_F g_F)\mu_B B. \tag{3.9}$$

A list of the various transitions on the MOT cycler and their μ' factors are included in Table 3.2.

With respect to the directions of the magnetic field lines, this means all the MOT beams are left-circularly polarized in the horizontal plane and that the top and bottom

σ^+ transitions			σ^- transitions		
m_F	$m_{F'}$	μ'	m_F	$m_{F'}$	μ'
2	3	1	-2	-3	-1
1	2	5/6	-1	-2	-5/6
0	1	2/3	0	-1	-2/3
-1	0	1/2	1	0	-1/2
-2	-1	1/3	2	1	-1/3

Table 3.2: List of μ' factors for $^2S_{1/2}$ $F = 2$ to $^2P_{3/2}$ $F' = 3$ transitions. Our MOT uses red-detuned light to address the σ^- transitions because the energy levels of these transitions decrease with increasing magnetic field.

beams are right-circularly polarized. The MOT beams are composed of both cycling and repumping light and are red-detuned from their respective atomic resonances by about 5 Γ. Generally speaking, we typically have 6.5 to 7.5 mW of cycling power and 2 to 3 mW of repumping power in each horizontal MOT beam. We generally have 12 to 14 mW of cycling power and 5 to 6 mW of repumping power in each vertical MOT beam.

A picture of our MOT is shown in Figure 3.5. Our MOT can typically load about 4 billion atoms in 10 to 15 seconds, with a maximum MOT size of about 6 billion atoms in 30 seconds or so. To keep atom number the same from experimental run to experimental run, we trigger our laser cooling sequence on the voltage from a photodiode looking at fluorescence from the MOT.

Our MOT typically has a density of 10^{10} cm^{-3} and a temperature of a few mK. This means that we have to increase the density by three orders of magnitude and decrease the temperature by three orders of magnitude to obtain a BEC. To increase the density prior to gray molasses, we ramp the field gradients to 80 G/cm while at the same time bringing the cycling light close to resonance and significantly attenuating the repumping light. This pushes atoms in from the outside and increases the density to 10^{11} cm^{-3}. As the atoms move inwards, we apply gray molasses to cool the atoms to 60 μK, as will be discussed in the next section.

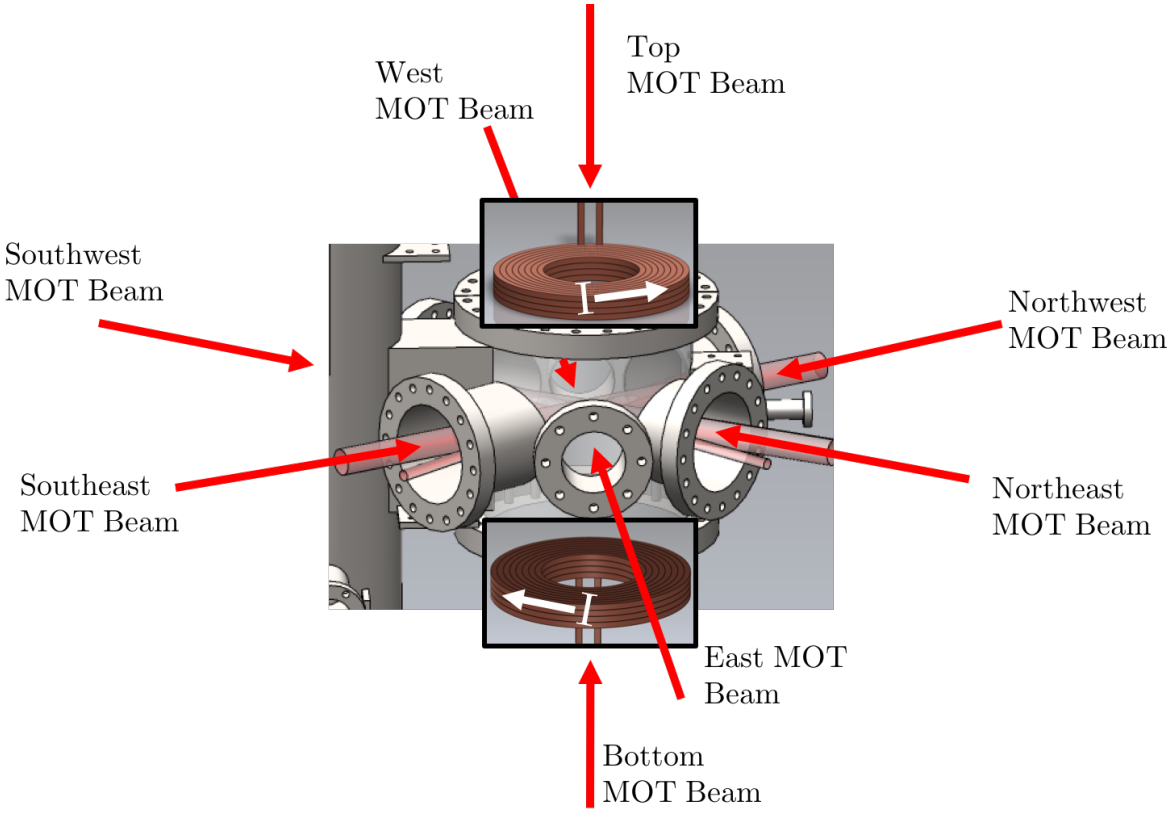

Figure 3.4: Diagram of the MOT. In our experiment, we actually use eight MOT beams instead of six. This is because our original MOT windows are at too shallow of an angle to strongly confine the atoms in the direction transverse to the slower beam in the horizontal plane.

We could load the MOT directly into the magnetic trap without gray molasses. However, we would not be able to successfully evaporate. This is because the temperature of the MOT is about 1 mK and loading directly into the magnetic trap would squeeze the atoms and increase the temperature even further such that the scattering length in the magnetically-trapped $|2, 2\rangle$ state would approach zero.

3.5 Gray Molasses

As mentioned before, the temperature limit associated with optical molasses is the Doppler cooling limit. This temperature is 140 μK for lithium. To cool below the

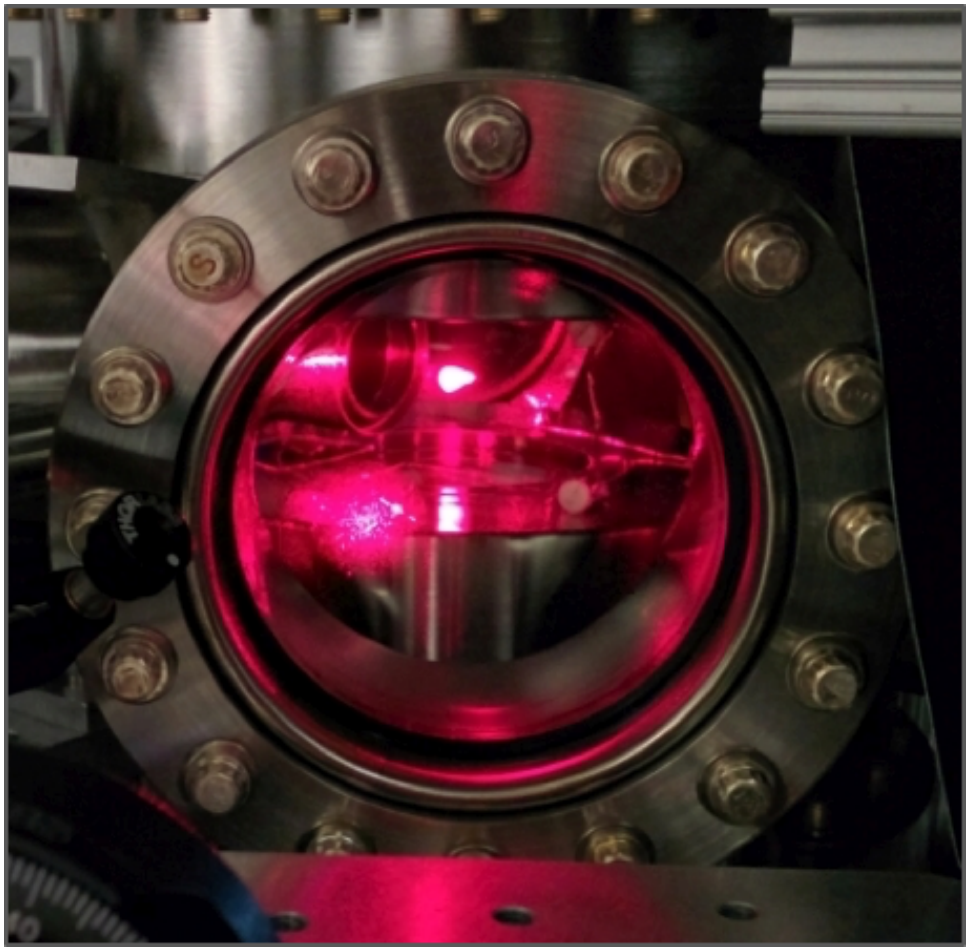

Figure 3.5: The red floating fluorescing orb in the center is the MOT. This particular MOT is composed of about 4 billion atoms.

Doppler limit we have to play a few games. Cooling below the Doppler limit is called sub-Doppler cooling (surprise surprise).

In early MOT experiments by William Phillips and his coworkers [47], they found that their six-beam molasses actually resulted in a temperature below the Doppler limit. This occurred because of the transfer of populations between different magnetic Zeeman sub-levels in the ground state configuration as the atoms move through the spatial standing wave produced by pairs of counter-propagating molasses beams. The atoms lose kinetic energy as they move up the hills of the spatial standing wave, which is why this type of cooling is called Sisyphus cooling (named after the mythological Greek king who was

punished for his cruelty by having to roll a giant rock up a hill continuously for eternity). Unfortunately, ordinary Sisyphus cooling does not work for lithium because the excited state structure of the $^2P_{3/2}$ state is unresolved.

In order to perform sub-Doppler cooling with lithium, we have to play some tricks on the D1 line. The trick we will play is called Λ scheme gray molasses which was first demonstrated in lithium in 2013 [48].

The way this works is as follows. Image you have three energy levels in your atom given by two ground states $|1\rangle$, $|2\rangle$ and an excited state $|3\rangle$, where the transitions from $|1\rangle$ to $|3\rangle$ and from $|2\rangle$ to $|3\rangle$ are optically allowed, meaning they have an electric dipole transition. Next, we shine one laser beam that connects states $|1\rangle$ to $|3\rangle$ and $|2\rangle$ to $|3\rangle$, both at a blue detuning δ as shown in Figure 3.6.

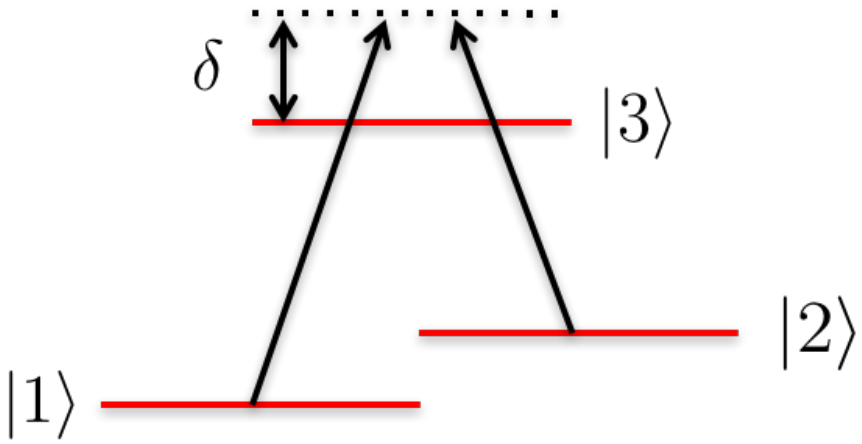

Figure 3.6: Λ scheme.

The presence of the laser beams create a coherent superposition of the ground states that is not optically coupled to the excited state. We call this superposition a dark state $|D\rangle$. Orthogonal to this state, is a bright state $|B\rangle$, which can optically couple to the excited state.

Suppose both laser beams form a standing wave at the atoms. Then the bright state's

energy will be spatially modulated by the light shift from the laser beams. Because states $|D\rangle$ and $|B\rangle$ are not eigenstates of the kinetic energy operator, the dark state can couple into the bright state. The most likely place for this to happen is at an energy minimum of the bright state. The atom then moves up a hill, converting its kinetic energy to potential energy. Then, when the atom is high enough in energy, it undergoes a simultaneous absorption and stimulated emission event. The result of this whole process is that an amount of kinetic energy equal to the height of the hill is lost, as shown in Figure 3.7.

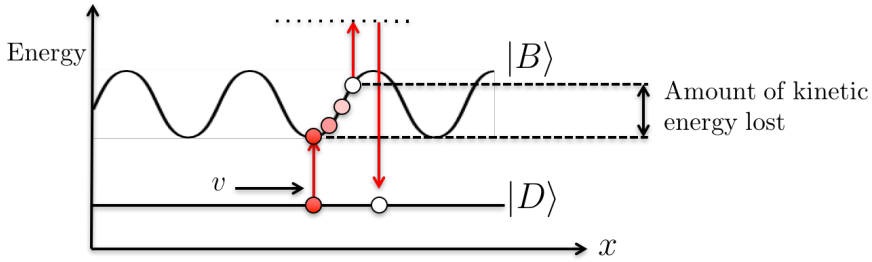

Figure 3.7: Grey molasses. The redness of the atom indicates the amount of kinetic energy of the atom.

Our gray molasses works by coupling together the ${}^2S_{1/2}$ $F = 2$ and ${}^2S_{1/2}$ $F = 1$ ground states to the ${}^2P_{1/2}$ $F = 2$ excited states as depicted in Figure 3.8. We accomplish this by shining two beams onto the atoms: one horizontal beam in a bow-tie retro-reflected set-up to form a standing wave in the x and y directions and one retro-reflected vertical beam to form a standing wave in the z direction. The gray molasses (GM) light is produced from a dedicated home-built tapered amplifier that puts roughly 35 to 40 mW of ${}^2S_{1/2}$ $F = 2$ to ${}^2P_{1/2}$ $F = 2$ laser light in each GM beam. We use a home-built EOM operating at 803.5 MHz to generate the necessary 1 to 2 percent side band that addresses the ${}^2S_{1/2}$ $F = 1$ to ${}^2P_{1/2}$ $F = 2$ transition. The GM beams are roughly 6.5 Γ blue detuned from the ${}^2P_{1/2}$ $F = 2$ state to mitigate single-photon absorption events and maximize the likelihood of the two-photon simultaneous absorption and stimulated emission event.

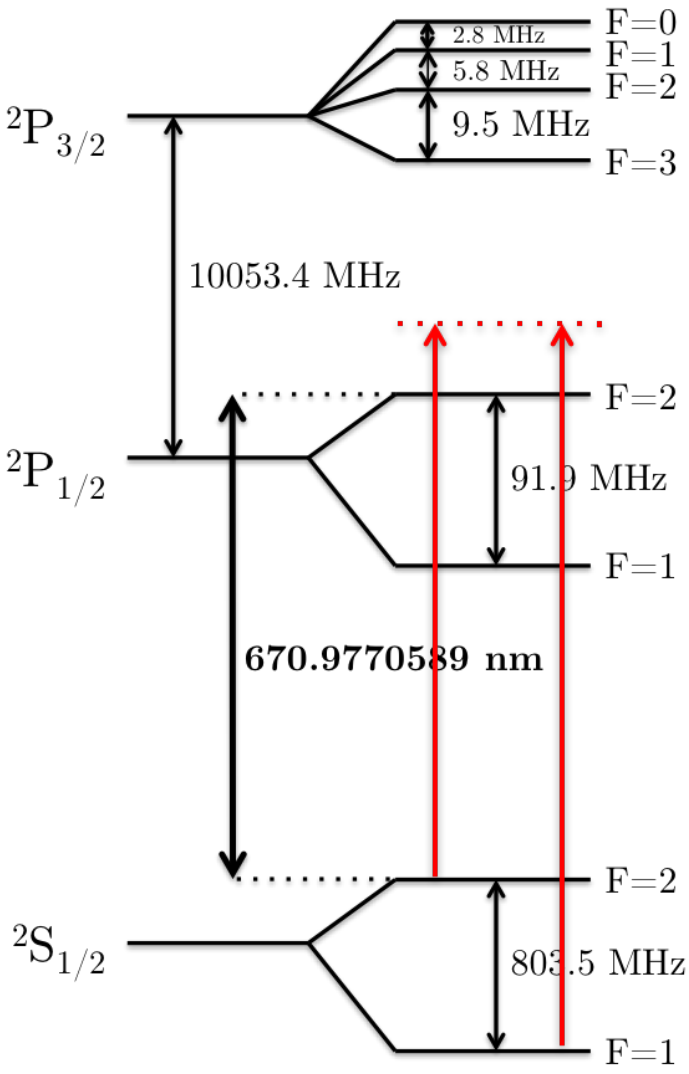

Figure 3.8: Grey molasses level diagram.

We varied the relative detuning between the two colors of light to check the effective temperature after applying 1 ms of gray molasses light. This data is shown in Figure 3.9. We typically operate gray molasses at 0 relative detuning to reach temperatures of 50 to 60 μK.

I have included absorption imaging pictures of our post gray molasses cloud in Figure 3.10.

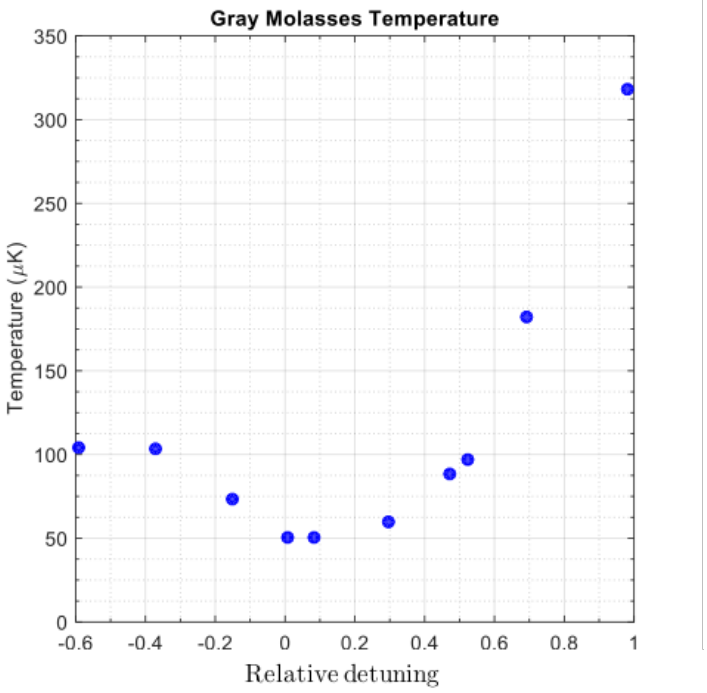

Figure 3.9: Temperature as a function of relative detuning between the two GM colors in units of Γ.

3.6 Optical Pumping

To confine the atoms in the magnetic trap, we want all the atoms to be in the stretched magnetic state ground state: $|F = 2, m_F = 2\rangle$. By conservation of angular momentum, having all of the atoms in the $|2, 2\rangle$ state mitigates spin-changing collisions that would result in significant atom loss in the magnetic trap.

We perform optical pumping on the D1 line to transfer all the atoms into the $|2, 2\rangle$ state. A schematic of how this is done is shown in Figure 3.11. By circularly polarizing the D1 light and applying a several Gauss bias magnetic quantization field, we can induce the atoms to absorb laser light that drives $\Delta m_F = +1$ or σ^+ transitions. Once the atoms are pumped to the $|2, 2\rangle$ state, they become dark to the pumping light and no longer scatter any photons. This shut-off of pumping is crucially important to prevent heating

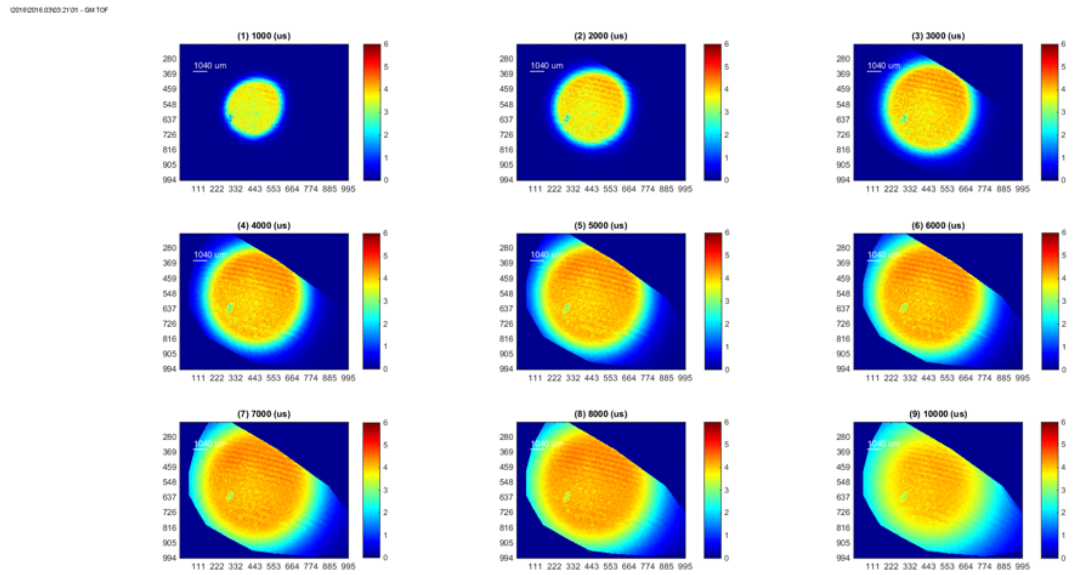

Figure 3.10: Absorption images after gray molasses. Each image is taken at a different time-of-flight (noted above each image). The atomic cloud is measured to be at a temperature of 60 μK by fitting the size of the cloud as a function of the time-of-flight. The imaging light is clipped by the supports inside the main chamber.

of the atomic cloud after gray molasses. Optical pumping on the D2 line is a bad idea because the D2 line is not very well spectroscopically resolved. In particular, performing pumping on the D2 $F = 2$ to $F' = 2$ line causes atoms to cycle photons on the D2 $F = 2$ to $F' = 3$ states, resulting in significant heating. To perform the pumping, we use our vertical gray molasses beam and change the relative detuning between the two colors of light to prevent simultaneous absorption and stimulated emission of the two colors. Not changing the relative detuning from the gray molasses scheme is bad because a photon from the stimulated emission event would cause the atom to undergo a $\Delta m_F = -1$ transition which we don't want.

To prevent center of mass movement of the cloud in the vertical direction during D1 pumping, we actually retro-reflect the pumping beam back onto the atoms. The retro-reflection mirror does not change the polarization of the light with respect to the

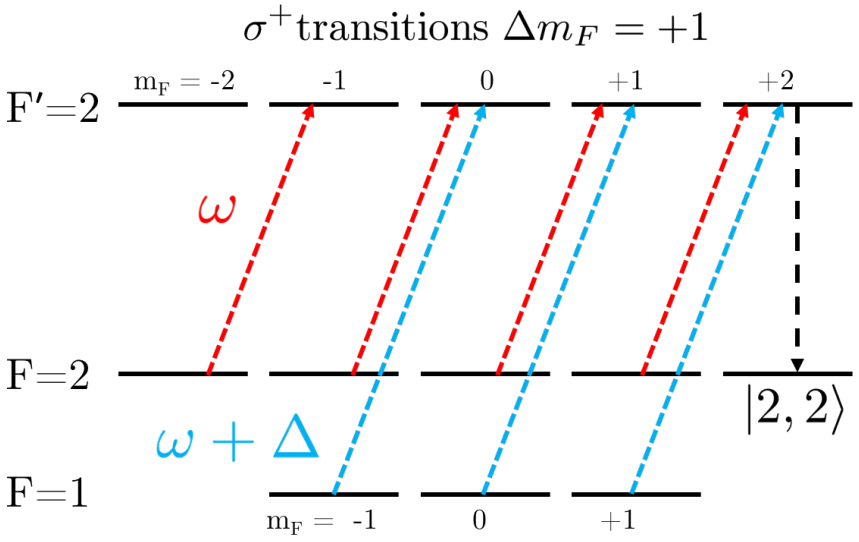

Figure 3.11: D1 optical pumping.

direction of the magnetic field, which means the retro-reflected pump beam continues to drive σ^+ transitions but imparts momentum that opposes the initial pumping beam to mitigate center of mass movement of the atomic cloud. The pumping beam contains about 80 mW of laser power. The $F = 2$ to $F' = 2$ color is blue-detuned by about 5 Γ (with roughly 54 mW of power) and the $F = 1$ to $F' = 2$ color is blue-detuned by about 4 Γ (with roughly 27 mW of power).

We can transfer nearly 100% of the atoms to the $|2, 2\rangle$ state in about 450 μs, as depicted in Figure 3.12.

3.7 RF evaporation in magnetic trap

After optical pumping, the atoms have heated to about 100 μK. The next thing we do is snap on a magnetic trap and ramp the field gradient to the maximum value (500 A of current to create a field gradient of 422 G/cm) to increase density and encourage scattering between the atoms. We then perform radio-frequency (RF) evaporation in the

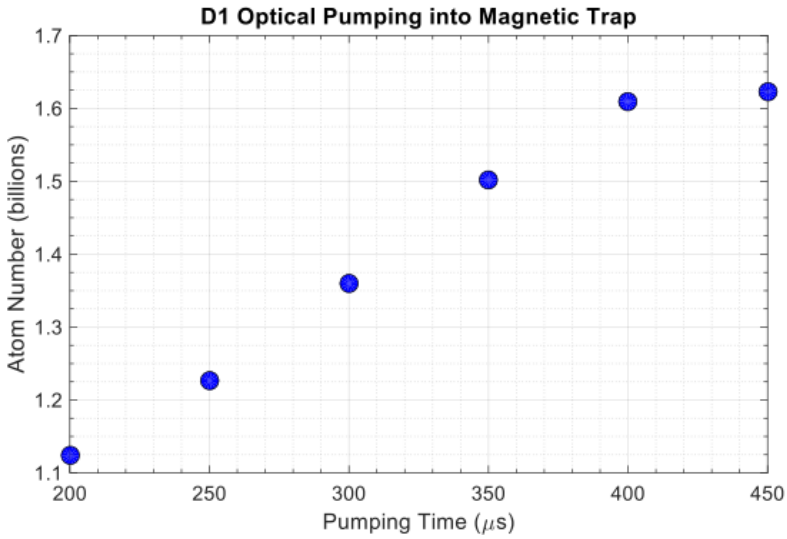

Figure 3.12: Trapped $|2,2\rangle$ atom number versus D1 optical pumping time. Nearly 100% state conversion is achieved within 450 μs.

optically plugged quadrupole magnetic trap to lower the temperature. This works just like blowing the top layer of atoms off a cup of coffee. The radio-frequency light is used to selectively remove the hottest atoms from the trap. The hottest atoms have the highest energies which means they move the farthest away from the center of the magnetic trap and define the spatial edge of the atomic cloud. In combination with the Zeeman shift from the magnetic trap, the RF drive flips the atomic states at the farthest edges of the atomic cloud from the magnetically trappable $|2,2\rangle$ state to the magnetically un-trapped $|1,1\rangle$ state. No longer trapped, the hot $|1,1\rangle$ atoms then exit the trap region and the atomic cloud equilibrates to a lower temperature via atom-atom collisions. A cartoon of this is shown in Figure 3.13.

We begin our radio-frequency sweep from about 1 GHz (which addresses a spatial location beyond the physical extent of the atomic cloud) and end the radio-frequency sweep at a value a little higher than the ground state hyperfine splitting, typically 805 or 806 MHz. We perform this RF sweep in four linear stages while reducing the magnetic field gradient at the same time. The magnetic field gradient must be relaxed because

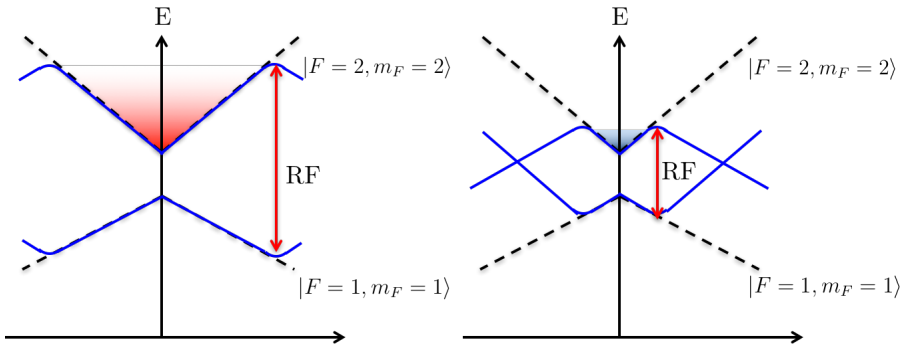

Figure 3.13: Radio frequency evaporation. The radio-frequency light flips the atomic states at the furthest edges of the atomic cloud from the magnetically trappable $|2,2\rangle$ state to the magnetically un-trapped $|1,1\rangle$ state. As the frequency of the RF light is lowered, the hottest atoms continue to escape and the rest of the cloud continuously equilibrates to a colder temperature.

the density increases to above 10^{13} cm^{-3} as the atoms evaporate. If the density becomes higher than 10^{13} cm^{-3}, then three-body loss begins to kill the number of atoms in the trap.

Another potentially devastating loss mechanism in the magnetic trap is Majorana loss. Majorana transitions occur when atoms confined in a magnetic trap make spin-flip transitions to a magnetically un-trapped state near the field zero of the magnetic trap [49]. These spin-flip transitions happen when the spin of the atom is not able to adiabatically follow the field direction and the "quantization" axis is lost. To prevent these non-adiabatic transition, we use a 532 nm blue-detuned plug beam focused onto the magnetic field zero to push atoms away.

There are two crucially important considerations for RF evaporation in a magnetic trap to be performed correctly. 1) If there is a magnetic bias field on the magnetic trap, then the center of the magnetic trap will move as the field gradient is ramped down. 2) If the center of the trap moves, then the plugging beam no longer plugs the magnetic-field zero of the trap. This means shimming the magnetic trap to remove any DC magnetic offset is critically important.

To properly magnetically shim the magnetic trap, we take absorption images of the magnetic trap at all field gradients and plot the position of the cloud as a function of the field gradient. We then change the current running in our magnetic shim coils to prevent any movement of the center of the atomic cloud as the field gradient is decreased. We do this in all three dimensions using two sets of cameras on the vertical and horizontal axes. Additionally, it is important the atomic cloud resulting from gray molasses is centered in the center of the magnetic trap (this requires that the MOT is also centered on the magnetic trap) to prevent swinging oscillations (and therefore heating) of the atomic cloud in the magnetic trap.

To properly plug the magnetic trap, we focus 10 W of 532 nm light on to the magnetic field zero to push atoms away. This beam is focused to a $1/e^2$ waist of 15 μm (D4σ = 30 μm). Absorption images of how the magnetic trap looks after radio-frequency evaporation as we vary the focus position of the plug beam is shown in Figure 3.14. The magnetic trap is properly plugged at 7 turns of the translation stage holding a refocusing lens.

At the end of radio-frequency evaporation, we typically have 60 million atoms at a density of 10^{12} cm^{-3} with a temperature of 10 μK. Unfortunately, the scattering length in the $|2,2\rangle$ state is -27 a_0 (attractive) which means the atoms barely scatter and if they do, they clump up to form a solid. One can make a BEC with this scattering length, but it is unstable and typically limited to a few thousand atoms [17]. To fix this, we load the atoms into a crossed optical dipole trap and then use the Feshbach resonance in the $|1,1\rangle$ state to generate a roughly 600 a_0 scattering length and then optically evaporate to a BEC.

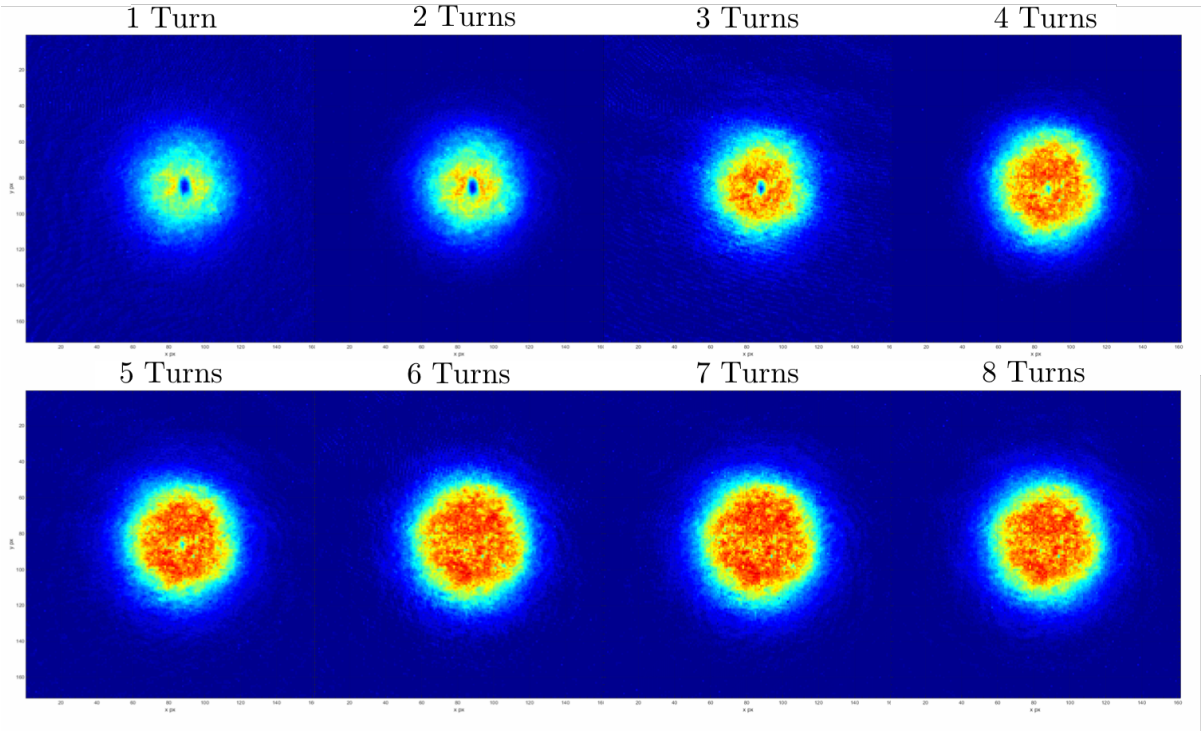

Figure 3.14: Absorption images of the atomic cloud after RF evaporation for various positions of the plug beam focusing lens. The hole resulting from the 532 nm plug beam is clearly visible at 1 turn of a translation stage micrometer that moves a refocusing lens. At 7 turns, the plug beam is properly focused on the field zero and the atom number in the magnetic trap skyrockets.

3.8 Optical Evaporation

As mentioned in the previous section, we have to transfer the atoms to the $|1,1\rangle$ state. To do this, we load roughly 25% of the RF evaporated atoms into a crossed optical dipole trap and then apply a small bias magnetic field to prevent the atoms from losing their spin configuration. We then sweep the RF field in 65 ms from 809.6 MHz to 807.5 MHz to perform a Landau-Zener passage from the $|2,2\rangle$ state to the $|1,1\rangle$ state. While performing the 65 millisecond sweep, we switch the MOT coils from an anti-Helmholtz to Helmholtz configuration and then apply a 729 G DC magnetic field on the atoms to access the Feshbach resonance.

A few notes on the Feshbach resonance. Randy Hulet and his team at Rice University characterized the scattering length in the $|1,1\rangle$ state as a function of magnetic field in [18]. The Feshbach resonance in lithium follows the typical form:

$$a = a_{bg}\left(1 + \frac{\Delta}{B - B_\infty}\right), \tag{3.10}$$

where $a = -24.5\ a_0$, $\Delta = 192.3$ G, and the resonance location at $B_\infty = 736.8$ G. The scattering length zero-crossing is located at $B_0 = 543.5$ G and the scattering length has a slope in the vicinity of the zero-crossing of $0.08\ a_0$/G. We calibrated our experimental Feshbach magnetic fields to the zero-crossing at 543 G using size measurements of the BEC. We confirmed the location of the Feshbach resonance at 737 G by holding the atoms in a crossed optical dipole trap and examining the atom loss rate in the trap after a hold time of several seconds. After calibrating our Feshbach fields to the zero-crossing, our prediction of the Feshbach resonance location of the resonance matched the magnetic field that resulted in maximum atom loss of the held crossed optical dipole trap.

Our crossed optical dipole trap is produced from two optical dipole trapping beams, called ODT1 and ODT2, which intersect at approximately 90 degrees. The two beams are produced by a high power Gaussian 1064 nm laser and each have $1/e^2$ diameters of 180 μm. The trap depths of our ODTs are typically in the hundreds of μK which means if we adiabatically turn on the ODTs after the radio-frequency evaporation, then the atoms will sit near the bottom of the Gaussian beam which can thus be modeled by a harmonic oscillator potential. The harmonic oscillator potential that results from a single optical dipole trap is given by:

$$U(r,z) \approx -U_0\left[1 - 2\left(\frac{r}{\omega_0}\right)^2 - \left(\frac{z}{z_R}\right)^2\right] \tag{3.11}$$

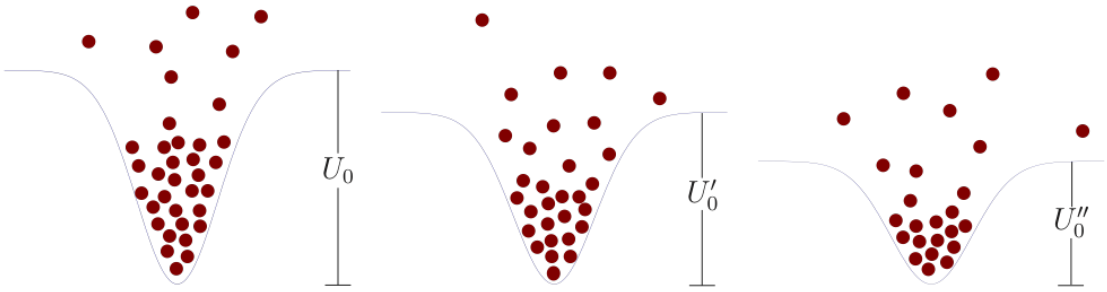

Figure 3.15: Optical evaporation. At each time step, the depth of the confining optical potential is reduced. The hottest atoms escape the trap and the remaining cold atoms interact with each other to equilibrate to a colder temperature.

where U_0 is the depth of the trap, ω_0 is the waist and z_R is the Rayleigh range.

Optical evaporation proceeds by simply lowering the intensity of the crossed optical dipole trap as shown in Figure 3.15. The functional form of the optical evaporation is an exponential with a time constant that is half of the evaporation time. Typically our optical evaporation is performed in 4.5 seconds.

Figure 3.16 shows the formation of our lithium BEC as a function of the final crossed optical dipole trap power noted on each image, given as a fraction of the initial optical power U_0. These absorption images after a 3000 μs time-of-flight show how a thermal cloud in the left most panel becomes a nearly 95% pure condensate in the right most panel. We typically have 200,000 atoms in our BEC.

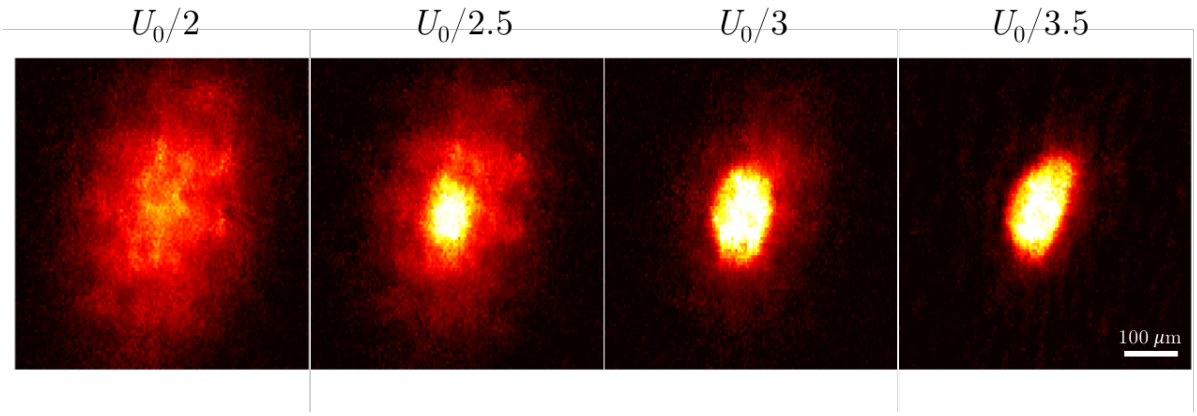

Figure 3.16: Birth of the condensate as a function of the final crossed optical dipole trap power with respect to the initial power, U_0. The leftmost panel is a thermal cloud. The rightmost panel is a nearly pure Bose-Einstein condensate. The absorption images are taken after a time-of-flight of 3000 μs.

Chapter 4

Lithium Experimental Apparatus

4.1 Machine Overview

The entirety of the machine sits on two optical tables: one for laser systems and one for the vacuum chamber.

A Solidworks rendering of the lithium vacuum chamber is shown in Figure 4.1. The central feature of the lithium machine is the main chamber. This is a large 316L stainless steel chamber with nine large optical view-ports. There are two large re-entrant windows on the top and bottom of the main chamber that house the high-current electromagnets used to magnetically trap lithium atoms and apply the Feshbach fields. Ultrahigh vacuum is maintained inside the main chamber with a 75 l/s Agilent ion pump and a titanium sublimation pump (Ti-sub). Surrounding the main chamber are three levels of continuously cast aluminum breadboards and three pairs of magnetic shim coils to cancel out Earth's magnetic field and apply magnetic bias fields to the atoms.

To reach ultrahigh vacuum pressures, the entire apparatus was baked at 170°C for eight days while maintaining pumping to remove water vapor and any surface contaminants. The pressure inside the main chamber typically sits at 10^{-12} Torr. When the

pressure begins to creep back up to 10^{-11} after several months, we typically fire the titanium sublimation pump to lower the pressure back to 10^{-12}.

Figure 4.2 shows where the various cooling stages occur in the machine.

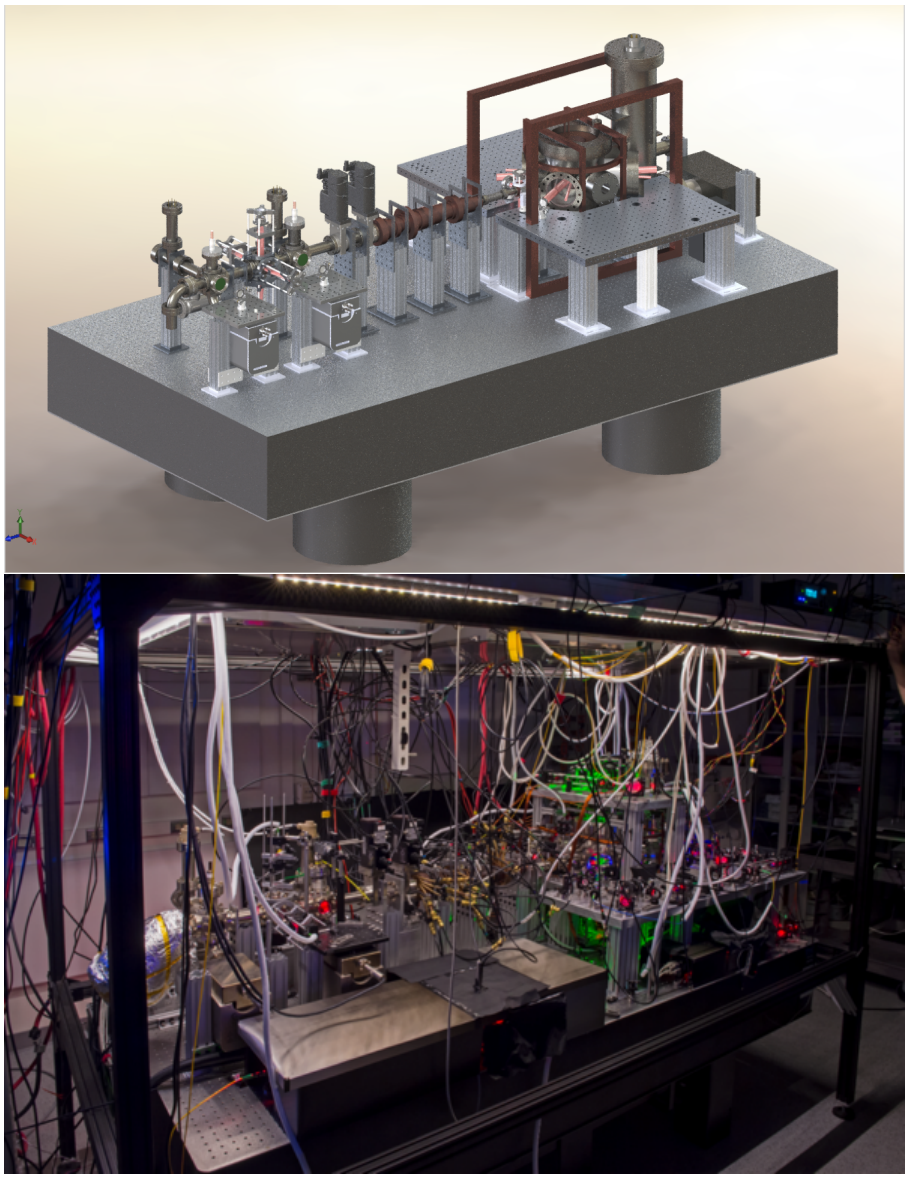

Figure 4.1: Solidworks rendering of the lithium machine (top) and an actual photo of the lithium machine (bottom). The white tubes dangling from the cloud in the bottom picture are optical fibers that couple laser light over from the optical table (not shown).

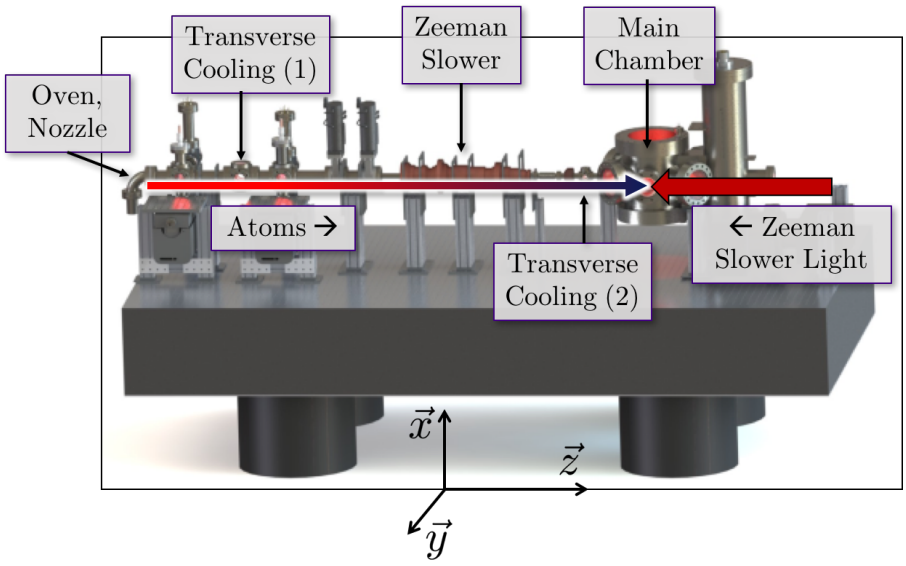

Figure 4.2: Illustration of where the various laser cooling stages occur in the apparatus. Magneto-optical trapping, gray molasses, RF evaporation, and optical evaporation all occur in the main chamber.

4.2 Oven and Nozzle

A stainless steel cup initially filled with 25 grams of lithium serves as our atomic source. This cup is heated with a band heater to 450 °C to produce a hot lithium gas. This resultant Boltzmann gas is then collimated by a micro-capillary array of stainless steel tubes [50] to produce an atomic beam with an approximate root mean square axial velocity of 1500 m/s. A diagram of our nozzle is shown in Figure 4.3. The micro-capillaries are constrained to be horizontal by stacking them in a hexagonally packed lattice. This multichannel effusive oven nozzle improves beam collimation over traditional single-orifice nozzles and therefore provides longer oven lifetimes. To prevent clogging of the nozzle, the nozzle flange is always held at a temperature 100 °C hotter than the temperature of the cup. A photo of the atomic beam immediately after the oven is shown in Figure 4.4.

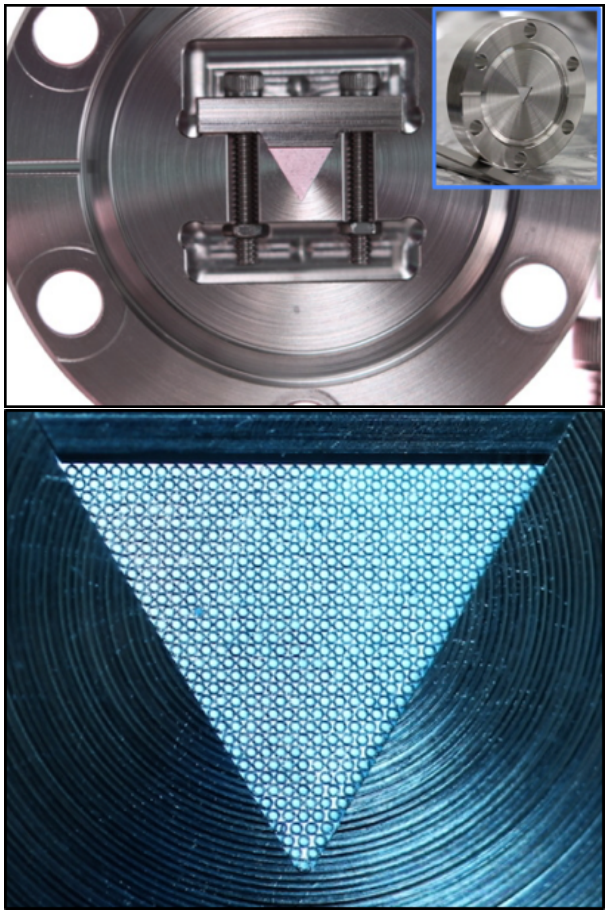

Figure 4.3: The micro-capillary nozzle. Each tube has an inner diameter of 200 μm.

4.3 Transverse Cooling

We apply 2D optical molasses both after the nozzle and after the Zeeman slower to collimate the atomic beam and prevent beam explosion. A diagram of our 2D transverse cooling set-up before the Zeeman slower is shown in Figure 4.5. We found empirically that the optimal tranvserse cooling set-up before the Zeeman slower only required the vertical beam, suggesting that the atomic beam is directed slightly upwards. This vertical transverse cooling beam contains 4 mW of cooling light and 1 mW of repump light.

Both the x and y directions are used in the transverse cooling after the Zeeman slower.

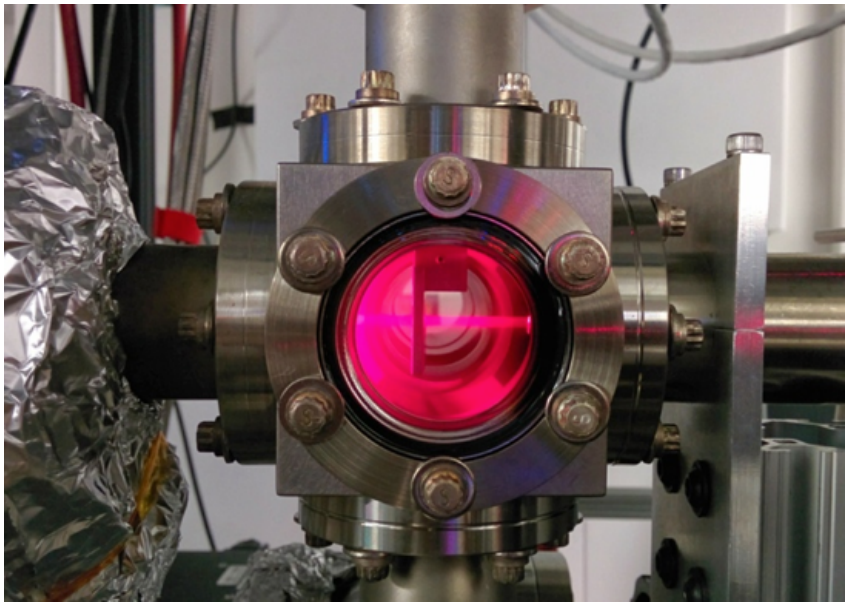

Figure 4.4: Flux of the atomic beam after the nozzle. The red beam is fluorescence of the atomic beam from the slower beam. The crumple of aluminum foil to the left encases the oven.

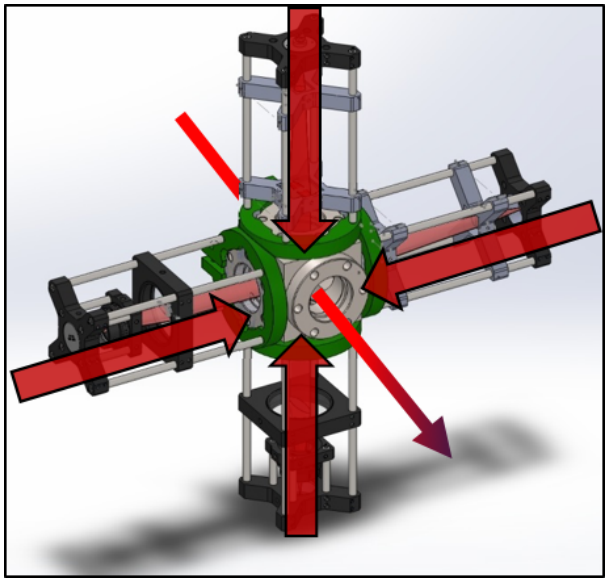

Figure 4.5: Diagram depicting four beam molasses.

The post Zeeman slower transverse cooling contains 2 mW of cooling light and 2 mW of repump light.

4.4 Zeeman Slower

The next cooling stage is the Zeeman Slower (Figure 4.6) where the magnetic field from a tapered solenoid mediates the radiation pressure force from a counter-propagating red detuned cooling laser beam called the slower beam.

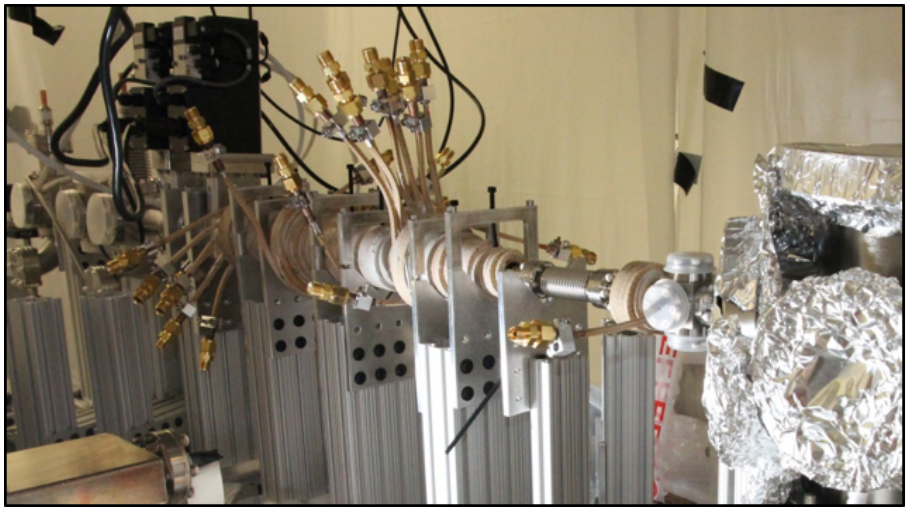

Figure 4.6: Early picture of the Zeeman slower magnet.

Initially, the Doppler shift of the axially traveling atoms is compensated by the red detuning of the beam and the Zeeman shift due to the entrance field of the slower. As they absorb and isotropically re-emit photons the resultant effect is to decelerate their axial velocity. The spatially dependent Zeeman shift balances the changing Doppler shift, resulting in monotonic cooling. The measured field profile of the Zeeman slower is shown in Figure 4.7.

The Zeeman slower magnet has four sections (A, B, C, and D) constructed from low gauge, hollow wire to allow water cooling. The wire is wound together as a tapered solenoid and held in place using thermally conducting, electrically insulating epoxy (Duralco NM25). The magnet is tapered so that it compensates the Doppler shift with an applied Zeeman shift. Our Zeeman slower is designed to be a spin-flip slower that cap-

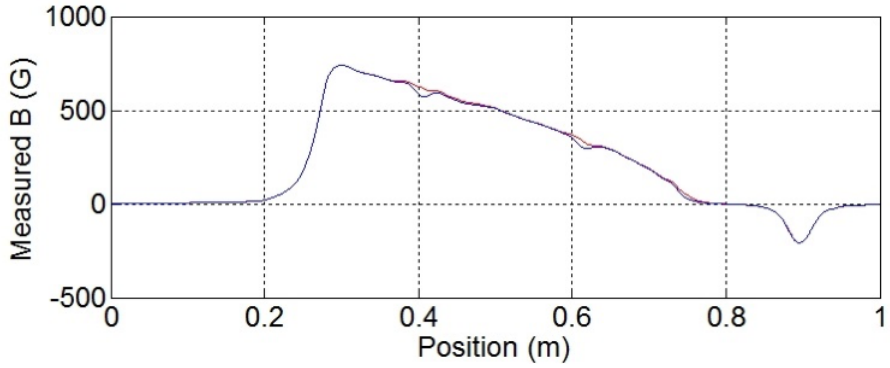

Figure 4.7: Measured magnetic field from Zeeman slower. The first dip at a position of 0.4 m is smoothed by a shim coil (called the AB shim) that operates with 5 amps of current. We empirically found that the other magnetic field dips do not need to be shimmed to maximize atom number in the MOT.

tures atoms moving with a velocity of 1000 m/s or below and reduces them to a speed of 50 m/s (this is the capture velocity of our MOT). The advantage of using a spin-flip Zeeman slower is that the Zeeman slower laser light is far detuned from the zero-field cycling transition, mitigating its effect on the magneto-optical trap.

Sections A, B, C, and D run currents of 31.7 A, 56.3 A, 29.5 A, and 44 A, respectively. The currents are optimized to maximize the loading rate of the magneto-optical trap. Because of the high currents, the Zeeman slower sections are wound from square, hollow wire to allow water cooling.

Sections A and B are each powered by Sorenson DLM8-75 power supplies. Section C is powered by an Acopian 0-8 V, 40 A supply and Section D is powered by an Acopian 0-8V, 64 A supply. All of these power supplies are hooked up to 100 A mosfets to enable quick turn-off and turn-on of the Zeeman slower currents.

4.5 Electromagnets

A picture of one of the MOT coils is shown in Figure 4.8. There are two of these coils, housed in the top and bottom buckets of the main chamber. Both of these coils form “two

pairs" of coils, an inner coil pair and an outer coil pair. The inner coil pair is powered by a TDK Lambda 500A, 20V supply that we call the ESS. The outer coil pair is powered by a TDK Lambda Genesys 500A, 20V power supply that we call the GSS. Both of these power supplies have similar ramping speeds, which allows the user to consider both the inner coil and outer coil pairs as one large anti-Helmholtz or Helmholtz pair. The current supplies are connect to IGBTs to allow for rapid turn off (hundreds of μs) of the currents. However, to rapidly turn on the magnetic trap after gray molasses, we use a 500V bank of capacitors connected in parallel with the inner MOT coils to snap on a field gradient of 80 G/cm in 100 μs. These capacitors are charged between each experimental run of the machine during the MOT loading phase.

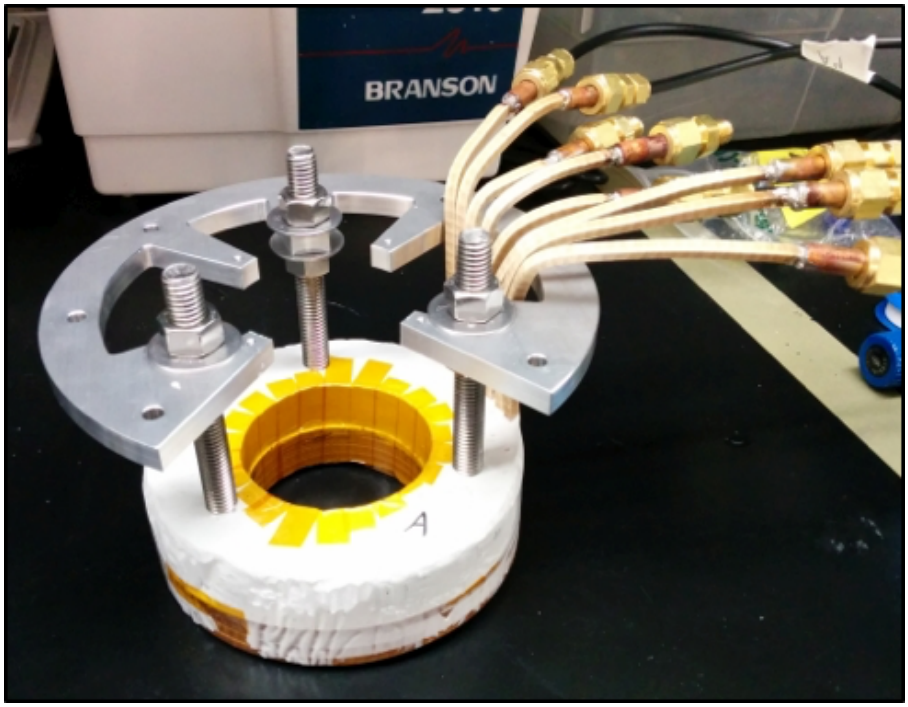

Figure 4.8: Picture of one of the MOT coils after winding. The magnets are constructed from hollow square wire to allow water cooling. The water cooling lines (plastic black tubes) are shown in the top right. These are connected to the MOT magnet wires via Swagelok tube fittings. The current source is attached to the copper tubes with aluminum lugs (not shown).

A diagram of the coils in anti-Helmholtz configuration is shown in Figure 4.9. In this

configuration, both the GSS and ESS work together to produce a magnetic quadrupole trap. This is the configuration used in the magneto-optical trap and in the magnetic trap.

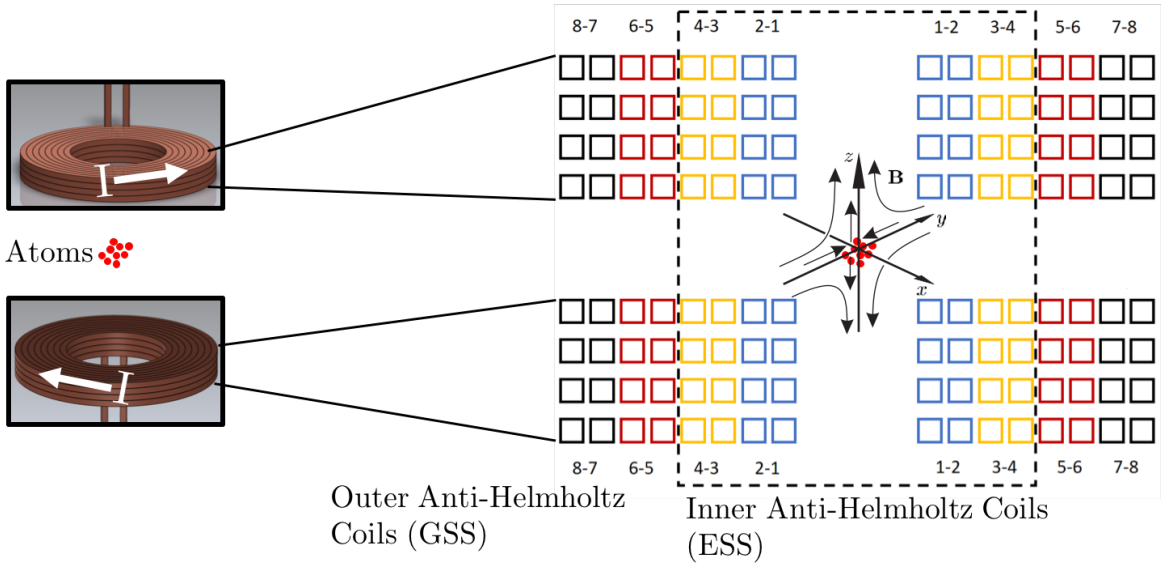

Figure 4.9: Anti-Helmholtz configuration.

A diagram of the coils in the Feshbach field configuration is shown in Figure 4.10. In this configuration, the GSS works in a Helmholtz configuration to create a static magnetic field that points downward on the atoms. The ESS coils are switched such that half of its coils produce a static magnetic field in the upwards direction and the other half of its coils produce a static magnetic field in the opposing direction. The point of this is that the magnetic field curvature from the inner coil set helps to cancel the magnetic field curvature from the outer coil set.

The configurations of the electromagnetic coils are switched from anti-Helmholtz to Helmholtz configuration in 20 ms by an H-bridge circuit.

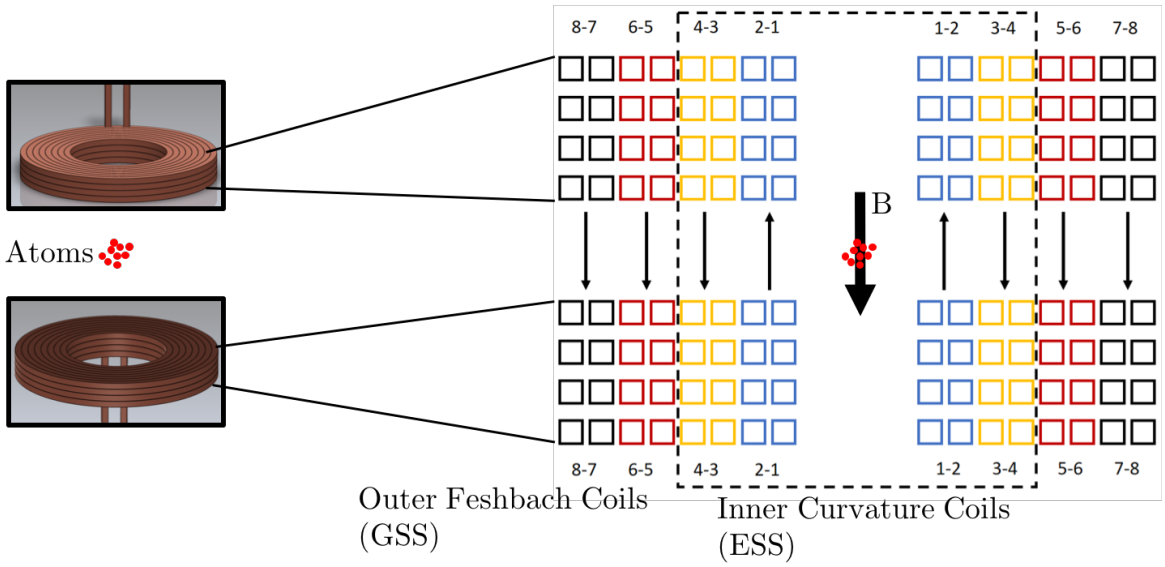

Figure 4.10: Helmholtz configuration.

4.6 Water Cooling

The electromagnets, IGBTs and Zeeman slower magnets all generate a significant amount of heat. To cool them down, we have a closed in-house water cooling system. An overview of this water cooling system is shown in Figure 4.11.

We fill the water cooling system with 90% distilled water and 10% isopropyl alcohol to clean out any contaminants. The Neslab chiller cools the water to 18 degrees Celsius and the booster pump (Pump PB1016S153 from Flint and Walling) is used to pressurize the lines with water at 100 PSI. This ensures that cold water passes through the lines rapidly enough to remove heat from the system. At the end of each day, we turn off the Booster pump and shunt the water through a filter to clean it.

A schematic of the water lines in the lithium machine is shown in Figure 4.12. The water lines are used to cool the MOT coils, the Zeeman slower coils, the IGBTs for the main magnets and the Nufern 1064 nm 50 W amplifier.

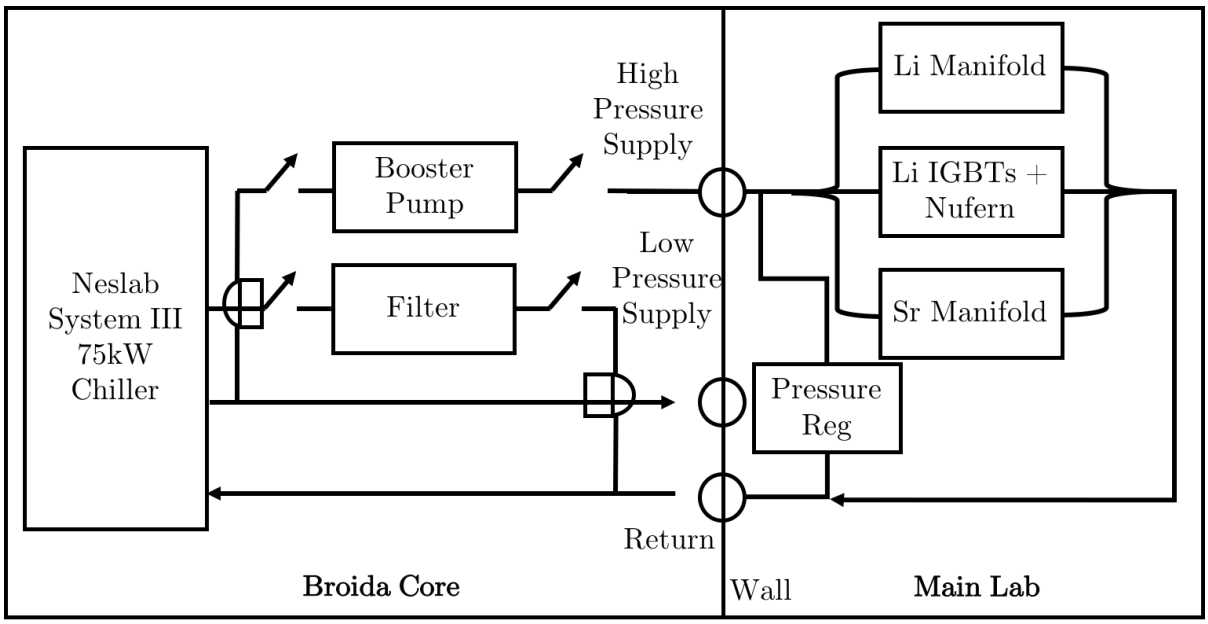

Figure 4.11: Overview of water cooling manifold.

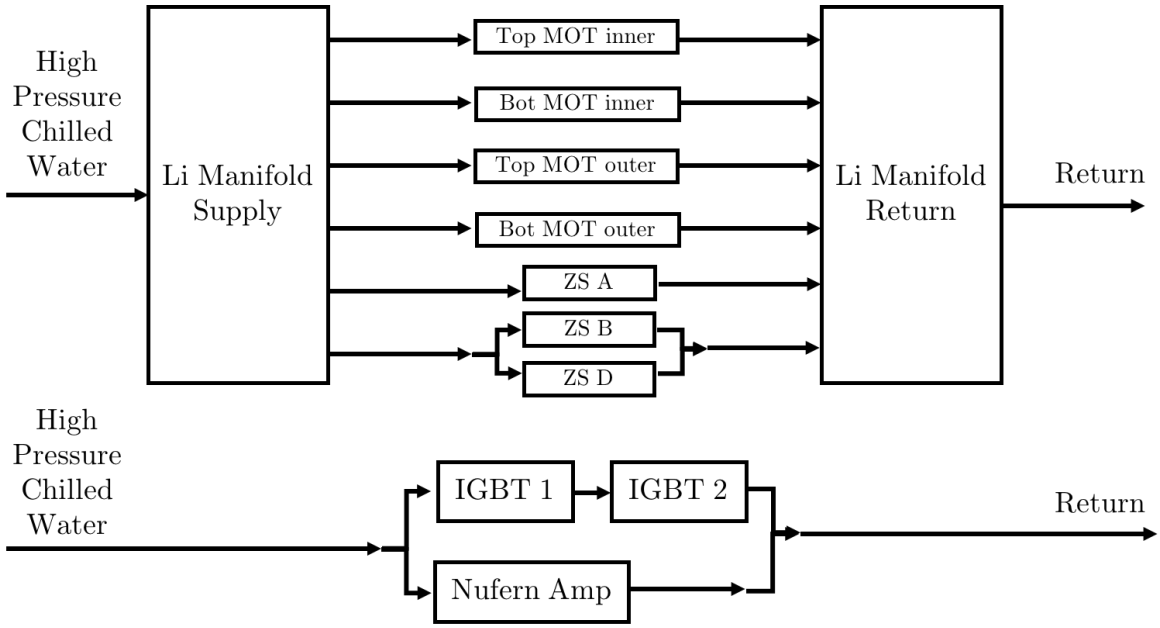

Figure 4.12: Overview of lithium water cooling lines.

4.7 671 nm Laser System

The main workhorse of the lithium experiment is the 671 nm laser system. This is the laser system responsible for the brunt of the laser cooling and trapping. The master laser is a Toptica TA pro that was initially rated to output 500mW but now only outputs 300 mW. The entirety of the 671 laser table is diagrammed in Figure 4.13.

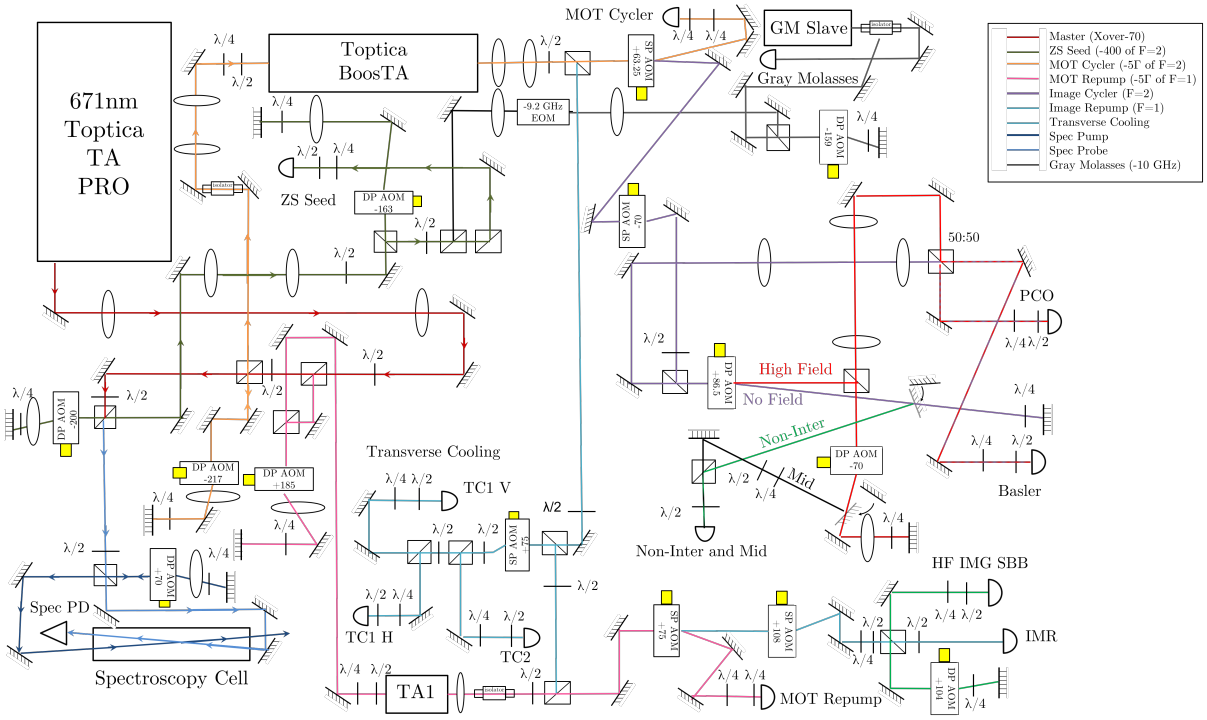

Figure 4.13: Overview of 671 nm laser table.

The master laser is locked to the crossover resonance on the D2 line using saturated absorption spectroscopy with a double-passed AOM. A frequency modulation signal from the Toptica control box adds sidebands on the double pass AOM to produce a lockable error signal. There are two main amplifying stages on the 671 laser table: a Toptica BoosTA that outputs 310 mW and a home-built TA (TA1) that outputs 450 mW. To bridge the gap between the D1 and D2 lines, we use a 9.2 GHz EOM (Model 4851 from

Newport). Additionally, we use injection locking to lock two slave diode lasers. One is used to frequency select the appropriate EOM sideband to produce GM light and is called the GM slave diode. Another slave diode is injection locked with the Zeeman slower seed light to produce the Zeeman slower beam.

We frequently use the Feshbach resonance to change the s-wave scattering length between atoms. This typically requires applying a 543 G field (zero-crossing) which we call the non-interacting region. We also apply a 729 G field to create strong interactions between atoms (this is the field we use to produce a BEC) which we call the high-field region. Additionally, we sometimes use roughly 40 a_0 of interactions which we call the mid-field interaction region. In varying the magnetic fields, the energy levels of the lithium atom split by hundreds of MHz and we have to use a cascade of AOMs to bridge these splittings. A plot showing how the transitions vary with magnetic field is shown in Figure 4.14. At each magnetic field, we have to change our imaging light frequency and this is done with the High-Field and Non-Inter pathways shown in the laser table diagram (Figure 4.13). Our main absorption imaging camera is an sCMOS PCO.edge 5.5 (from PCO) and we additionally use two small CMOS cameras from Basler (aca1920-25μm) to perform absorption imaging on different axes as needed.

To address all the various transitions in the lithium atom, we have to use about two dozen AOMs. One of my main projects as a junior graduate student was building the drivers for all of these AOMs. Figure 4.15 shows a diagram of a typical circuit for an 80 MHz visible wavelength range AOM.

Building a circuit to drive an AOM is rather straightforward. Most of the AOMs we have purchased in lab are from IntraAction. If you go to the IntraAction website, the specification sheets will tell you what the optimal RF power is for each AOM. As an example, the 80 MHz AOM at 671 nm requires 1 W of RF drive power (the necessary RF drive power for TeO_2 crystals typically varies as the square of the optical wavelength).

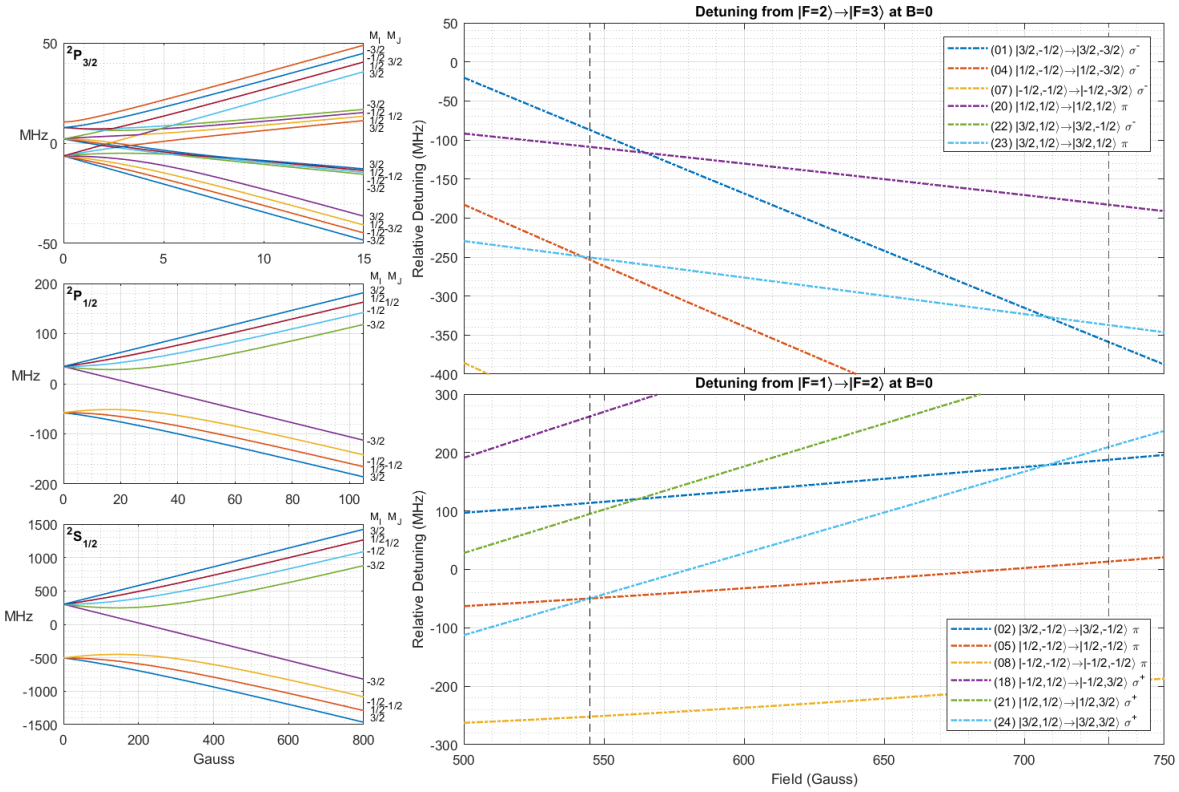

Figure 4.14: Splittings of the hyperfine states as function of magnetic field. Left panels show the splittings for the $^2S_{1/2}$, $^2P_{1/2}$, and $^2P_{3/2}$ hyperfine manifolds. The right panels show the change in the transition energy for the relevant imaging transitions on the D2 line.

1 Watt of RF drive power is equal to 30 dBm. We then go to the website of our favorite electronics manufacturer, Minicircuits, to find an 80 MHz voltage controlled oscillator. One of my favorites is the ZOS-100+. This has an output power of 9 dBm and an auxiliary port at -12 dBm you can use for monitoring the oscillator frequency. You then get an RF switch (so that you can turn the diffracted laser beam on and off quickly) and a voltage variable attenuator (so you can change the power in the diffracted laser beam). A nice RF switch is the ZX80-DR230+ and a nice VVA (voltage variable attenuator) is the ZX73-2500+. The RF switch will reduce the power from the VCO by 0.5 dB and the VVA will reduce the power further by 3 dB. This means the output RF power after these three components is 5.5 dBm. To get up to 30 dBm, we need an amplifier. I particularly

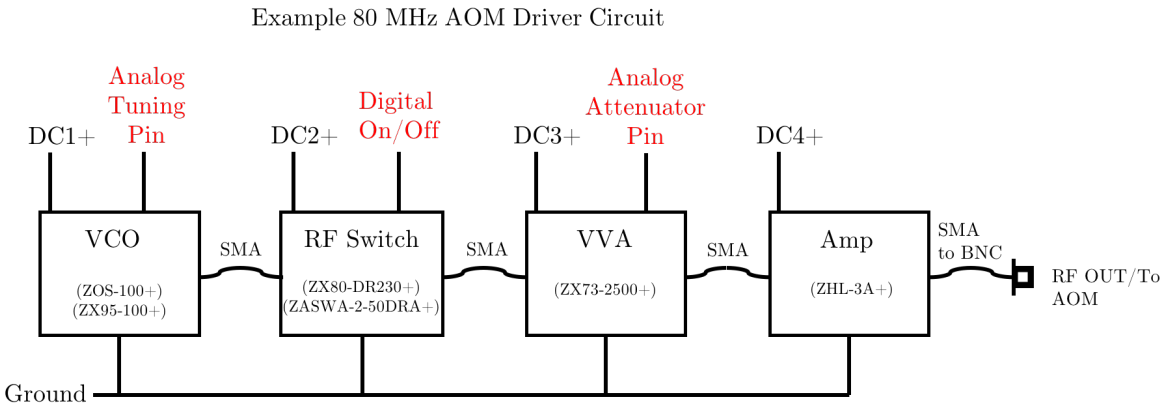

Figure 4.15: Overview of an 80 MHz AOM driver circuit with a few of my favorite parts. The analog tuning pin is used to change the frequency of the VCO (voltage controlled oscillator). The digital on/off is used to turn the RF on or off (tens of nanoseconds). The analog attenuator pin is used to change or modulate the RF power.

like the ZHL-3A+, which has a linear gain of 25.5 dBm at 80 MHz. This means, at the end of the amp, the total RF power is 31 dBm. You'll probably lose 1 dB in the BNC cable going to the AOM itself, which means the power delivered to the AOM will be 30 dBM or 1 Watt, as required. Spending time browsing RF components on Miniciruits and thinking of new ways to mix and match components has honestly been a pretty fun part of my graduate school experience.

The last portion of the 671 nm laser system is the gray molasses and D1 setup. A schematic of this is shown in Figure 4.16. A dedicated home-built tapered amplifier (TA2) generates the power necessary to produce the GM light and the pumping light. This optical set-up was placed on the machine table itself to avoid losing GM power to fiber coupling loss.

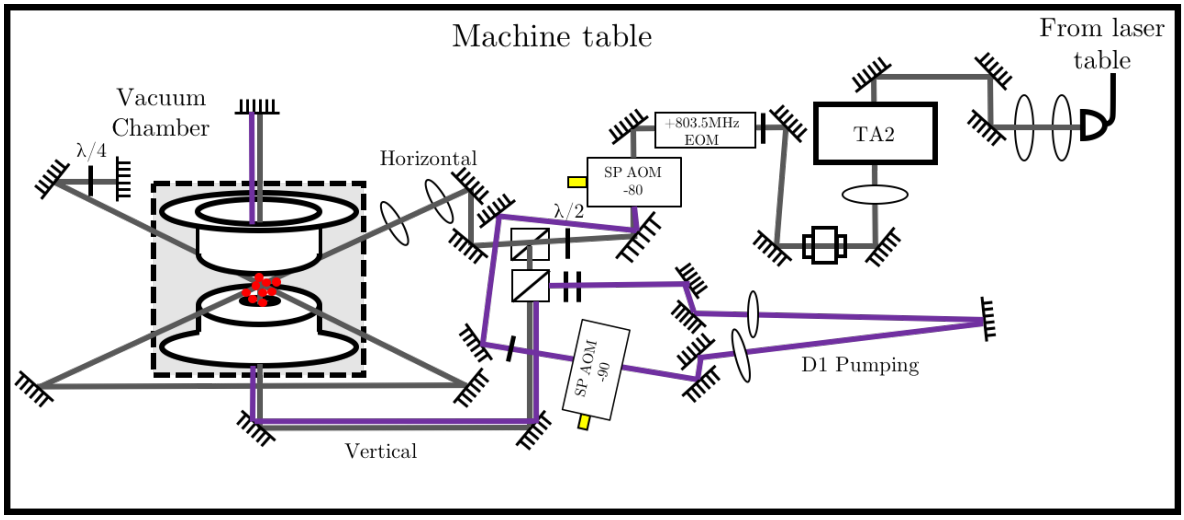

Figure 4.16: Gray Molasses and D1 pumping optical pathway.

4.8 532 nm Laser System

The 532 nm laser is a 10 W Lighthouse photonics Sprout. It's main and only job is to serve as a plug beam and prevent Majorana losses through the magnetic field zero of the magnetic trap during radio-frequency evaporation. A diagram of the beam pathway is shown in Figure 4.17. We initially planned to use an AOM to turn switch the laser on and off of the atoms, but the AOM distorted the shape of the laser beam and significantly affected the output power (we were only about to get a diffraction efficiency of roughly 70%). We opted to use a waveplate rotator (model RSC-104E) from Pacific Laser Equipment. This rotator can rotate 45 degrees in 300 milliseconds which is much faster than any rotator we could find from Thorlabs. You can program (with a serial connection) the rotator to perform a sequence of rotations after a trigger. After radio-frequency evaporation, the plug beam is adiabatically turned off by diverting all of its power into a beam dump in 300 ms.

The piezoelectric mirror (Model 8821 from Newport) shown in the Figure 4.17 is used to precision align the plug beam onto the field zero. We do this by taking absorption

images of the RF evaporated cloud and then moving the plug beam several piezo-electric steps at a time to maximize atom number.

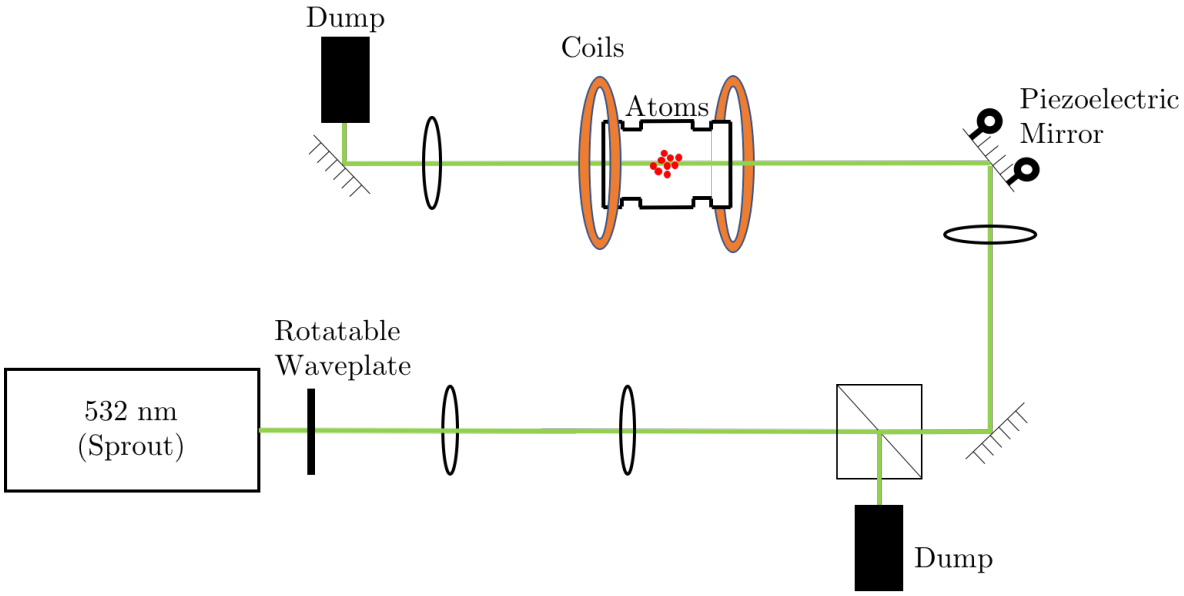

Figure 4.17: 532 nm laser setup.

4.9 Radio-Frequency Antenna

A picture of the radio-frequency antenna we use to shine RF light on the atoms is shown in Figure 4.18. The ribbon antenna is mounted inside a 3D printed holder that presses up against the inside of the top MOT coil. We initially planned to use an antenna inside the chamber to perform RF transitions, but the leads became brittle during the main chamber bake and broke when we tried to solder them.

To solve that problem we had to create our ribbon antenna to address the atoms from the outside of the main chamber. This was no easy task because it is hard to get RF to couple inside our giant steel main chamber. The game plan quickly became to make a coil antenna to sit as close as possible to the atoms. This was accomplished by having a

ribbon antenna encircle the window in the top bucket. We went through nearly twenty iterations of an antenna before we were able to construct an antenna that did not have significant attenuation of RF coupling in the region between 800 MHz and 1 GHz.

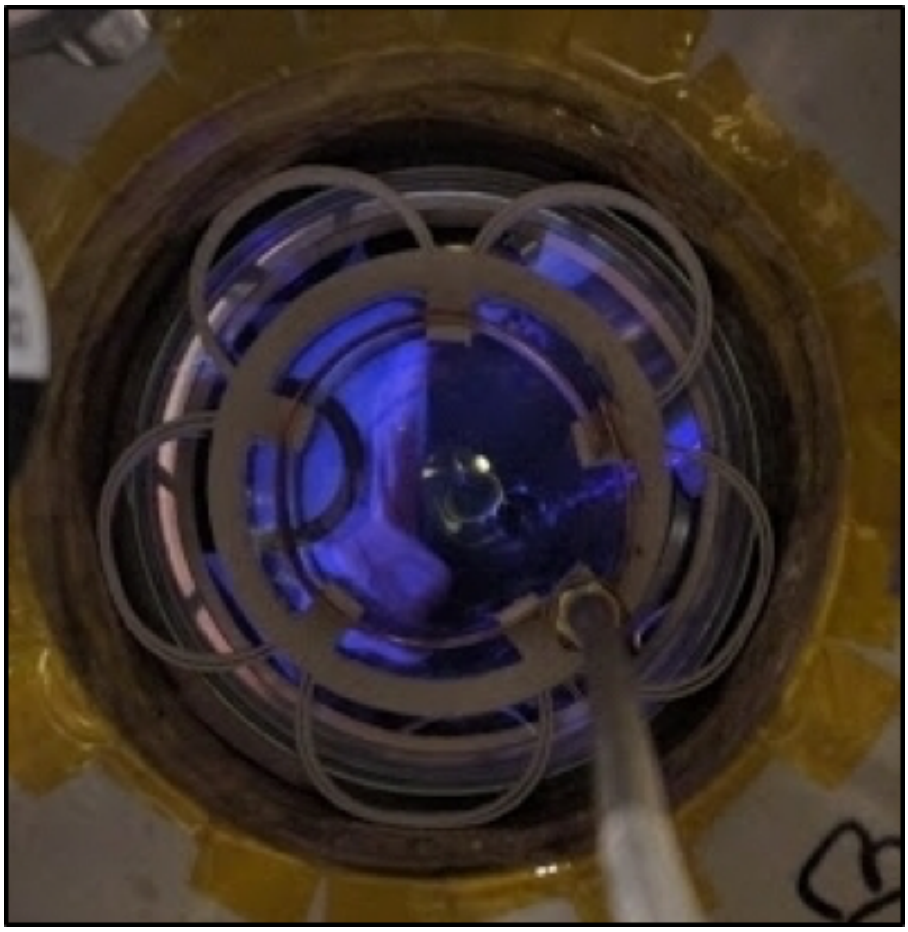

Figure 4.18: Ribbon antenna mounted in top bucket of the main chamber.

In order to get strong enough RF coupling to our atoms, we had to buy a 200 W RF amplifier (Model 5020R from Ophir). Even though we placed this amplifier in the core rather than in the main lab, the radio-frequency generated by our antenna causes RF to couple to all of the electronics, oscilloscopes, and computer displays in our lab. We had to spend a significant amount of time "RF proofing" the laboratory by putting ferrite beads, clamps, and chokes on our electronics. This had led to one of my favorite

lab sayings: "choke everything and choke often."*

4.10 1064 nm Laser System

The 1064 laser system (Figure 4.19) is used to create the optical dipole traps and the optical lattices in our experiment. We use a Nufern 50 W fiber amplifier to amplify a 50 mW seed from a NKT Photonics Koheras Boostik HPA laser.

The light from the Nufern is passed through two optical isolators to protect the amplifier from the lattice retro-reflection. In fact, we optimize the reflection of the lattice beams by maximizing the output power through a rejection port on the isolator on the return pathway.

We use two rotatable waveplates (model RSC-104E from Pacific Laser equipment) to control the total power diverted to ODT1 and ODT2. During optical evaporation, all of the 1064 nm laser power is diverted in equal parts to ODT1 and ODT2. We control the optical power on the atoms by sampling off roughly 1% of each ODT beam using BSF10C beam samplers from Thorlabs. The chipped off light is sent to a photodiode (PDA100A) and used to feedback on the RF power of the individual ODT AOMs using a PID circuit. The output power of each ODT arm as a function of the PID photodiode set-point voltage is shown in Figure 4.20. During the 4.5 seconds of optical evaporation, RWP1 and RWP2 are slowly rotated to divert all the extra optical power that is not needed at the end of optical evaporation in the crossed ODT to the lattice beams. We also monitor the power in each lattice beam by sampling 1% of the lattice light in each arm using a BSF10C beam sampler. However, we monitor the lattice light using fast photodiodes: Thorlabs, PDA20CS. We monitor the lattice light with fast photodiodes because the majority of our experiments require fast modulation of the optical lattice

*Also a good motto to have if you enjoy Brazilian jiu-jitsu like me.

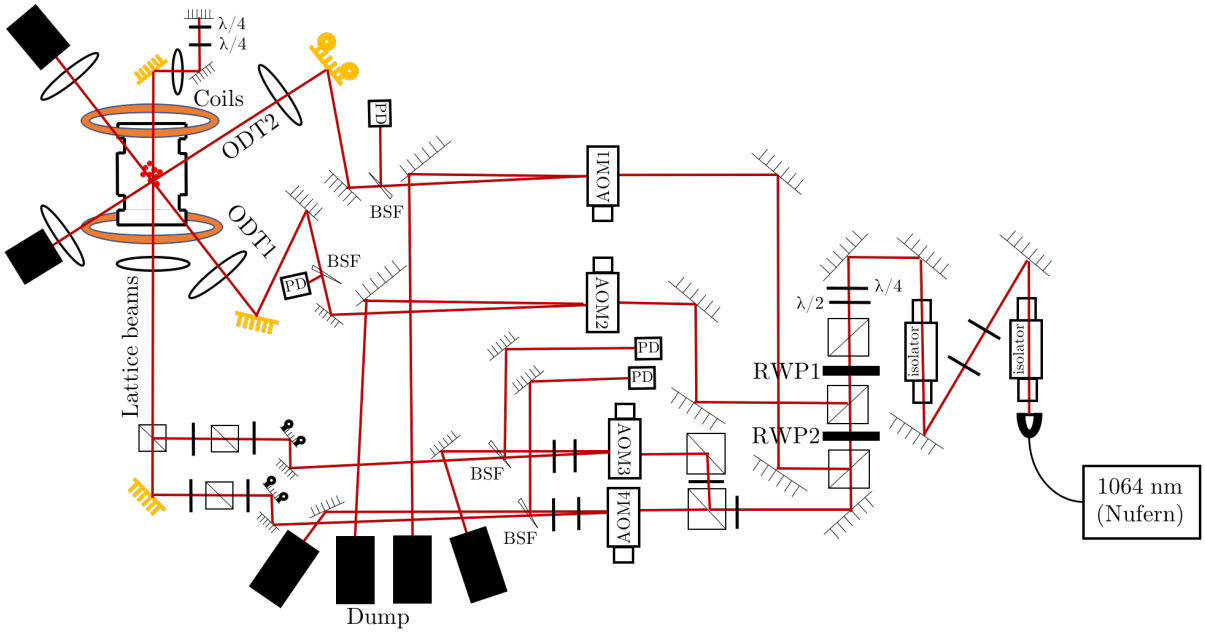

Figure 4.19: 1064 nm laser setup. The yellow mirrors in the diagram are dichroics that reflect 1064 nm and transmit 671 nm. We send 671 nm light through these dichroics if we want to image the 1064 nm beams on a camera or if we want to perform absorption imaging on that axis. The mirrors with circular knobs are position-controlled with piezoelectrics to allow for precision alignment of ODT2 and each of the lattice beams.

amplitude. There are two lattice beams that overlap each other in Figure 4.19. They are

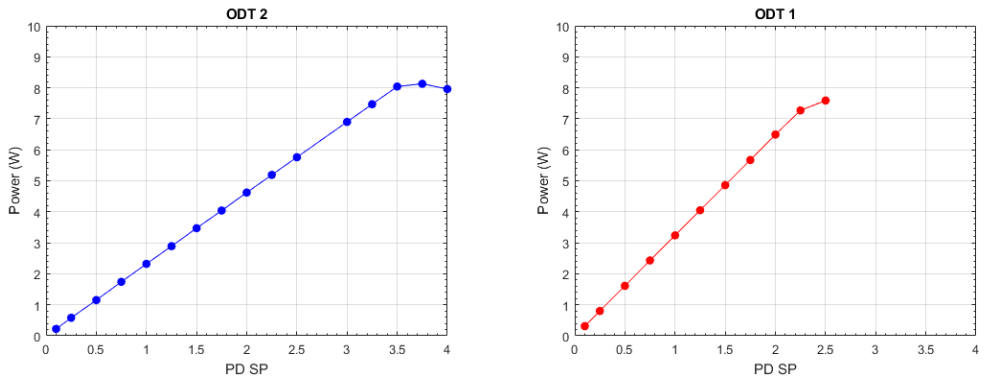

Figure 4.20: Power in ODT1 and ODT2 as a function of the PID set-point voltage.

both linearly polarized on the atoms, but orthogonal to each other. Additionally, the two quarter waveplates that appear prior to the retro-reflection mirror are angled such that

one of the lattice beams acquires a spatial phase shift of $\lambda/4$ (half the lattice spacing) relative to the other (see Appendix C for details). We use up to 7 W of 1064 nm light per lattice beam and an 88 μm beam waist. The two lattices are separated in frequency by 160 MHz. Because one of the lattices is spatially shifted from the other by $\lambda/4$, the two lattices will cancel each other when both beams have the same power, resulting in a featureless optical dipole trap. The radio-frequency signals in the lattice AOMs (AOM3 and AOM4) are produced by programming an AD9854 DDS board. This allows us to simultaneously modulate both lattice beams to construct a variety of modulated lattice potentials. Use of the AD9854 DDS board allows us to modulate the amplitude of the lattice at up to 2 MHz. Moreover, the double lattice modulation allows us to create a combined optical lattice that can change sign, where maxima (minima) become minima (maxima) during a drive cycle.

Chapter 5

Floquet Band Hybridization

All of our experiments begin with a BEC adiabatically loaded into the ground state of the combined optical lattice. We adiabatically and linearly ramp on the lattice light to a 5 to 20 E_R depth static lattice in 100 ms while the crossed optical dipole trap beams remain on to hold the BEC. The presence of the crossed optical dipole trap prevents atoms from Bloch oscillating in the optical lattice. We set the $t = 0$ point of the experiment as the moment that the crossed optical dipole trap is turned off.

A diagram of our typical lattice experiments is shown in Figure 5.1. We apply magnetic forces along the lattice direction by using four 4' by 8' rectangular wire loops with 75 turns/coil. These rectangular wire loops can effectively be considered bar magnets because the far rectangular side is too distant from the atoms to have an effect and the radial directions have no effect. We colloquially call these push coils the wing coils because they look like four large angel wings on the main chamber.

We use the push coils to both cancel the residual magnetic force along the lattice direction from the main electromagnets and to apply a controllable magnetic force along the lattice direction to induce Bloch oscillations. A plot of the induced force along the lattice direction as a function of the current in the four magnets is shown in Figure 5.2.

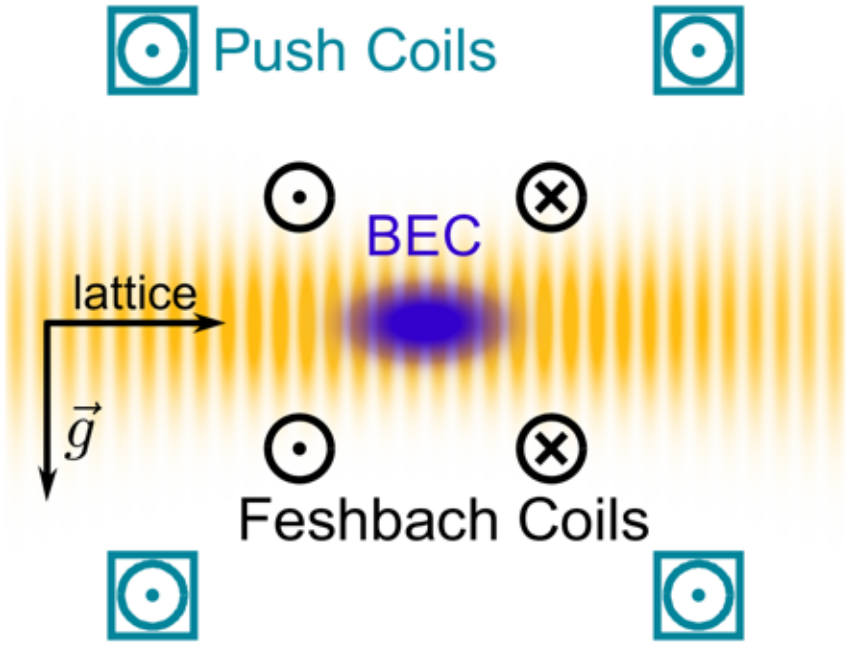

Figure 5.1: Schematic of the optical lattice. Figure is adapted from [20].

5.1 Amplitude Modulation Spectroscopy

We have two ways to calibrate the depth of each of the optical lattices. One way is with amplitude modulation spectroscopy and the other way is with Kapitza-Dirac (matter-wave) diffraction. We typically use the Feshbach resonance to set the s-wave interactions between atoms to zero prior to calibrating the lattice depth.

In amplitude modulation spectroscopy, we turn on one of the optical lattices and perform amplitude modulation at a variety of frequencies to look for band transitions. A plot of various band transitions as a function of the lattice depth is shown in Figure 5.3. We can control at which quasimomentum we induce the transition by letting the atoms controllably Bloch oscillate to a certain quasimomentum up the band.

Figure 5.4 shows what a typical amplitude modulation calibration run looks like. In

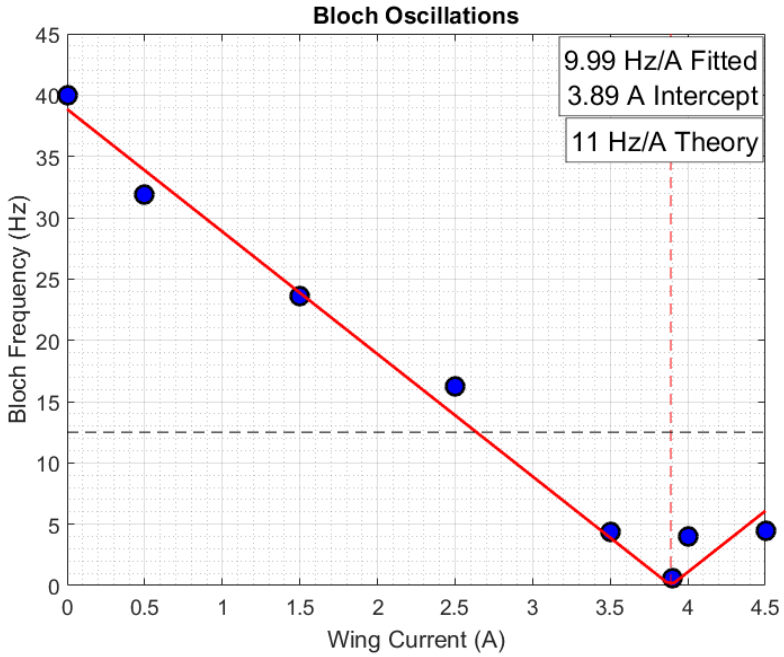

Figure 5.2: Bloch oscillation frequency (in a single 10 E_R lattice) along the lattice direction as a function of current in the push coils. You'll notice that there is a 40 Hz Bloch oscillation at zero amps. This is from the residual magnetic curvature from the main electromagnets.

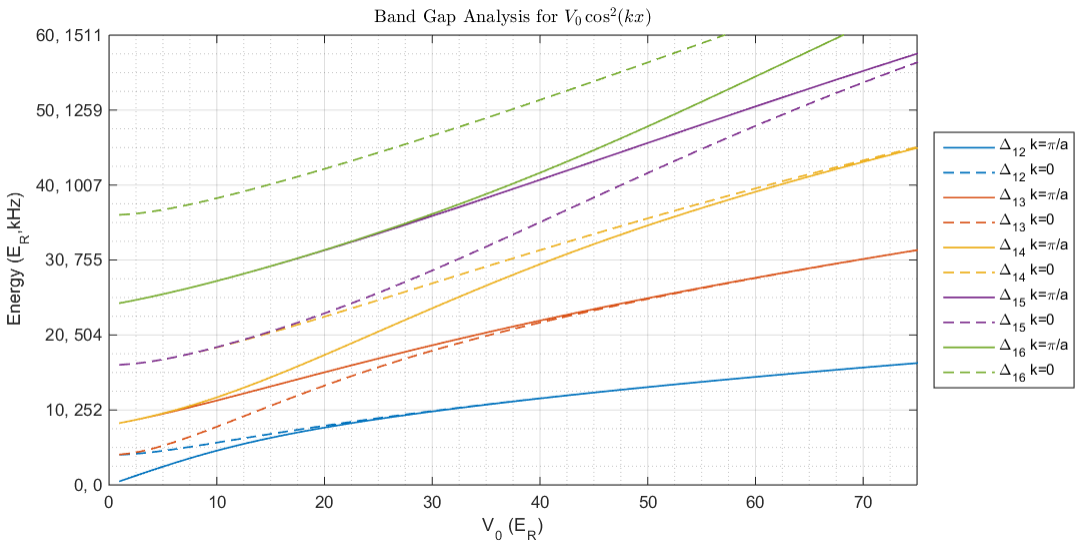

Figure 5.3: Various band transitions as a function of the lattice depth. Δ_{1n} indicates the transtion energy from the 1st (ground) band to the nth band. k indicates the quasimomentum value.

this experimental run, we load the atoms into the ground band of a 5 E_R lattice at zero quasimomentum and perform 10% modulation of the optical lattice depth in a frequency range from 124 to 167 kHz. You'll notice from Figure 5.3 that the transition from the 1st to 3rd band happens in a 5 E_R lattice at around 130 kHz. Because we perform amplitude modulation (as opposed to phase modulation) and because the quasimomentum of the atoms is zero, we do not see the 1st to 2nd transition (because this would be parity violating). We perform band-mapping after the amplitude modulation to extract the population of the atoms in the ground band. Band-mapping is a procedure where if the optical lattice is turned off adiabatically with respect to the band gaps, the atoms in different bands will be mapped onto the free particle momentum states. This procedure allows us to extract the population in each band from an absorption image [51]. Figure 5.5 shows fits to the atom number population in the ground band and the third band (called the 1st order or 1st excited band in the figure). The resonance occurs at about 136 kHz which tells us the lattice depth is indeed 5 E_R.

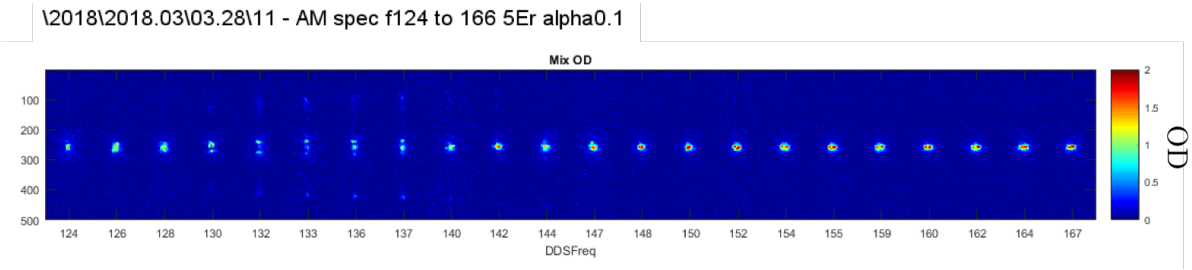

Figure 5.4: Absorption images from amplitude modulation spectroscopy on a 5 E_R lattice. DDSFreq is the modulation frequency in kHz (produced from the DDS).

5.2 Kapitza-Dirac Diffraction

A more robust way to calibrate a deep optical lattice is with Kapitza-Dirac diffraction. In this method, we pulse on the lattice as a square wave for 3 μs (see Figure 5.6) and

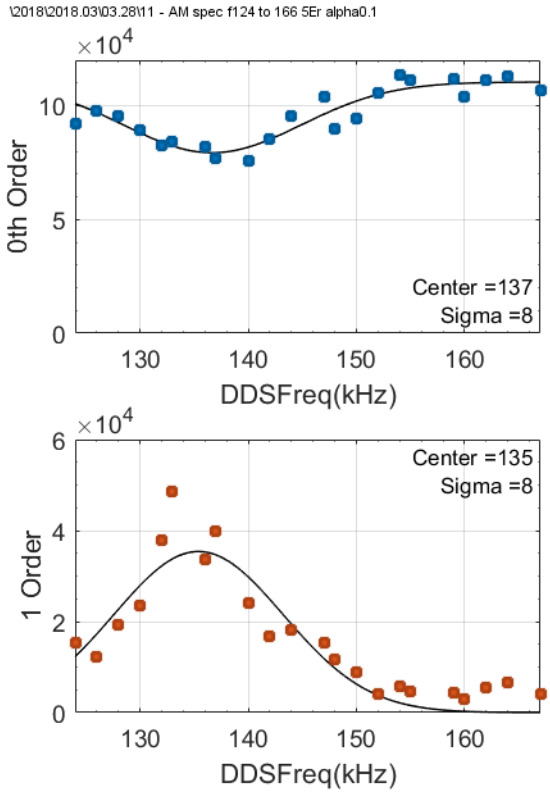

Figure 5.5: Fits of the atom number in the various observed peaks from amplitude modulation spectroscopy. Same data as Figure 5.4.

fit the atom number in the matter-wave diffracted peaks via comparison to numerical integration of the time-dependent Schrödinger equation [52]. We can do this separately for each lattice or for the combined lattice system. We colloquially call the horizontally polarized lattice KP1 and the vertically polarized lattice KP2.

The way we perform Kapitza-Dirac diffraction calibration is as follows. We pulse on each lattice separately for 3 μs at a variety of different lattice depths. We vary the lattice depth by changing the voltage of the voltage variable attenuator that controls the RF power sent to each AOM that produces the lattice beam (AOM3 or AOM4 from Figure 4.19). For each lattice depth, we measure the optical power of the lattice beam using a photodiode pick-off (example measurement is Figure 5.6). We then produce plots of the diffracted atom number in each momentum peak as a function of the photodiode voltage

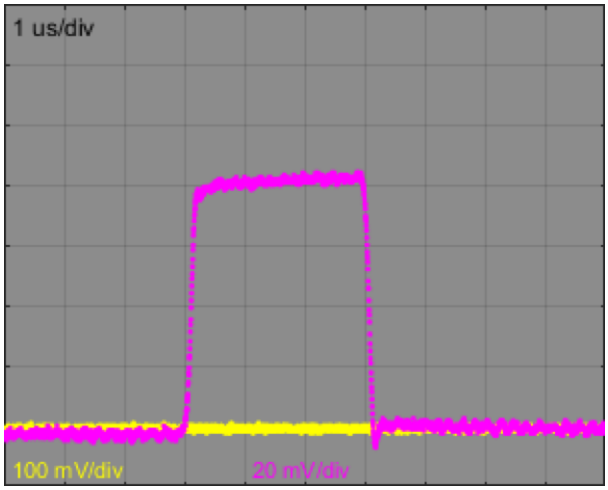

Figure 5.6: Optical lattice pulse shape as measured by a photodiode for Kapitza-Dirac diffraction measurements (horizontal axis is time in μs and the vertical axis is the voltage on the photodiode). Yellow is KP1 and pink is KP2. Only KP2 is pulsed here.

(shown for each lattice in Figures 5.7 and 5.8). We then extract the lattice depth per voltage as measured on the photodiode dedicated to each lattice via comparison of the observed atom number fraction in each momentum peak to numerical integration of the Schrödinger equation. Once we know the lattice recoils per volt, we can then perform a linear ramp of the VVA voltage in 100 ms to extract the functional form of the lattice depth as a function of the VVA voltage for each lattice (as shown in Figure 5.9). Once we know the appropriate VVA value to set a certain lattice depth, we then use the DDS to programmatically modulate the optical lattice depths.

5.3 Position-Space Bloch Oscillations

The first experiment we performed with our optical lattice was to observe position-space Bloch oscillations for the first time.

Normally, when you apply a constant force on something, the object just moves along with constant acceleration. However, in a mind-boggling turn of events, this is not the

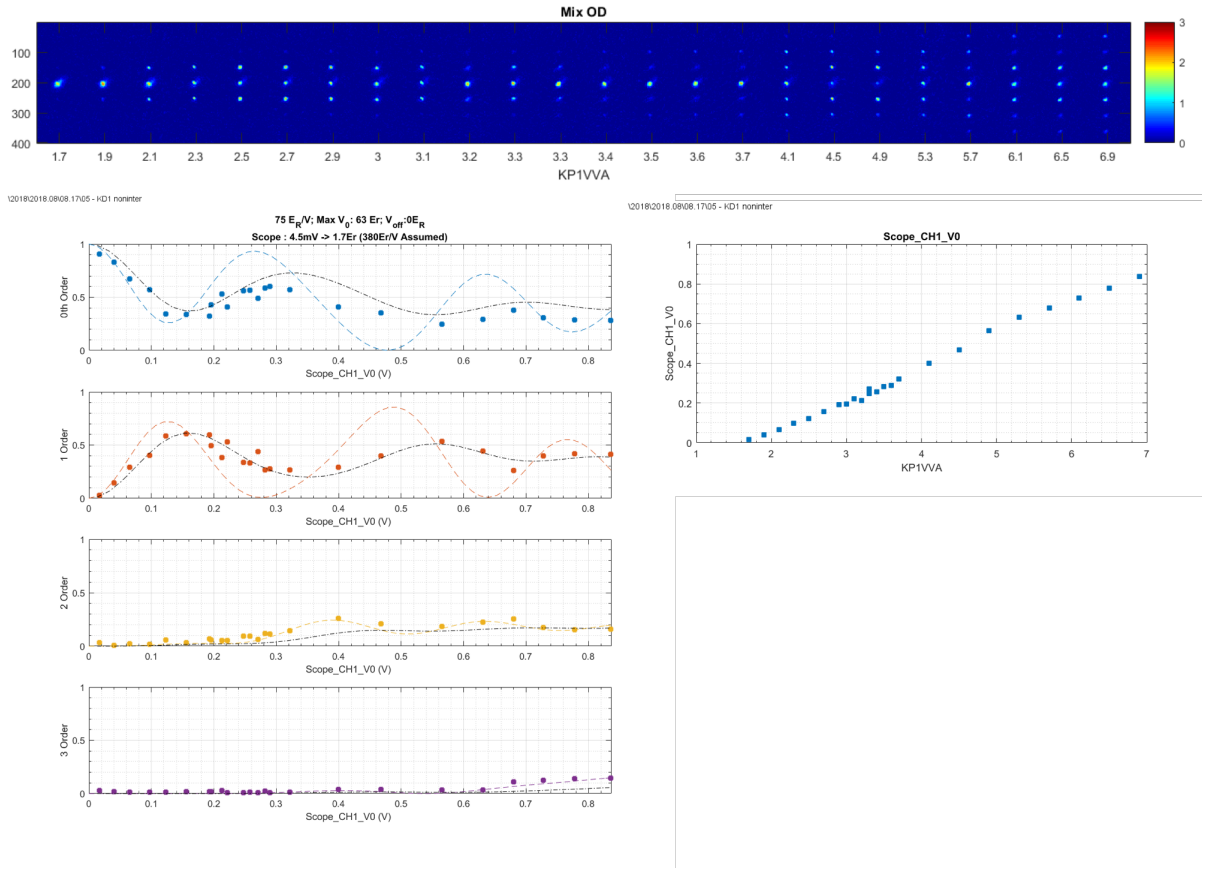

Figure 5.7: Plots of the Kapitza-Dirac diffraction measurement for KP1.

case for quantum particles in a periodic potential. If you apply a constant force on particles in a periodic potential, you'll actually find that they undergo periodic motion! This is a Bloch oscillation. Even though I have seen it in our absorption images thousands of times, I personally still find it incredibly spooky. Typically, Bloch oscillations are hard to see in solid state systems due to phonons and electron-electron scattering. With cold atoms, it is relatively straightforward. In our experiment, we first prepare a lithium Bose-Einstein condensate and load it into the ground band of an optical lattice.

Because our atom is magnetic, we apply a magnetic field gradient on the atoms with the push coils to create a small force along the lattice direction. This causes the atoms to oscillate in the band-structure. In Figure 5.10, I have plotted the band structure of

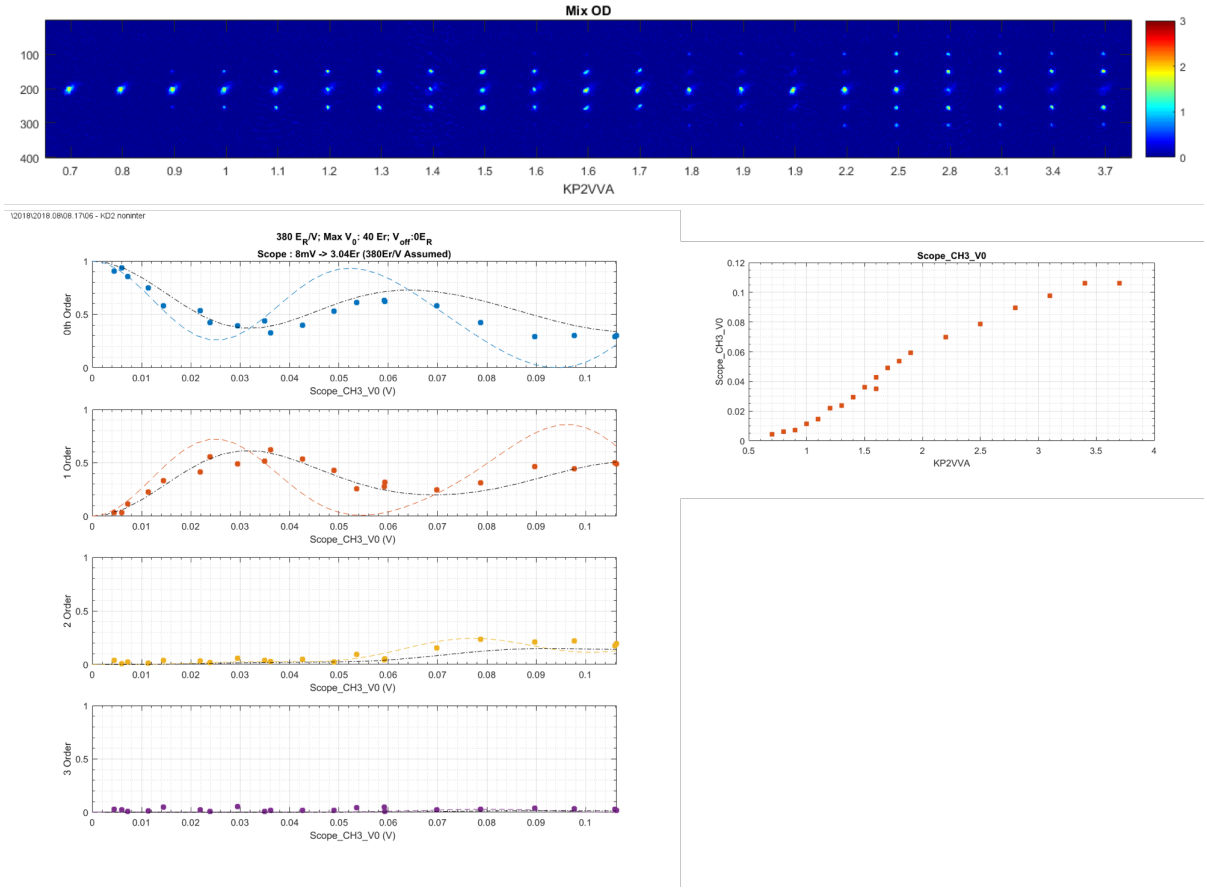

Figure 5.8: Plots of the Kapitza-Dirac diffraction measurement for KP2.

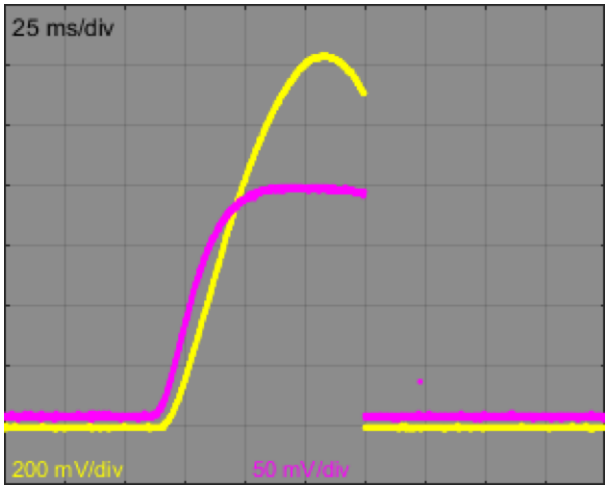

Figure 5.9: Optical lattice depth vs VVA. Here, the VVA voltage for each lattice is ramped linearly in 100 ms starting from the 50 ms point.

an optical lattice. We typically denote the bands of the lattice with letters s, p, d, f, g, and so on.

In cold atom experiments, Bloch oscillations are normally observed in momentum space because the position-space oscillations are typically too small to image or extract. The amplitude of the spatial oscillation is given by the Wannier-Stark localization length [53]:

$$l_{WS} = 2J/F. \tag{5.1}$$

Here, J is the tunneling rate between lattice sites and F is the force applied to the atoms. In our experiments, J is very large (because lithium is really light!) and F can be made to be rather small (we used magnetic forces instead of gravity!). Additionally, we remove the interactions between atoms with the Feshbach resonance. With these ingredients, we were able to observe large amplitude position space Bloch oscillations for the first time (Figure 5.11).

A great application of position space Bloch oscillations is that they directly map out the band structure of the optical lattice. To see this, consider first the functional form of the position as a function of time using the integral of the group velocity:

$$x(t) = \int v(t)dt = \int \frac{1}{\hbar}\frac{\partial E}{\partial k}dt = \int \frac{1}{\hbar}dE\frac{\partial t}{\partial k}. \tag{5.2}$$

During a Bloch oscillation, the quasimomentum k evolves linearly with the force F [53]:

$$k = \frac{F}{\hbar}t, \tag{5.3}$$

where $F = hf_B/d$ and d is the lattice spacing of 532 nm. Combining this with equation

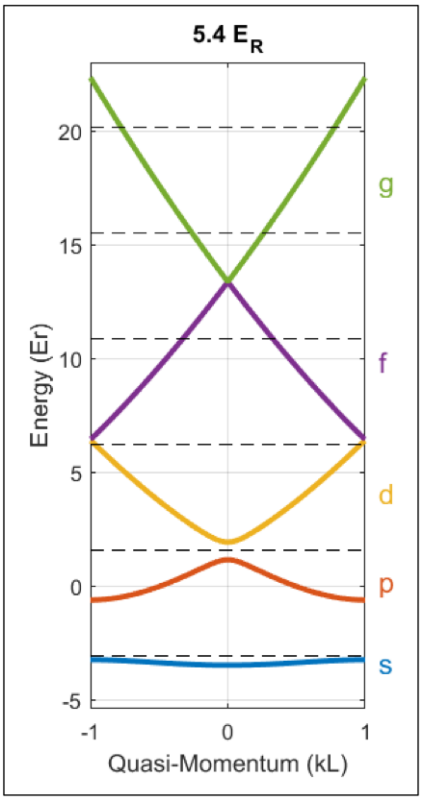

Figure 5.10: Band structure (energy as a function of quasimomentum) of a 5.4 E_R lattice.

5.2, we have:

$$x(t) = \int \frac{1}{\hbar} dE \frac{\hbar}{F} \tag{5.4}$$

$$\Delta x = \frac{\Delta E}{F} \tag{5.5}$$

This tells us:

$$E = Fx, \qquad k = \frac{F}{\hbar} t. \tag{5.6}$$

Therefore, there is a one-to-one mapping from position to energy and a one-to-one mapping from quasimomentum to time. In other words, if we experimentally measure the position as a function of time $x(t)$, then we directly measure the energy as a function

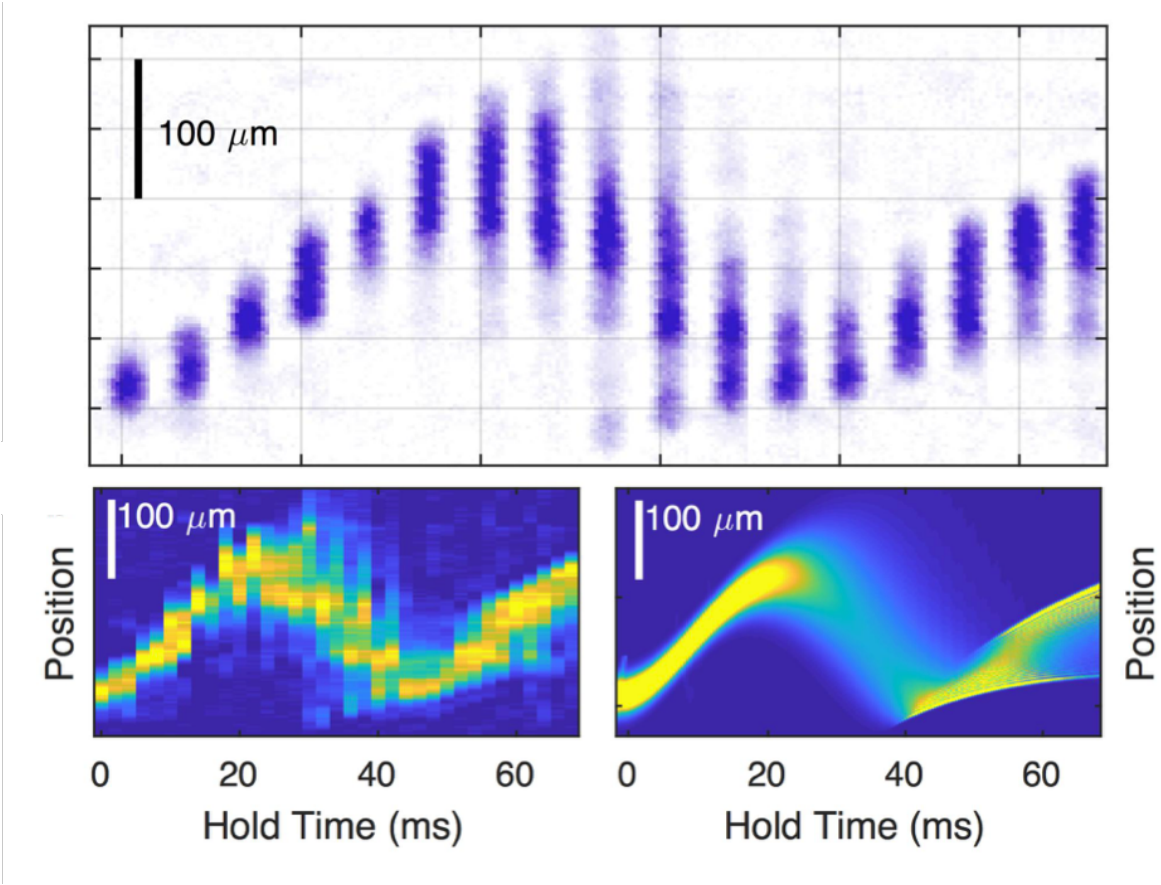

Figure 5.11: Large amplitude position space Bloch oscillations. This top plot is the raw experimental absorption images, time ordered from left to right. Each cloud is a snapshot of the atoms at a constant time interval into the future. Bottom right plot is a numerical simulation of the oscillation with the same experimental parameters. Figure is adapted from [19].

of quasimomentum $E(k)$. Examples of these measurements performed at various lattice depths are shown in Figure 5.12. In this figure, we directly overlay the measured positions of the atoms on top of the band structure with no fits and see that they agree well.

These arguments are not just limited to the ground band. They can be used to map out the band structure of the higher bands as well. In Figure 5.13, I have included position measurements of the atoms in the ground band (s-band) and also in the p-band.

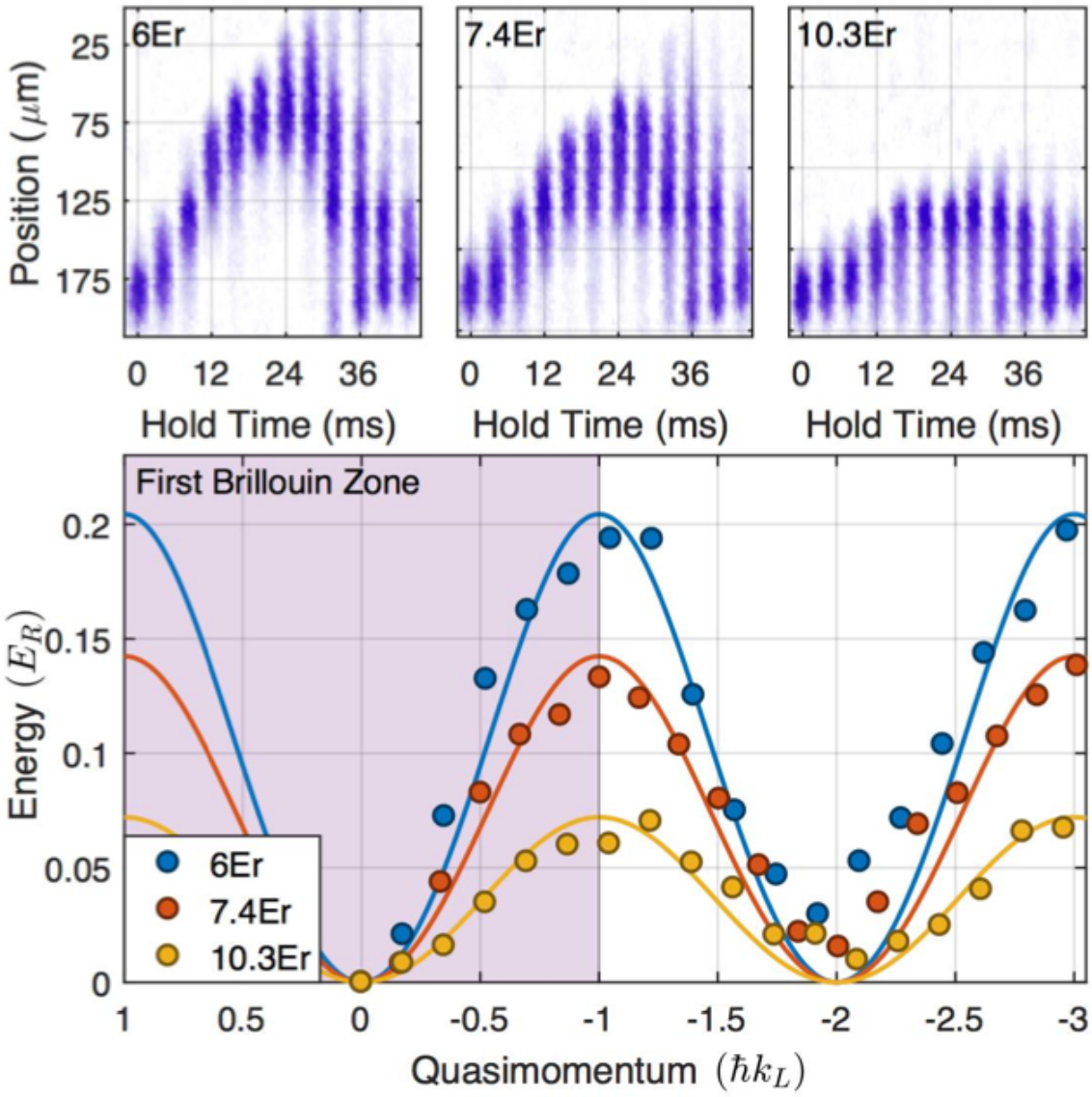

Figure 5.12: Position space Bloch oscillations map out the band structure of the optical lattice. The top row shows absorption images of the atoms Bloch oscillating in position space for various lattice depths. The bottom row shows the position of the atoms overlaid on top of the band structure using equation 5.6. Figure is adapted from [19].

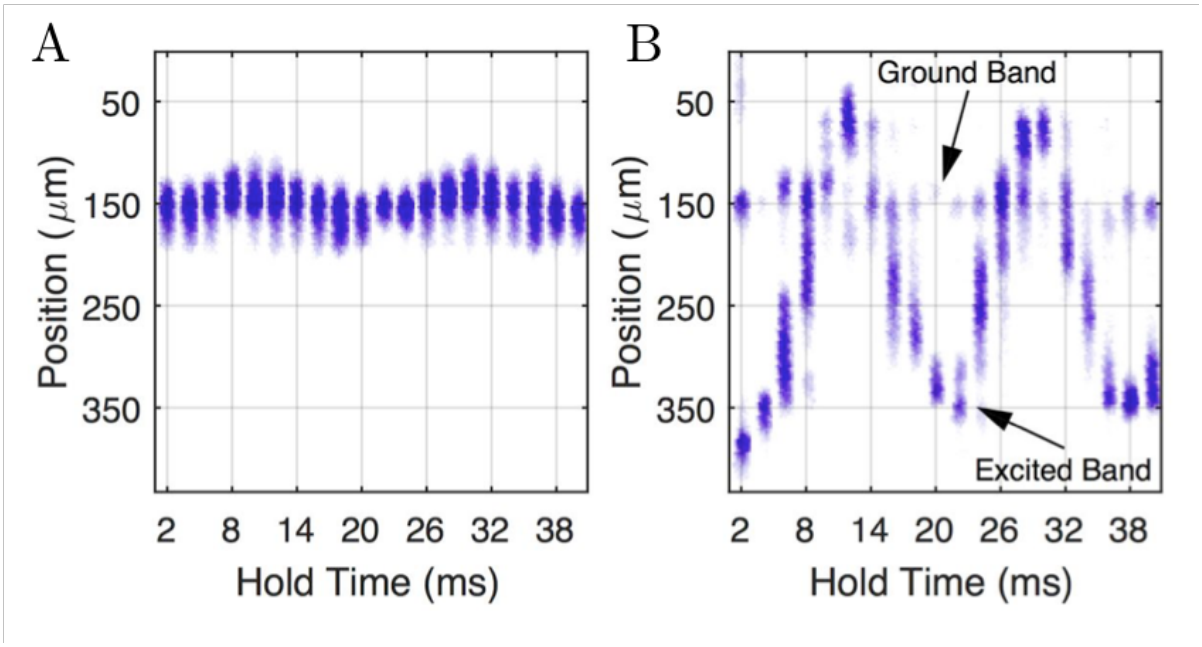

Figure 5.13: Absorption images of the atoms Bloch oscillating in position space in the s-band and in the p-band. Position space Bloch oscillations can be used to map out the band structure in higher bands as well. Figure is adapted from [19].

5.4 Transport in Floquet-Hybridized Bloch Bands

In this section, we'll perform the same experiments as in previous section but add amplitude modulation (between 0 to 100% of the amplitude of the lattice) at a fixed frequency. If the amplitude modulation frequency is resonant with a band transition at a certain quasimomentum, then the two bands effectively hybridize to create a hybrid band. Just like how the spatial potential being periodic in a crystal causes the momentum to be the same modulo $2\pi/a$ and is called quasimomentum, the presence of the drive photons cause energy to be the same modulo $\hbar\omega_{drive}$ and is called quasienergy. The space of hybridized bands is called the quasienergy or Floquet spectrum and an example of this is shown in Figure 5.14. Great resources to learn how to quickly calculate quasienergy band structures for driven optical lattices are [42, 9].

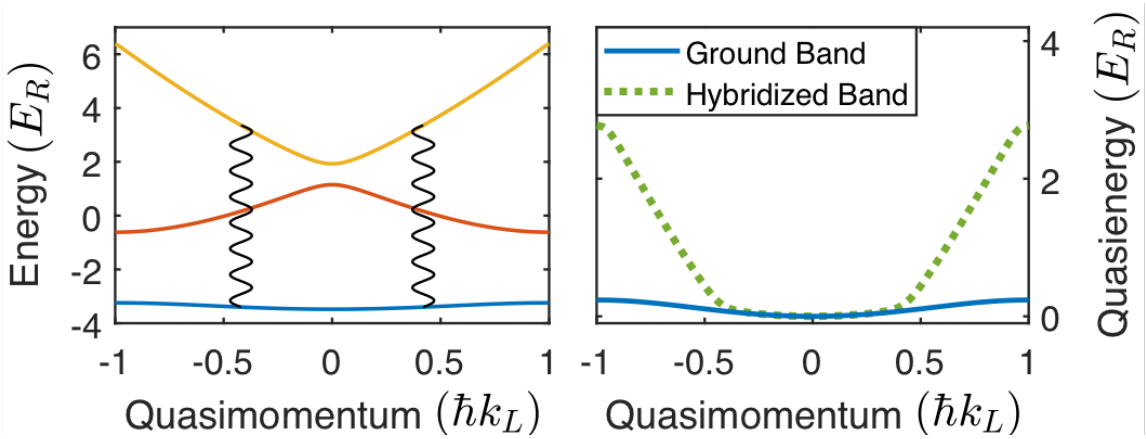

Figure 5.14: Example of the effect of small amplitude modulation. If the modulation frequency bridges the gap between two bands, then the two bands effectively hybridize. Bloch oscillations now occur along this hybridized band.

Let's suppose we couple the s to d bands in a 5.4 E_R lattice by applying a 20% amplitude modulation at a frequency of 170 kHz. We then let the atoms Bloch-oscillate in this band with a Bloch oscillation frequency of 48 Hz, starting initially in the zero quasimomentum state of the ground band. What we observe is shown in Figure 5.15.

The atoms initially begin Bloch oscillations in the s-band portion of the hybrid band structure shown in Figure 5.14. Once they enter the d-band portion, the group velocity suddenly becomes large and the atoms shuttle across the magnetic potential that initially provided an effective constant force for Bloch oscillations. However, now that the atoms are moving long distances, the force from the magnetic potential is no longer constant. Instead, the force decreases, becomes zero, and then switches sign. This means the atoms begin to Bloch oscillate back down the hybrid band, having never reached the edge of the Brillouin zone. Because the magnetic trap is shallow (the trap frequency is $\omega_{trap} = 2\pi \times 15.5$ Hz), the atoms travel a long way (roughly 2000 lattice sites) in the d-band portion of the excited band. This is long distance transport. The nature of the transport in the hybrid band is summarized in Figure 5.16. The atoms continue to coherently Bloch oscillate when they return to their initial position in the magnetic trap, as shown in Figure 5.15C. This opens up a wide array of opportunities to use the transport mechanism as a way to interfere transported atoms with the atoms remaining in the s-band to perform atom interferometric experiments. The relative population of the transported atoms and the remaining atoms can be controlled with the intensity of amplitude modulation.

Additionally, this coupling of hybrid bands is not just limited to the s and d bands. One can in principle couple together any pair of bands at a certain quasimomentum to create a variety of Frankenbands. In Figure 5.17, we use the modulation to create hybrid bands of the s and g bands and show absorption images of the resulting Bloch oscillation. As an aside, if we stitch the s-band together with a higher even numbered band near the edge of the Brillouin zone, we can emulate the physics of the relativistic harmonic oscillator [55].

Just like how the position-space Bloch oscillation could be used to map out the band structure of the static lattice, the position-space Bloch oscillation can also be used to

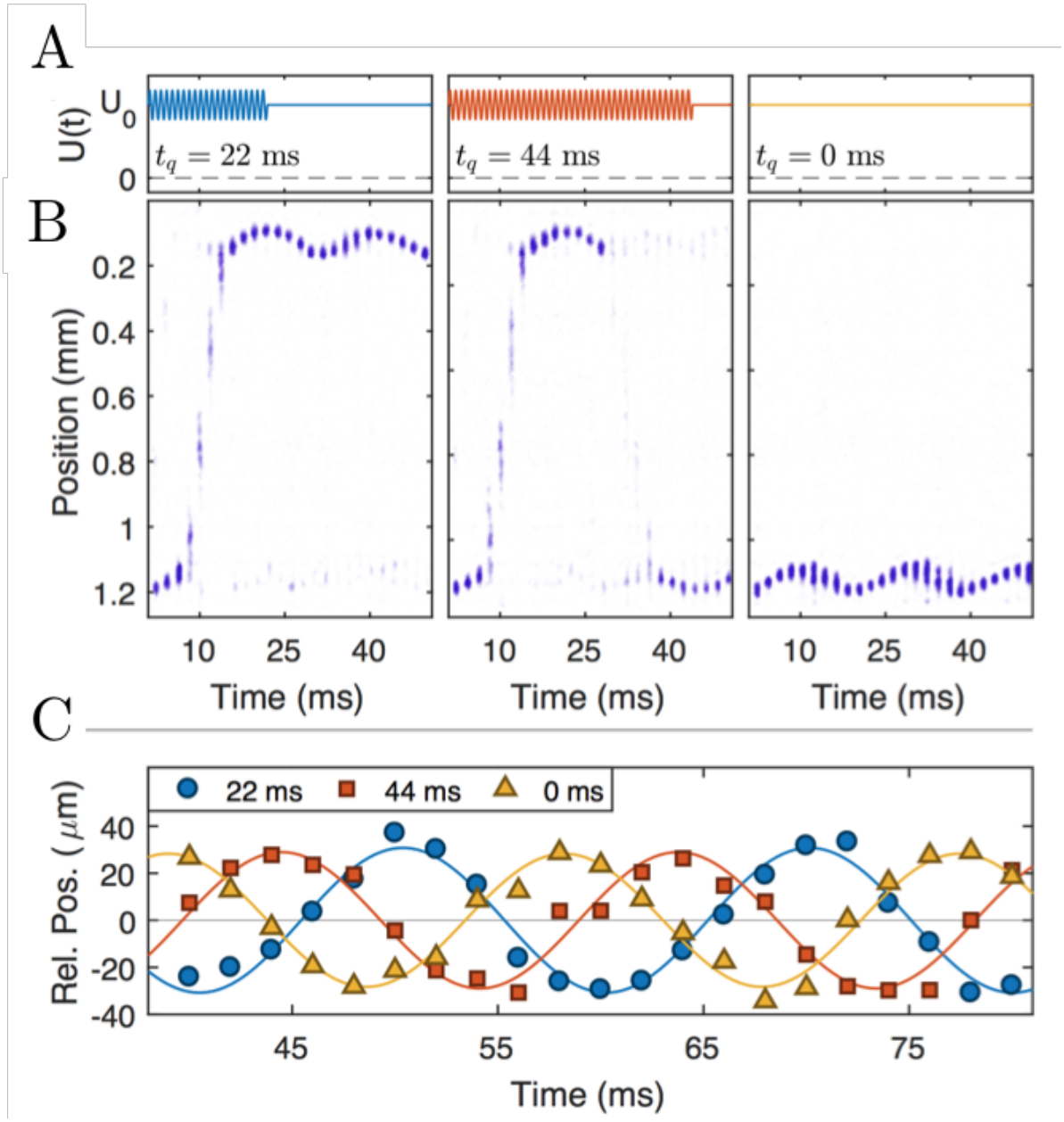

Figure 5.15: Long distance coherent transport. A) shows the modulation of the optical lattice for three different scenarios. B) Absorption images of the atoms as a function of time for each modulation scenario shown in (A). C) The Bloch oscillations in the s-band continue to evolve coherently even after the return of the atoms. Figure is adapted from [20].

map out the quasienergy structure of the modulated lattice. In Figure 5.18, we couple together the s and p bands using 25% amplitude modulation at a frequency of 56 kHz

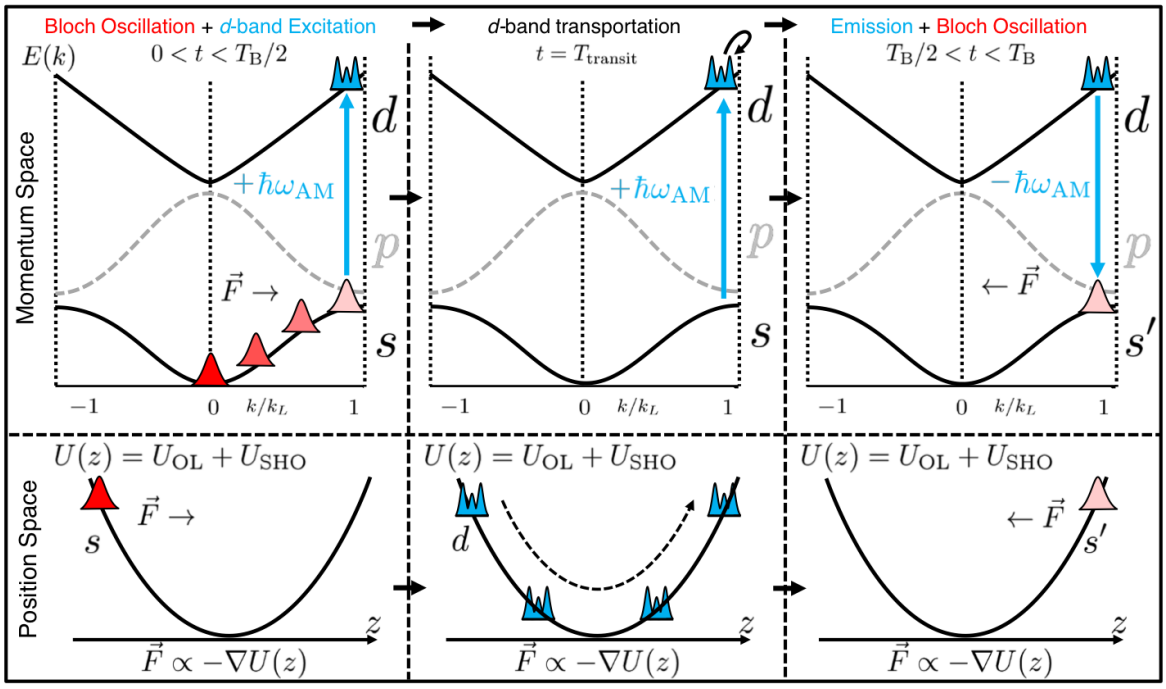

Figure 5.16: Diagram of the long-distance transport. The atoms begin Bloch oscillating in the s-band. The atoms are excited to the d-band once they Bloch oscillate in momentum-space to a quasimomentum value that makes them resonant with the drive photon. The atoms move long distances in the d-band such that the force no longer remains constant. The force decreases to zero and then switches sign. In the d-band, this means the atoms perform a loop in the band-structure and are then de-excited to the s-band at the opposite side of the magnetic potential. Figure is adapted from [54].

in a 3.6 E_R deep lattice. We use this shallow lattice to experimentally distinguish the frequency of the $k = 0$ transition from the $k = \pi/a$ transition (see Figure 5.3) and prevent two-photon coupling to the d band. What we find in the s-p hybrid is that the atoms form a (relatively) flat band. Additionally, the position-space motion of the atoms maps out the quasienergy spectrum of the hybrid band as demonstrated explicitly in Figure 5.18D. There are no fitting parameters.

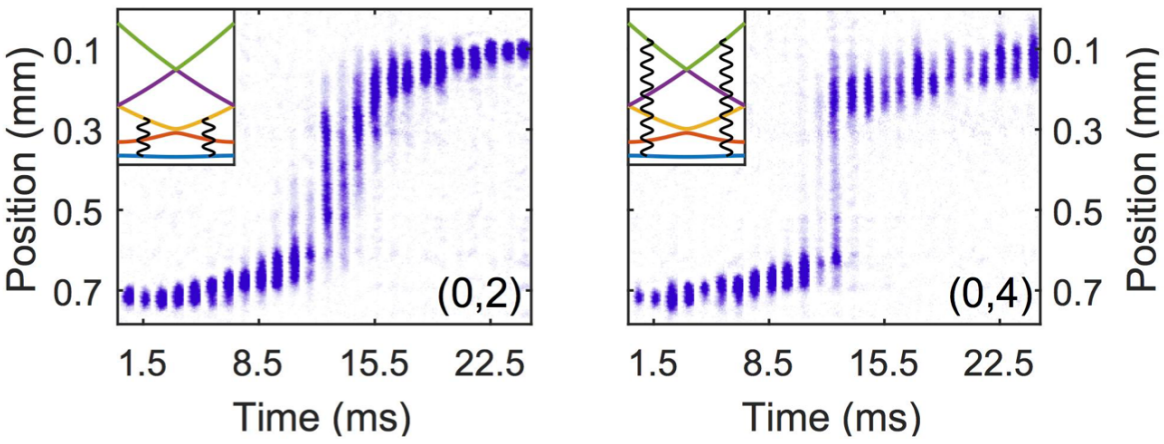

Figure 5.17: Absorption images of position space Bloch oscillations demonstrating that a variety of hybrid bands can be constructed using amplitude modulation at specific quasimomenta. The left plot demonstrates s-d hybridization. The right plot demonstrates s-g hybridization. Figure is adapted from [20].

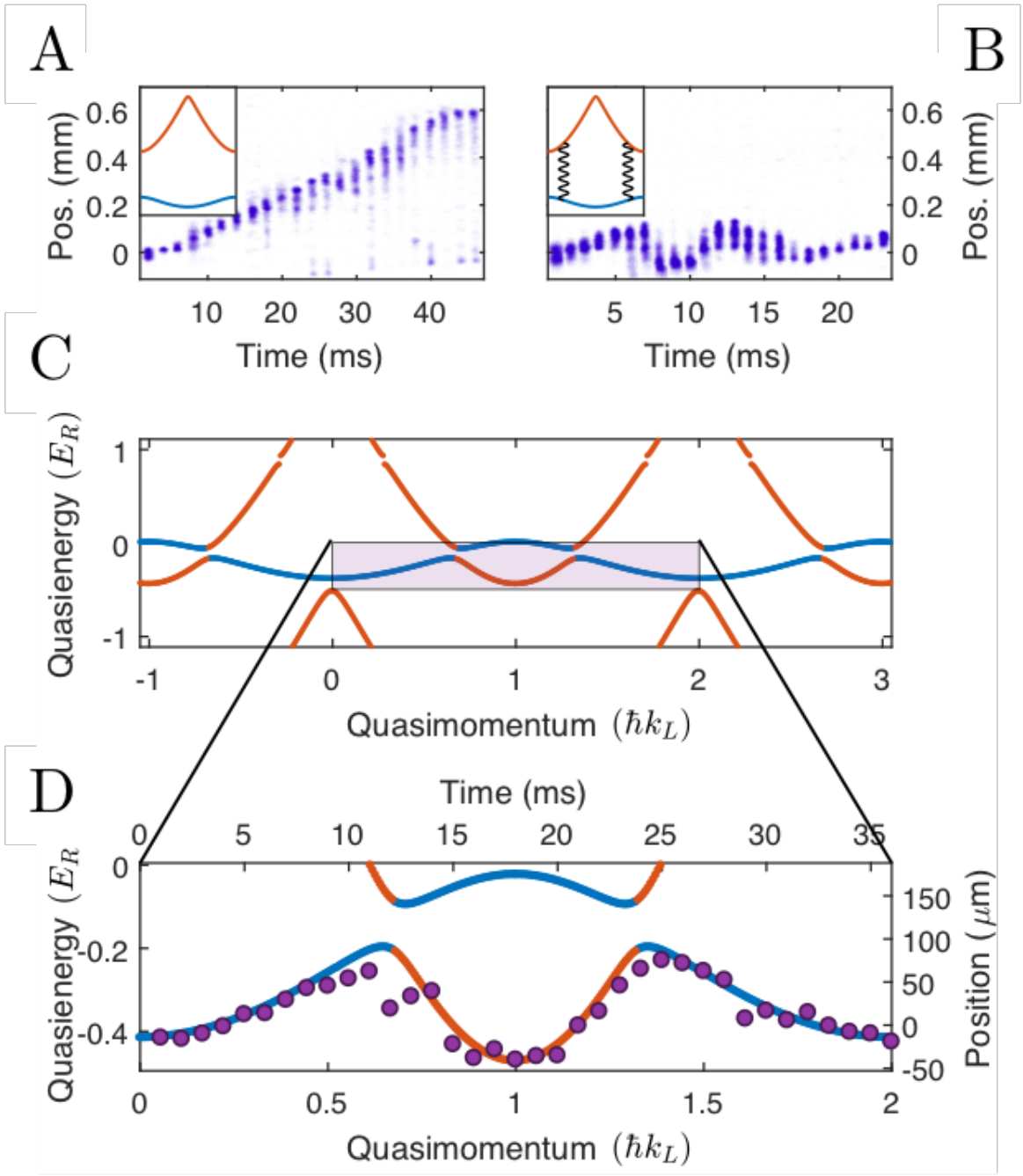

Figure 5.18: Experiments in a 3.6 E_R lattice. A) Bloch oscillations in the lattice with no modulation. B) Bloch oscillations in the lattice with 25% amplitude modulation at a frequency of 56 kHz to couple together the s and p bands. C) Theoretical quasienergy structure D) Data from (B) overlaid on top of the quasienergy structure from (C). Figure is adapted from [20].

Chapter 6

Periodic Gibbs Ensembles and Floquet Prethermalization

As discussed in Chapter 2, Floquet engineering has emerged as a powerful technique for building novel quantum states with drive-dependent properties [56, 57, 39, 42, 58, 59, 60, 61, 62, 63, 20]. While interacting driven multi-band systems are generally expected to heat to infinite temperature at infinite time, this does not preclude the realization of nontrivial states at intermediate (and in some cases exponentially long) time scales [26, 64, 65, 66, 67]. Thus, proper engineering of novel Floquet states requires both understanding and manipulating these intermediate prethermal states. For undriven systems, such prethermalization plateaux [68, 69] admit a statistical description in terms of generalized Gibbs ensembles [70, 71, 31] and have been observed in experiments [33, 72, 73]. Driven systems, by analogy, are theorized to exhibit *Floquet prethermalization* plateaux and quasi-steady states describable by a *periodic* Gibbs ensemble (PGE) [23, 40, 44, 64, 74, 75]. These PGEs allow computation of physical observables in non-equilibrium periodically driven systems.

In this chapter I will discuss experiments that generalize the concepts of equilibrium

statistical mechanics to periodically-driven systems that are far from equilibrium. These experiments explore a new regime of strongly-driven quantum systems, probing the evolution of tunably-interacting ^{7}Li atoms in an optical lattice amplitude-modulated at up to a thousand percent. I will discuss how we use a double quench protocol to directly quantify the localization of the initial state in the basis of the Floquet eigenstates of the one-cycle evolution operator. Our experiments map out a Floquet delocalization crossover in the space of drive parameters, and measure characteristics of the prethermal state which are in quantitative agreement with theoretical calculations based on a periodic Gibbs ensemble. Additionally, by tracking the time evolution of the driven system, we observe the approach to the prethermal plateau as well as the long-time departure from it, either by the formation of a second prethermal plateau or, for stronger interactions, by complete delocalization.

Previous experiments have examined the role of driving on many-body localized systems [43] and on driving near the lattice band gap [76, 77, 78, 79]. In our experiments, we study multi-band dynamics without disorder in the strongly-modulated regime, choosing modulation frequencies extending from 0.1 to 10 times the lattice band gap. This frequency range represents a particular challenge for theory due to the breakdown of the Floquet-Magnus expansion.

6.1 Experimental overview

In this experiment, we use the same combined lattice as discussed in the previous chapter but perform strong amplitude modulation of the lattice such that the amplitude is modulated at up to 1000% of the initial lattice depth. Additionally, we use the push coils to make sure that there are no forces (i.e. no Bloch oscillations) along the direction of the lattice. We use the Feshbach coils to generate three regimes of interactions: 1)

non-interacting (0 a_0), 2) moderately interacting (40 a_0), and 3) strongly interacting (600 a_0). The goal of using these interaction regions is to make the atomic system effectively resemble an integrable, nearly-integrable, and non-integrable system, respectively.

The lithium condensate is initially loaded into the ground band of the 1D optical lattice. The Hamiltonian is given by:

$$H(t) = -\frac{\hbar^2}{2m}\partial_x^2 + V_0[1 + \alpha f(t)]\sin^2(k_L x) \tag{6.1}$$

where $V_0 = 10\ E_R$ is initial static lattice depth and

$$E_R = \frac{\hbar^2 k_L^2}{2m} \tag{6.2}$$

is the recoil energy of the optical lattice. The modulation parameter is given by α which varies from zero to 10. In the experiment, the atoms are immediately quenched into the modulation function, $f(t)$, at $t = 0$ such that:

$$f(t) = \begin{cases} 0 & t < 0 \\ \sin(\omega t) & 0 \leq t \leq t_D \end{cases}$$

where t_D is the modulation time. The drive frequency can be expressed dimensionlessly as $\Omega = \omega/\omega_0$, where $\omega_0 = 2\sqrt{V_0 E_R/\hbar} = 159$ kHz is the frequency of harmonic motion in a single lattice site and which also approximates the lowest band gap of the static lattice. The modulation frequency Ω is chosen to be between 0 and 10. In this range, the frequency is high enough that multiple bands need to be considered but is not high enough that a Floquet-Magnus expansion can be used on the Hamiltonian [64]. As mentioned, the atoms are initially prepared in the ground band of a static optical lattice of depth $V_0 = 10\ E_R$ at zero quasimomentum. The system is quenched into the Floquet

Hamiltonian by applying lattice modulation at some Ω and α. After an amount of time t_D, the system is then quenched back into a static 10 E_R lattice to perform read-out of the many-body system in the eigenstates of the static optical lattice. We call this procedure our "double-quench" protocol. In the non-interacting case, the dynamics can be integrated straightforwardly using equation (10) in [80].

To guarantee the lattice modulation performs properly, we trigger the oscilloscopes that monitor the photodiodes on each lattice arm (see Figure 4.19 for the placement of the photodiodes). For each data run, we record the time trace of the power in each lattice in time (as shown in Figure 6.2). This lets us confirm that the lattice depths in each arm were correct and that the modulation proceeds at the appropriate α and appropriate Ω.

We program the DDS to perform the modulation of each lattice beam. As an example, we can explicitly make the potential the atoms experience from KP1 vary as:

$$V_1(x,t) = -A\left(1+\alpha\cos^2\left(\frac{\omega t}{2}\right)\right)\cos^2\left(kx+\frac{\pi}{2}\right) \tag{6.3}$$

and the potential from KP2 vary as:

$$V_2(x,t) = -A\alpha\cos^2\left(\frac{\omega t}{2}+\frac{\pi}{2}\right)\cos^2(kx). \tag{6.4}$$

The combined potential is then:

$$V_{tot}(x,t) = V_1(x,t) + V_2(x,t), \tag{6.5}$$

$$V_{tot}(x,t) = -\frac{A}{2}(1+\alpha) - \cos(2kx)\left[\frac{A}{2}+\frac{\alpha A}{2}\cos(\omega t)\right] \tag{6.6}$$

which results in the same Hamiltonian as Equation 6.1. An important note is that the combined optical lattice can be zero, but the overall confining ODT still exists. The

radial optical dipole trapping frequency in the combined lattice is then a function of α and is equal to:

$$\omega_r = 2\pi f_r = \sqrt{\frac{2}{m}\left(\frac{A(\alpha+2)}{\omega_0^2}\right)E_R}. \tag{6.7}$$

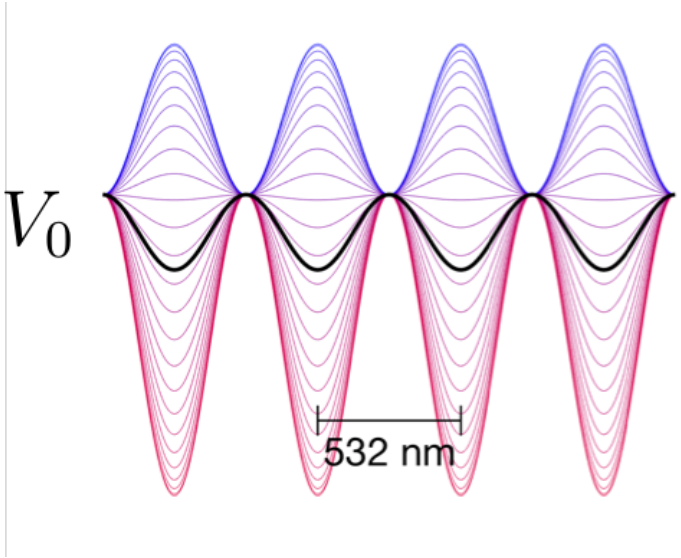

Figure 6.1: Schematic of strong modulation. The initial black lattice inverts in sign during the modulation.

As mentioned above, we first quench into the modulation, then quench out of the modulation, and then perform band-mapping on the optical lattice to read out the occupation number in the various bands of the lattice. An example absorption image for band-mapping is shown in Figure 6.3. We denote the occupation numbers in each band by f_0 for the ground band, by f_1 for the first band, and so on.

Measuring the ground band occupation is a direct quantitative measurement of the localization of the system in the basis of Floquet states. To see this, we will employ the notation for Floquet states and the periodic Gibbs ensemble as outlined in Section 2.4. To quantify the degree of localization (non-ergodicity), we initially prepare the system in the undriven ground-state $|\psi_0\rangle$, so that $c_n = \langle n(0)|\psi_0\rangle$, and consider the expectation

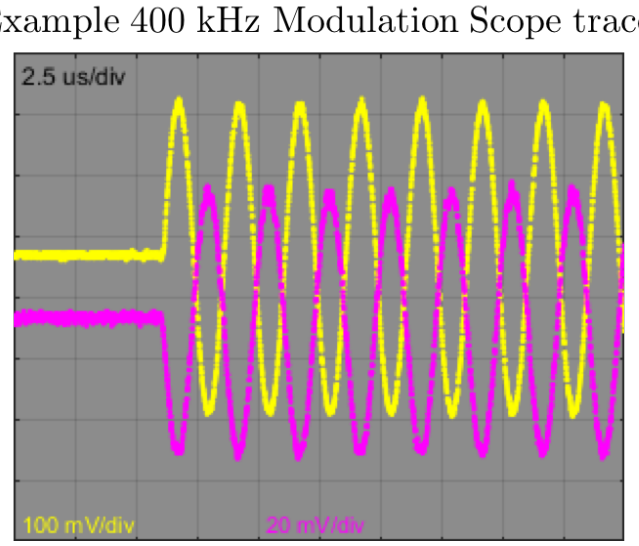

Figure 6.2: Example of lattice modulation for a modulation frequency of 400 kHz. The yellow trace is KP1, the pink trace is KP2. The initial 10 E_R static lattice is formed from the interference of the two lattices as seen in the flat region of this oscilloscope trace.

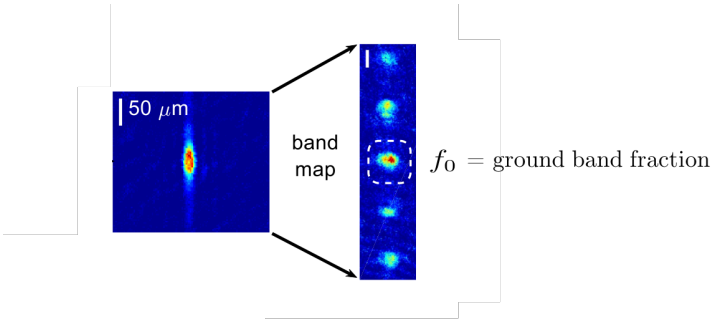

Figure 6.3: How to extract band occupation. Band-mapping lets us directly measure the population of the atoms in the ground band or the excited bands.

value of the projector $\hat{O} = |\psi_0\rangle\langle\psi_0|$ at stroboscopic times $t_\nu = \nu T$ with integer ν, which is equal to the squared overlap $|\langle\psi_0|\psi(t_\nu)\rangle|^2$ with the evolved state $|\psi(t_\nu)\rangle$. According to the diagonal ensemble and employing $|n(t_\nu)\rangle = |n(0)\rangle$, the long-time average (indicated by an overbar) over the stroboscopic dynamics of this quantity gives

$$\overline{|\langle\psi_0|\psi(t_\nu)\rangle|^2} = \sum_n |\langle\psi_0|n(0)\rangle|^4 \equiv \text{IPR}. \tag{6.8}$$

This quantity directly corresponds to the inverse participation ratio that quantifies the localization of the ground state $|\psi_0\rangle$ in the basis of the Floquet states. Its inverse, 1/IPR, is a direct measure for the number of Floquet states required to represent $|\psi_0\rangle$. For the non-interacting gas, we find that the desired overlap is given by the fraction of atoms populating the single-particle ground state (i.e. the quasimomentum $k = 0$ mode in the lowest Bloch band), $|\langle\psi_0|\psi(t_\nu)\rangle|^2 = f_0(t_\nu)$. Thus, having relaxed to a quasi-steady state, we have

$$\mathrm{IPR} = \overline{f_0(t_\nu)}, \tag{6.9}$$

so that the measured observable directly quantifies non-ergodicity. For the interacting system, this reasoning can still be applied in the prethermal regime.

6.1.1 Inverse Participation Ratios measure localization

To understand how inverse participation ratios measure localization in a basis, consider a generic system of size N.

If the wavefunction is totally **delocalized** in the position basis, then the wavefunction can be expressed as:

$$\psi(x) = 1/\sqrt{N}. \tag{6.10}$$

The corresponding inverse participation ratio for this state is:

$$\mathrm{IPR} = \sum_x |\psi(x)|^4 = N(N^{-1/2})^4 = 1/N \tag{6.11}$$

The inverse of this number returns the size of the system: N. Colloquially, this means there are roughly N position states participating in the wavefunction.

If the wavefunction is totally **localized** in the position basis, then the wavefunction

can be expressed as:

$$\psi(x) = \delta_{x,x_0}. \tag{6.12}$$

The corresponding inverse participation ratio for this state is:

$$\text{IPR} = \sum_x |\psi(x)|^4 = 1 \tag{6.13}$$

The inverse of the number returns the value 1. Colloquially, this means there is roughly 1 position state participating in the wavefunction.

What this means is that an IPR close to 1 indicates the system is localized in the position basis and an IPR value smaller than 1 means the system has become delocalized in the position basis.

In our experiment, we have the IPR for the initial state expressed in the basis of Floquet states, IPR $\equiv \sum_n |\langle\psi_0|n(0)\rangle|^4$. What this means is that an IPR close to 1 indicates the system is localized in one Floquet state and an IPR value smaller than 1 indicates the system has become delocalized among several or many Floquet states.

6.2 Observation of a Periodic Gibbs Ensemble

An important point about our IPR is that it is computed by considering the periodic Gibbs ensemble of Floquet states. In the absence of interactions, we can theoretically compute what the IPR should be for our system as a function of α and Ω. A plot of this is shown in Figure 6.4A. You'll notice that there is a localization crossover in Floquet space that occurs from the top left of the plot to the bottom right of the plot. In the localized regime, the IPR is roughly 1, indicating there is only 1 Floquet state necessary to represent the initial ground state. In the delocalized regime, the IPR is between 0.14

to 0.2, corresponding to roughly 5 to 7 Floquet states.

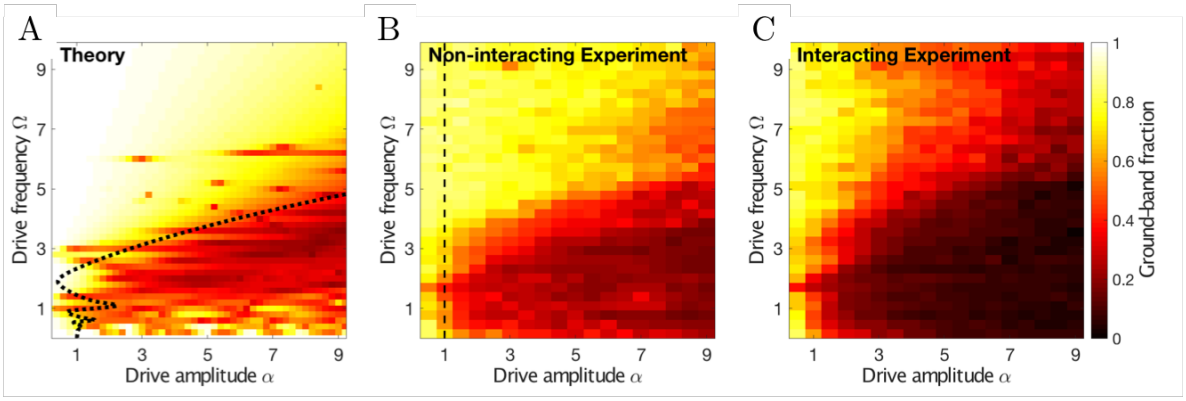

Figure 6.4: Localization diagrams as a function of drive amplitude α and drive frequency Ω. The ground band fraction is a measurement of the inverse participation ratio (IPR) in the basis of Floquet states. In A, the dashed line corresponds to the classical stability boundary of the equivalent driven pendulum (the Kapitza pendulum). The vertical line in B indicates previously explored regions performed with a single lattice (up to $\alpha = 1$). Our double lattice modulation permits us to explore the region for $\alpha > 1$, allowing us to verify a localization to delocalization crossover in Floquet space. Figure is adapted from [21].

There is a straightforward reason that only a finite number of states are expected to be significantly occupied. Since quasimomentum is conserved in the absence of interactions, the single-particle Hamiltonian H of the system can be expressed in terms of states $|m\rangle$ having momentum wave numbers $K_m = (4\pi/\lambda)m$ for integer m. In units of the recoil energy E_R,

$$H = 4\sum_m \left[m^2 |m\rangle\langle m| + \frac{V(t)}{16}\Big(|m+1\rangle\langle m| + |m-1\rangle\langle m| \Big) \right] \tag{6.14}$$

with $V(t) = (V_0/E_R)[1 + \alpha\cos(\omega t)]$. Thus, already for $|m| \simeq 1$, the energy separation $(m+1)^2 - m^2 = 2m + 1$ to higher-lying states becomes larger than the time-dependent coupling matrix elements $V(t)/16$ and the driving frequency. This suggests that the drive will cause substantial redistribution among small m, while for large m the Floquet states will not significantly differ from the undriven eigenstates of the system at large m that

correspond to the scattering continuum. In other words, the ground state of the non-interacting system will mainly overlap with a few Floquet states. The Hamiltonian 6.14 also explains the origin of the crossover to a highly localized regime with f_0 close to one for large frequencies as observed in Figure 6.4. The fact that it couples only neighboring momenta m and $m \pm 1$ shows that (except for narrow resonances) the ground state is predominantly coupled to low energy states, transitions to which become off resonant for large drive frequencies.

Figure 6.4B shows the experimentally measured IPR for the non-interacting case after 500 μs of modulation (much longer than the period of any drive frequency). Here, because of the finite initial spatial extent of the condensate wavefunction, we sum the atom number in the absorption image corresponding to 40% of the first Brillouin zone to extract the zero quasimomentum atoms. We see good agreement between the theory and the experimentally measured data. Figure 6.4C shows the experimentally measured IPR for the strongly-interacting case. We see that the presence of interactions modify, but do not destroy, the Floquet localization map.

What this demonstrates is that the atoms very quickly reach a prethermal plateau characterized by a periodic Gibbs ensemble. In this context, prethermal means that the atoms reach a steady state described by the PGE for an intermediate time prior to heating to infinite temperature at infinite time.

The rapid establishment of the PGE quasi-steady state after the initial quench is expected on theoretical grounds [23]. At any point in drive parameter space, we can measure the approach to the PGE state by observing the full time evolution during the drive. As shown in Figure 6.5A, band-mapping at variable drive time shows a near-immediate approach to the value of f_0 predicted by theory, on a timescale similar to the drive period. The rapid but not instantaneous nature of the dephasing responsible for the emergence of the prethermal plateau can be revealed by measuring a different

observable: the interference patterns after the system is quenched back to a static lattice which is snapped off immediately rather than band-mapped. Figure 6.5B shows that over the course of a few dozen drive cycles, the occupations of the first 2 interference peaks approach their quasi-steady state values.

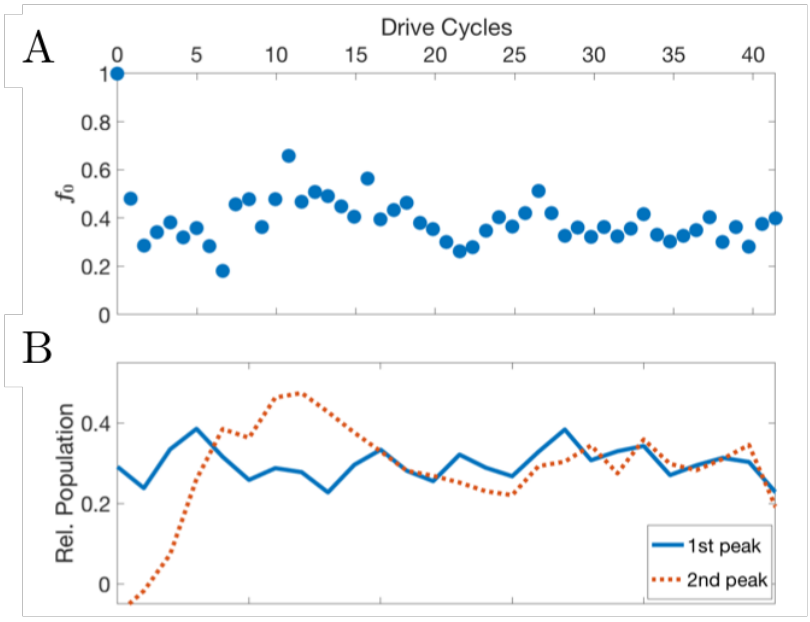

Figure 6.5: Entering the prethermal state (non-interacting data). **A:** Normalized ground band occupation f_0 as a function of time during modulation with $\alpha = 3$, $\Omega = 2.6$, $a = 0$. The system attains the prethermal value of f_0 on time scales comparable to a single drive cycle. **B:** Population fraction in diffracted peaks after diabatic lattice snap-off, as a function of time during the same drive. Gradual attainment of the prethermal steady state is apparent in the increase and settling of the second-peak population. Figure is adapted from [21].

We can perform time trace measurements at any place in the localization map. Figure 6.6 shows short time trace measurements at three places. What we see is that the ground band fraction quickly relaxes to the value as predicted by the PGE within a drive cycle or two. The oscillations around the mean PGE value are a consequence of the small accessible number of single-particle degrees of freedom in the prethermal state (as discussed above) and are qualitatively consistent with predictions from numerical solutions

of the time-dependent Schrödinger equation.

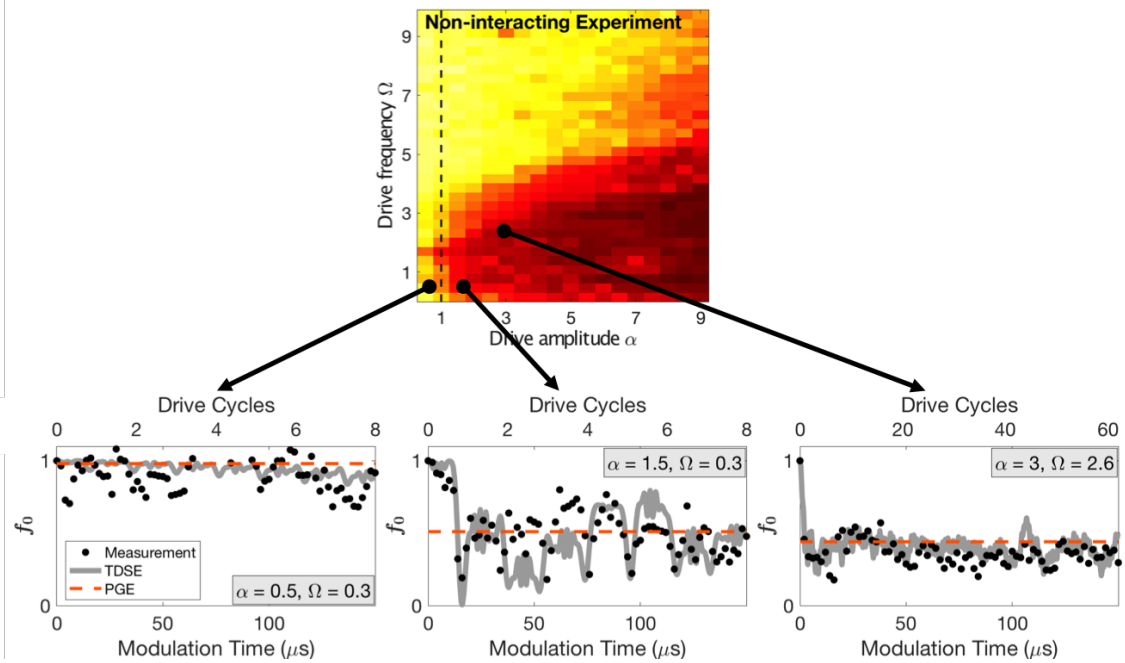

Figure 6.6: Short time traces. The atomic system quickly relaxes to the steady state value predicted by the PGE within several drive cycles. Figure is adapted from [21].

In addition to the ground band atom number fraction, we can also experimentally measure the atom number fraction in all the other bands using band-mapping. A plot of these atom number fractions as a function of α and Ω are shown in the first row of Figure 6.7. Using the periodic Gibbs ensemble, we can theoretically compute the long-time stroboscopic occupation of the other bands as well, shown correspondingly in the bottom row of Figure 6.7. We observe no significant population of atoms in bands higher than the twelfth. These measurements form a complete characterization of the periodic Gibbs ensemble.

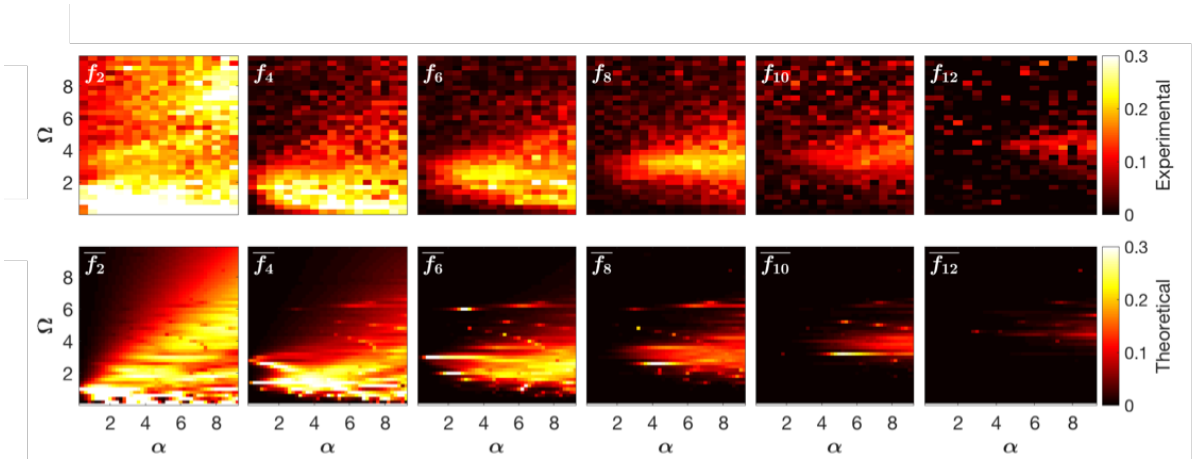

Figure 6.7: Atom number fraction in the higher energy bands. The top row shows the experimentally measurement atom number fraction for even numbered bands up to the twelfth band. The bottom row shows the corresponding quantity computed theoretically from the PGE. These results completely characterize the periodic Gibbs ensemble. Figure is adapted from [21].

6.3 Role of interactions and Floquet Prethermalization

Regardless of the interaction strength, the atomic system first immediately relaxes to the steady state predicted by the periodic Gibbs ensemble as experimentally demonstrated in Figure 6.8. However, the long-time traces demonstrate different behaviors for different scattering lengths (see Figure 6.9). For the non-interacting and moderately interacting scenarios, the atomic system relaxes to a second plateau. This second plateau can be understood as a consequence of a slow spreading in quasimomentum space: as the modulation proceeds, the initial atomic waveplacket spreads in quasimomentum and the selection rules that prohibit odd band occupation are broken. Hence, there are suddenly more states participating and the IPR drops. The strongly interacting samples do not attain the second plateau and instead exhibit ergodicity, decaying to an infinite temperature state with no observable atoms. In this limit, the presence of strong interactions means there are an incredibly large number of accessible states and hence the IPR is close to zero. The observation of decays from the steady state PGE value at different scattering lengths indicate the periodic Gibbs ensemble is indeed a prethermal ensemble, demonstrating Floquet prethermalization.

There have been several theoretical studies of the heating rates in interacting Floquet systems [44, 75, 26, 74, 67]. Experimentally, for these strongly interacting samples, we observe that the prethermal plateau can be regained by increasing the drive frequency. The three panels of Figure 6.10 investigate the long-time evolution of the participation ratio $1/f_0$ for the strongest-interacting samples at various values of the drive frequency Ω. At $\Omega = 2, \alpha = 3$, the observed long-time evolution of $1/f_0$ is consistent with the $\sqrt{t}$ dependence naively expected from Joule heating, and no significant plateau is observed.

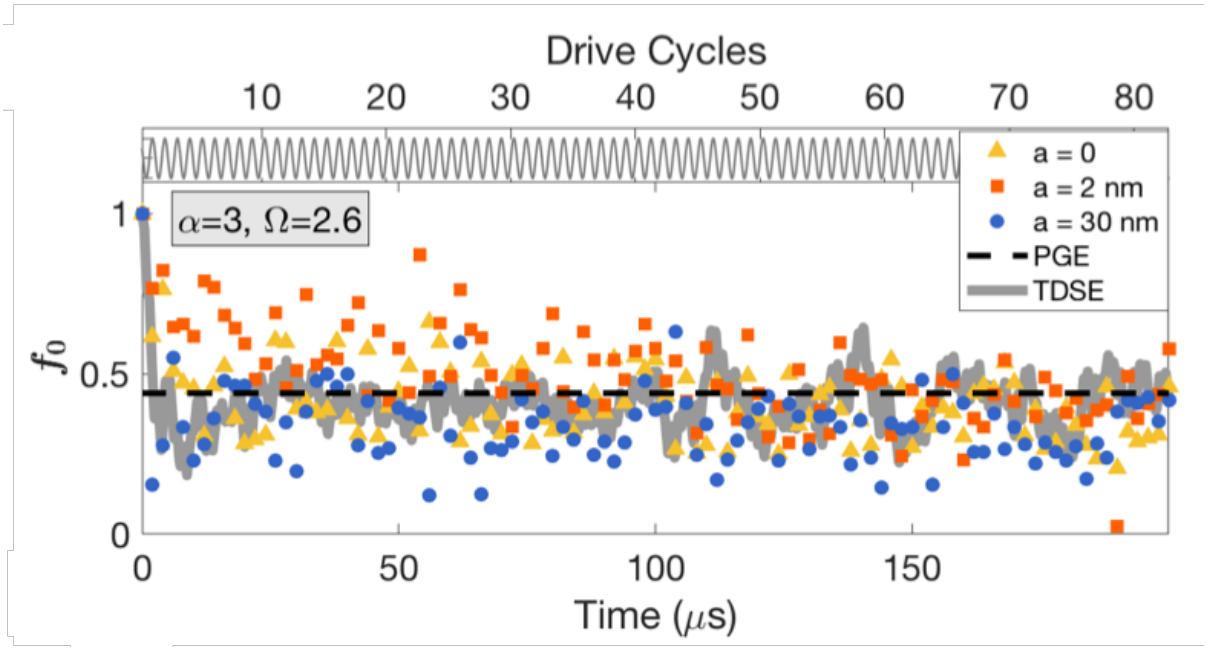

Figure 6.8: Interaction dependence of short-time dynamics for $\Omega = 2.6$ and $\alpha = 3$ at three different values of the s-wave scattering length. Regardless of interaction strength, the system first immediately relaxes to and oscillates near the PGE value. Solid gray line shows the solution to the time-dependent Schrodinger equation for the non-interacting case. Top panel shows the driving waveform. Figure is adapted from [21].

As the drive frequency is increased holding α constant, we observe the emergence of a quasi-static plateau lasting thousands of drive cycles, at a value of f_0 consistent with the PGE prediction. This plateau too eventually decays. Intriguingly, for the highest-frequency drives like the $\Omega = 8$ drive of Figure 6.10, the long-time departure from this plateau is consistent with a $t^{1/4}$ time dependence, and is clearly slower than for the lower drive frequencies. This behavior is consistent with the sub-Joule heating predicted by a recent theoretical analysis of a driven $O(N)$ model [44].

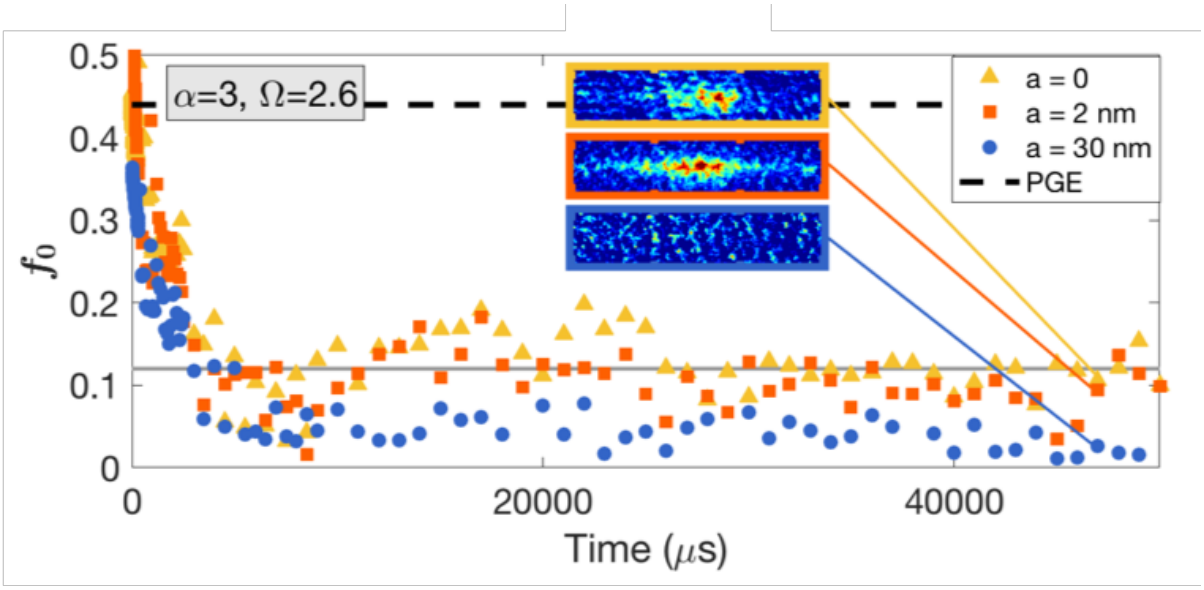

Figure 6.9: Interaction dependence of long-time dynamics for $\Omega = 2.6$ and $\alpha = 3$ at three different values of the s-wave scattering length. Data are boxcar-averaged into 200 μs bins. The non-interacting and moderately interacting samples relax to a secondary plateau below the PGE value. The strongly interacting samples decay to the infinite temperature state. The insets contain band-mapped absorption images at the indicated drives, showing no measurable atoms for the strongest-interacting sample. Figure is adapted from [21].

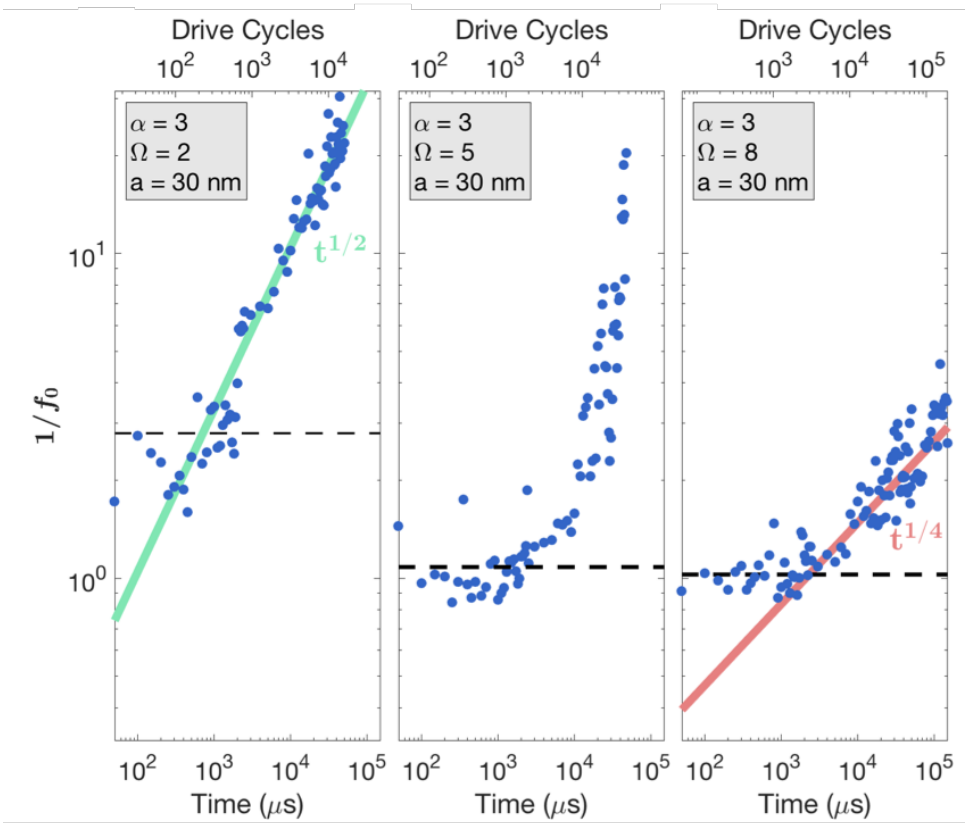

Figure 6.10: Frequency dependence of the long-time traces for strongly interacting samples. We observe that the PGE plateau becomes longer lived with faster drive frequency. Additionally, the departure from the plateau becomes slower for the highest drive frequencies. Figure is adapted from [21].

Chapter 7

Future of the Lithium Experiment

In summary, our experiments demonstrate our ability to controllably manipulate Floquet states. In particular, we have demonstrated tunable coherent control of long-range quantum transport in hybridized Floquet-Bloch bands. We have used hybridization of various pairs of separate static bands at varying quasimomenta to realize rapid long-distance transport of a Bose condensate and direct imaging of a hybrid Floquet-Bloch band. We have experimentally controlled and quantified prethermal localization in a many-body Floquet system. We have observed Floquet prethermalization, a Floquet delocalization crossover which is in quantitative agreement with predictions of a theory based on the periodic Gibbs ensemble, and a long-time transition to ergodicity which depends strongly on drive frequency and interaction strength.

There are numerous exciting future avenues of research for the lithium machine using Floquet engineering. Here are my two favorite ideas that would be realistically achievable with the present version of the machine:

7.1 Kapitza Crystal

As touched upon before, the combined lattice Hamiltonian is the quantum version of the classical Kapitza pendulum (see Figure 7.1). The classical Kapitza pendulum supports a dynamical stability point where the pendulum can be stabilized in the vertically pointing position with the appropriate drive parameters. In the quantum mechanical context, this would mean the atoms would become localized at the time-averaged maxima of the lattice in addition to the time-average minima [81, 82, 83], resulting in a halving of the lattice period. Such a crystal is called a Kapitza crystal and demonstration of it would be a beautiful example of quantum dynamical stability. We have tried experimentally engineering the Kapitza crystal in the laboratory but we have yet to find the appropriate initial wavefunction to prevent significant heating of the atoms as they begin localization at the time-average lattice maxima. Additionally, because we do not have single-site resolution, a new experimental observable is needed to say that the atoms have indeed populated the Kapitza state. I think an appropriate procedure is to first theoretically calculate what the Floquet state that corresponds to the Kapitza crystal is and then look at how it overlaps with the static bands of the lattice at the end of each drive cycle. This would let one do a band-mapping technique and use the distribution of the atoms in the various static bands as a method to reconstruct the time-periodic wavefunction during the modulation.

7.2 Topological Frequency Conversion

There are also many exciting experiment ideas that involve multiple drives at different frequencies (bichromatic or polychromatic driving). A particularly interesting experiment would involve bichromatic driving of the optical lattice where the frequencies of the two

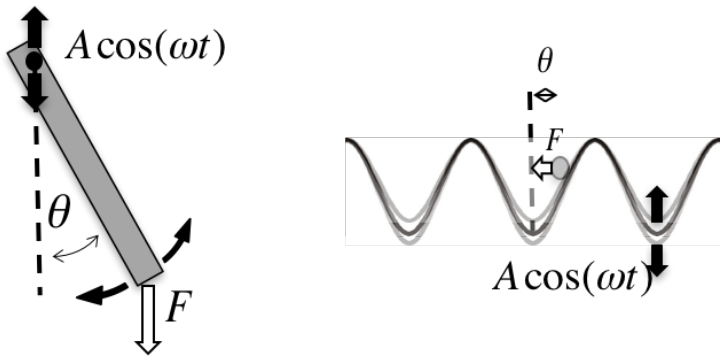

Figure 7.1: The combined amplitude-modulated lattice Hamiltonian is the quantum version of the classical Kapitza pendulum, which supports an inverted stability point.

drives are incommensurate [84]. In such a case, it would be experimentally possible to initialize a specific Floquet band and observe quantized transfer of energy between the two drives by probing the final Floquet state using the atom number distribution in the static bands after band-mapping. This would constitute an experimental analogue of the transverse current in a conventional topological insulator.

Appendix A

Design and Construction of Tapered Amplifiers

I have built five tapered amplifier units in my time as a graduate student: two for 671 nm, two for 689 nm, and one for 915 nm. In this appendix, I will describe in detail how I built the first 671 nm tapered amplifier. The design is essentially the same for all the others. The only difference is that the cylinders that house the input and output lenses are sometimes machined smaller in diameter to sit closer to the tapered amplifier chip for the 689 nm units.

A common complaint among TA designs is that the input and output lens positions are mechanically unstable or shift around in time. For example, having one of the lenses placed on an $x - y - z$ translation stage often causes the position of the lens to shift over the course of hours or days, resulting in poor or unreliable coupling. In this design, the lenses are epoxied directly to an aluminum block that is temperature controlled and holds the TA chip. In doing so, there are no movable parts which in my experience makes for a more reliable tapered amplifier unit.

Here are the steps for assembling the 671nm TA. First acquire the following objects:

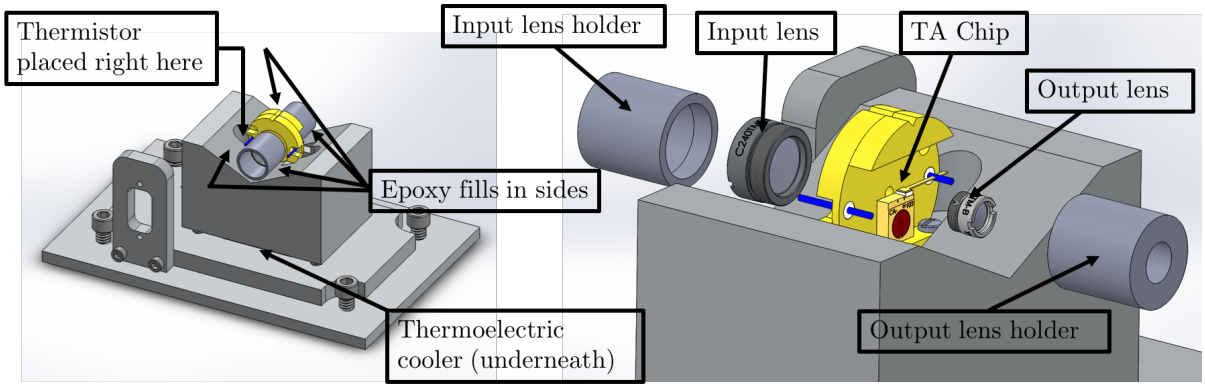

Figure A.1: Diagram of the tapered amplifier.

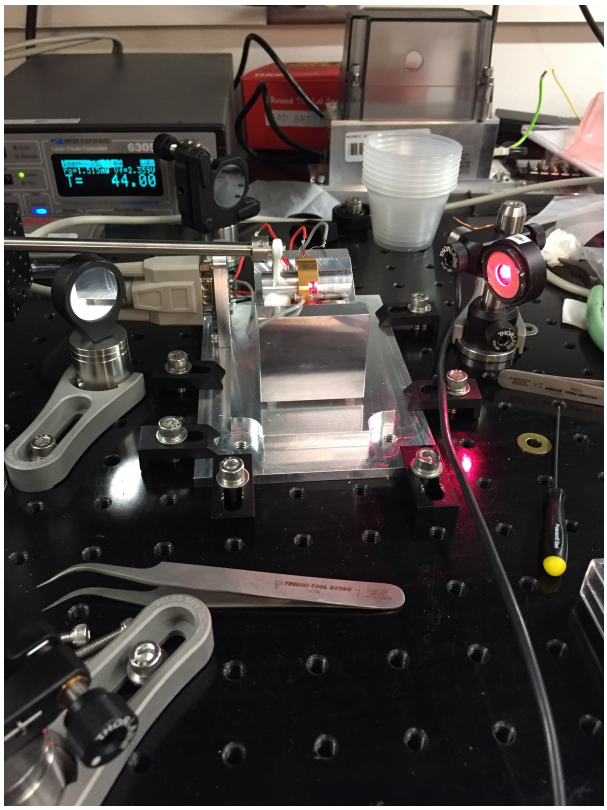

Figure A.2: Picture of the epoxying process. Cylinder-1 is epoxied to a goniometer + translation stage for accurate placement relative to the TA chip. Once the position of the input lens that maximizes output power of the TA chip is found, Cylinder-1 is then epoxied to the vBlock.

TA Chip: EYP-TPA-0670-00500-2003-CMT02-0000 from Eagleyard

Thermoelectric Cooler or Module (TEC): CP10-127-05-L1-W4.5 from Laird

10 kΩ Thermistor: 10K3A1B - Thermistor from Betatherm

Input Aspherical Lens: C240TME-B from Thorlabs

Output Aspherical Lens: N414TM-B from Thorlabs

Current and TEC Controller: 6310 combo source from Arroyo Instruments

Epoxy: Loctite Hysol 1C and Duralco NM25

Thermal paste: Arctic Alumina (or Arctic Silver)

TA Cover: 7360k62 from McMaster-Carr

Free Space Isolator: Thorlabs IO-5-670-VLP

4 Nylon Socket Head Cap Screws, 8-32 Thread, 3/4" Length

Manufacture the following from aluminum:

vBlock (Figure A.4)

basePlate(Figure A.5)

frontPlugInPlate (Figure A.6)

Cylinder-1 (Figure A.7)

Cylinder-2 (Figure A.8)

When assembling the tapered amplifier, the TEC is placed between the vBlock and the basePlate and is covered with Arctic Alumina on both sides of the TEC. Nylon screws are used to connect the vBlock and the basePlate. We use 10 kΩ thermistors instead of AD590s because the thermistor is much more stable against radio frequency radiation. Snugly place the thermistor inside the small hole adjacent to the TA chip location with a slight amount of Loctite Hysol 1C. The front plug-in plate has a DB9 connector port to control the thermistor, TA chip, and TEC. You will need to make the necessary solder connects and purchase the necessary DB connectors in order to control them with the 6310 combo source.

1) Steps to affixing the input lens:

Screw the input lens into Cylinder-1. Cylinder-1 is then lightly epoxied to a goniometer

on a translation stage. Then seed the TA chip with about 15 mW of light and control the angle of the cylinder using the goniometer and the position using the translation stage until maximum power is obtained on the output. When measuring the output power, remember to angle the power meter head to prevent reflected light from damaging the TA chip. The cylinder is then epoxied to the vBlock using Loctite Hysol 1C. In my experience, the best way to do this is to use a syringe and fill in the space underneath the cylinder first. Then fill in any remaining space between the vBlock and the cylinder with NM25.

2) Steps to affixing the output lens:

Screw the output lens into Cylinder-2. Cylinder-2 is then lightly epoxied to a goniometer on a translation state. Use the goniometer and the translation stage to collimate the fast diverging light from the TA Chip. NOTE: The TA chip's output light is astigmatic and diverges at different angles in two orthogonal directions. We use the output aspherical lens to collimate the fast diverging light first, which is the light in the vertical direction. Once the output light looks well collimated in the vertical direction (done using a beam profiler looking at the beam at a distance), the cylinder is epoxied to the vBlock using Loctite Hysol 1C. Then fill in any remaining space between the vBlock and the cylinder with NM25. After the lenses are attached, use a 100 mm focal length cylindrical lens to collimate the light in the horizontal direction. This lens is placed 13.5 cm away from the back edge of the TA chip. Place the isolator after the planoconvex lens to break time reversal symmetry and prevent light from going back and damaging the TA chip. The TA cover is then placed over the top of the whole unit.

To get good coupling of the TA light into a fiber, it is good to use a telescope that magnifies the central mode of the TA output. The typical magnification we use is $M = 4$ constructed from a 50 mm lens and a 200 mm lens.

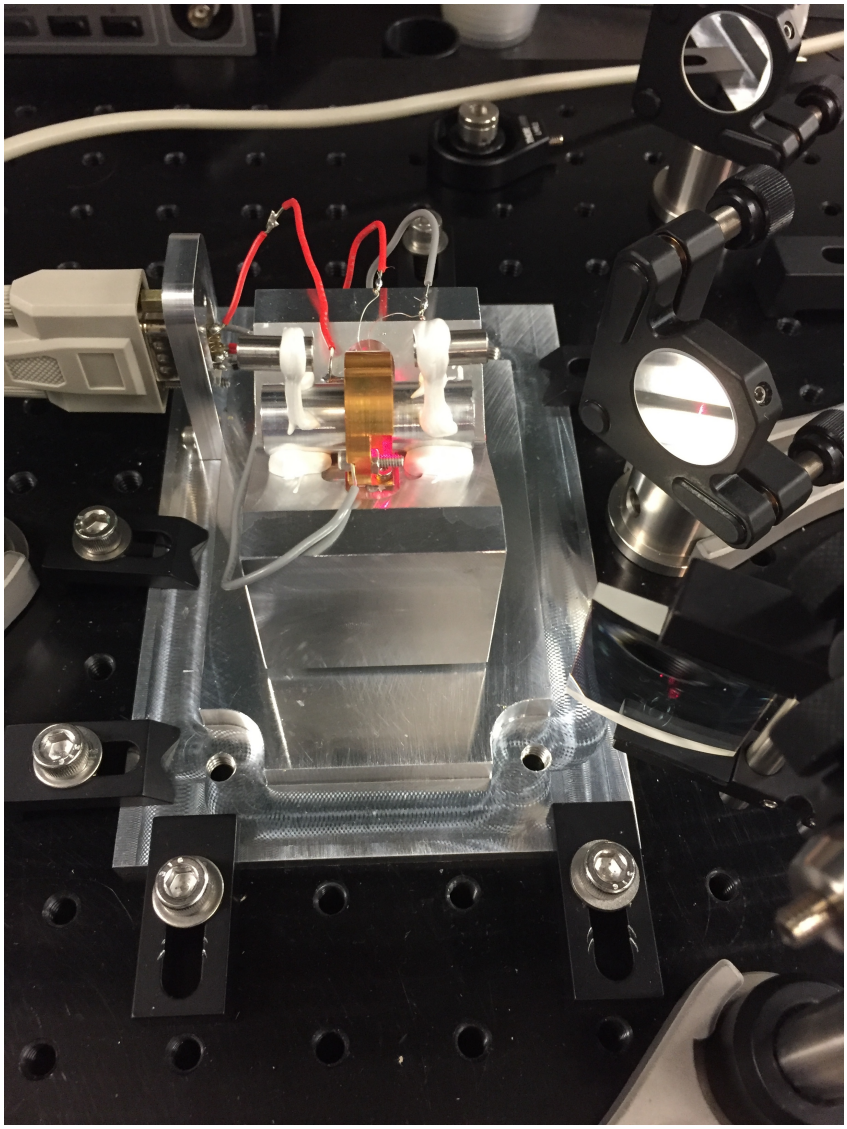

Figure A.3: What the lenses look like after the epoxy application.

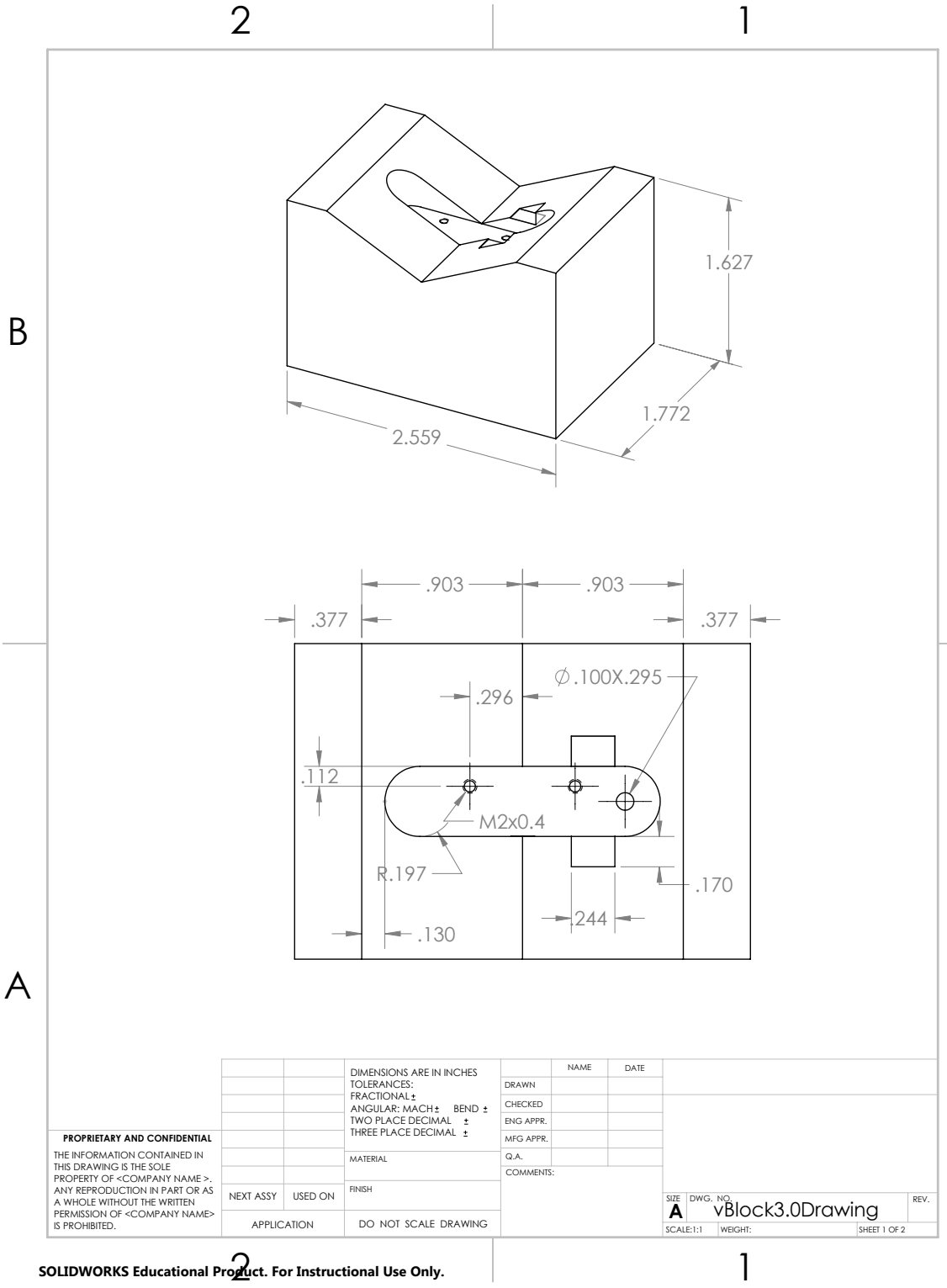

Figure A.4: The vblock.

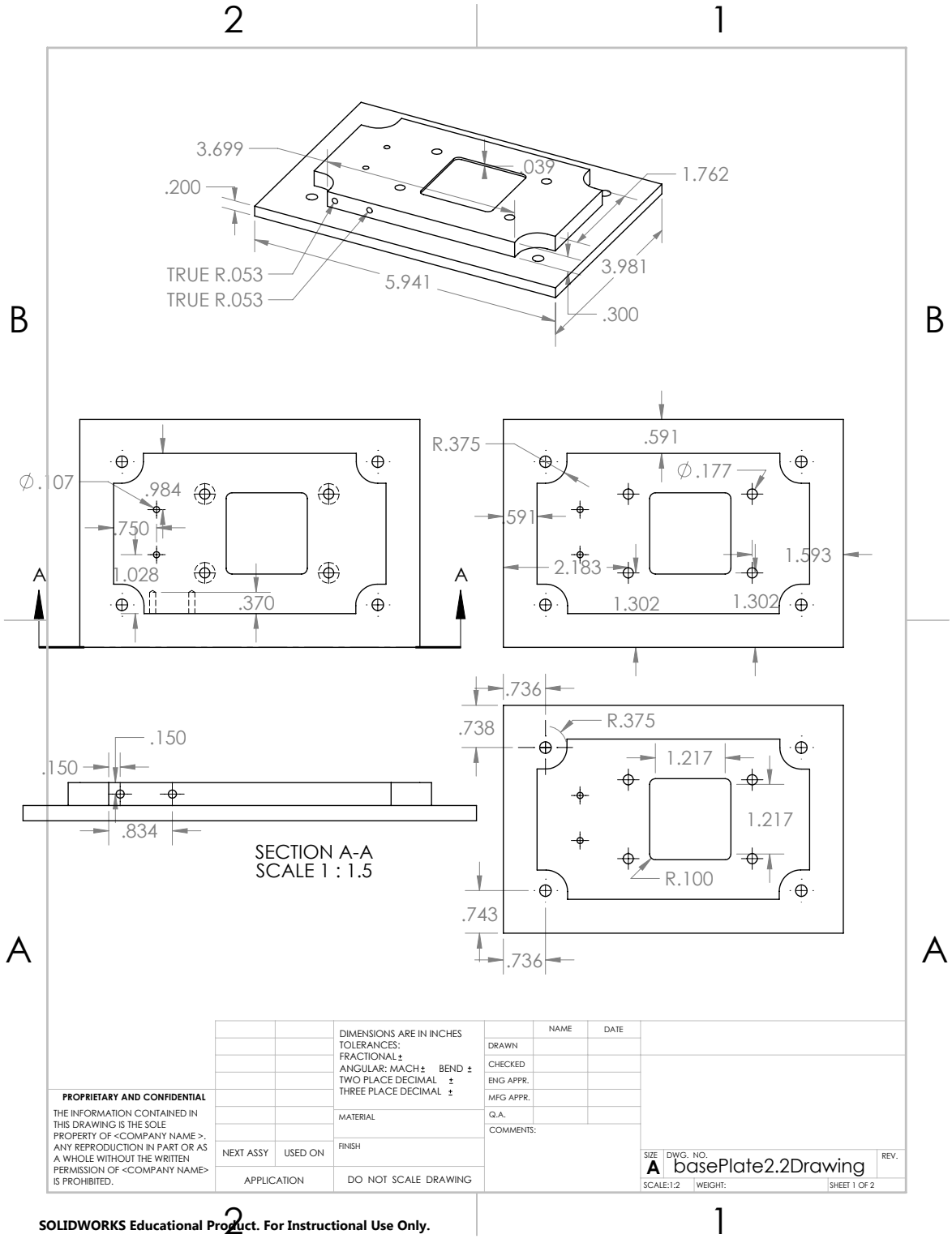

Figure A.5: The baseplate.

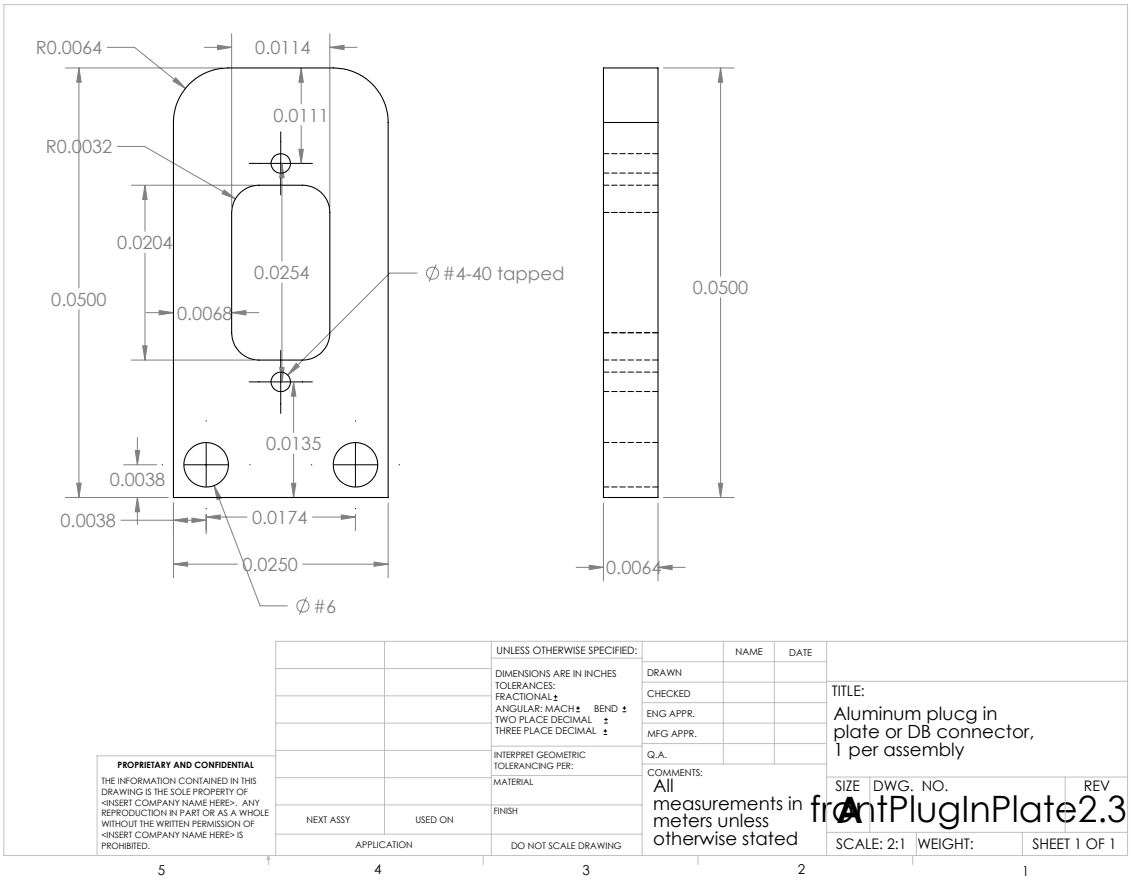

Figure A.6: The front plug-in plate.

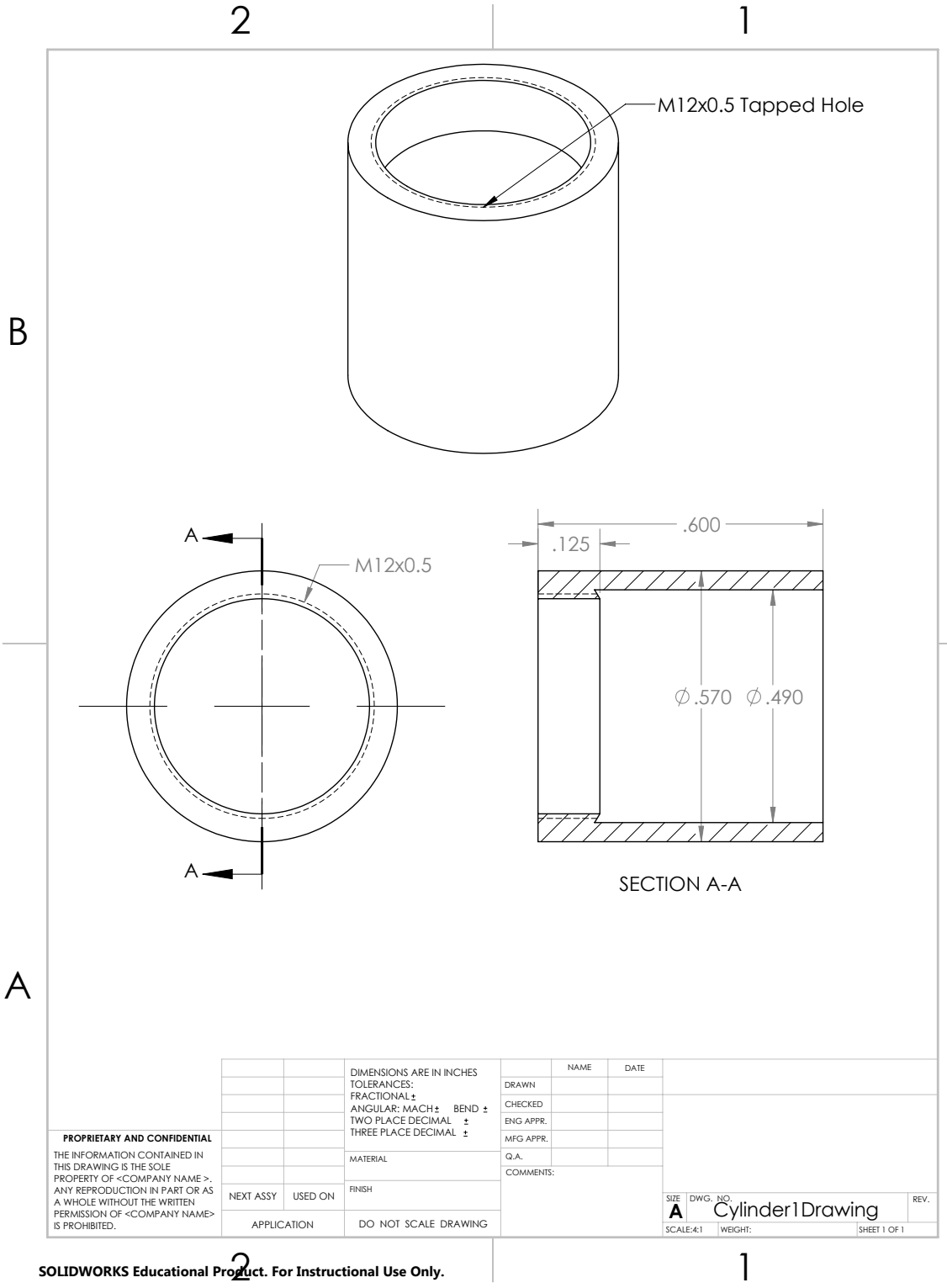

Figure A.7: The input lens holder.

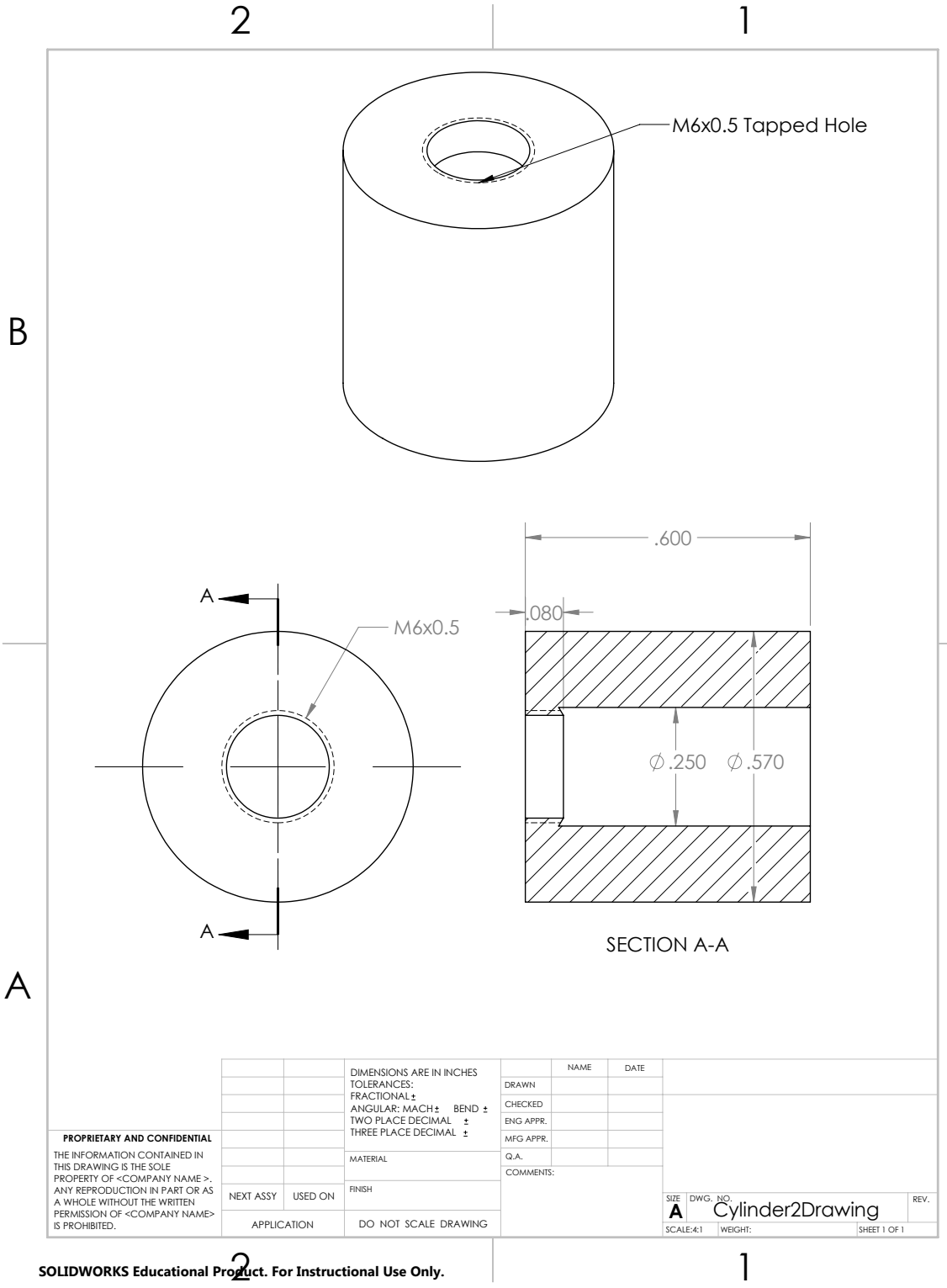

Figure A.8: The output lens holder.

Appendix B

Quasicrystals

Quasicrystals are materials that are ordered, but not periodic. Unlike ordinary crystals, they do not have translational symmetry. Quasicrystals were first discovered by Dan Shechtman and his team while making melt-spun ribbons of a particular Aluminum-Manganese alloy [85]. While performing a diffraction experiment on this material, they discovered a five-fold symmetry, which is crystallographically impossible. The key to understanding this aluminum manganese alloy was with a quasiperiodic tiling of space, which resulted in a paradigm shift with how we understand crystal structure and a Nobel prize for Dan Shechtman.

This quasiperiodicity gives rise to many interesting phenomena not observed in ordinary crystals. For example, quasiperiodic tilings manifest symmetries not possible in ordinary crystals, which leads to unconventional Bragg diffraction patterns. Moreover, just as phonons arise from a breaking of translational symmetry, phasons arise from translations in the higher dimensional periodic lattice in which a quasicrystal exists, giving rise to phasonic excitations in quasiperiodic systems. In addition, quasicrystals support very interesting topological states and exhibit exotic material properties [86]. In particular, applications under investigation include the development of ultra-hard structural

materials, non-stick coatings, and novel thermo-electrics.

Unfortunately, scientists know very little about quasicrystals and these phenomena. This is due to the fact that because quasicrystals do not have translational symmetry, ordinary condensed matter techniques (like Bloch's theorem!) are rendered useless. This means that the key to learning more about quasicrystals lies with experimental investigation.

If we want to make a quasicrystalline lattice for an ultracold atomic system, we have to take a moment to understand the geometric structure of quasicrystals. The central principle to remember is that all quasiperiodic lattices can be thought of as a cut and projection through a higher dimensional periodic lattice [87].

For example, a one-dimensional quasiperiodic lattice can be constructed from a two dimensional square lattice by first cutting out a rectangular strip oriented at an angle α to one of the lattice basis vectors. Once the cut has been made, we then project all of the sites along the rectangular strip to a line parallel to the strip. In order to obtain a quasiperiodic tiling, the cut slope must be irrational. If it is rational, then the resulting lattice will simply be periodic.

A famous example of this cut and project is used to construct the Fibonacci tiling. In particular, if the tangent of the angle α is equal to one over the golden mean (τ), then the resulting spacing between sites will follow the Fibonacci tiling between sites:

$$\tan(\alpha) = 1/\tau \equiv 2/(1+\sqrt{5}), \tag{B.1}$$

$$(1, \tau, \tau 1, \tau 1 \tau \tau 1, \tau 1 \tau \tau 1 \tau 1 \tau, \tau 1 \tau \tau 1 \tau 1 \tau \tau 1 \tau \tau 1 ...). \tag{B.2}$$

What this means is that there will be two fixed distances, labeled 1 and τ, that will tile the line according to the Fibonacci tiling which I have detailed on the second line above. Note that each successive tiling is simply the previous two tiling elements

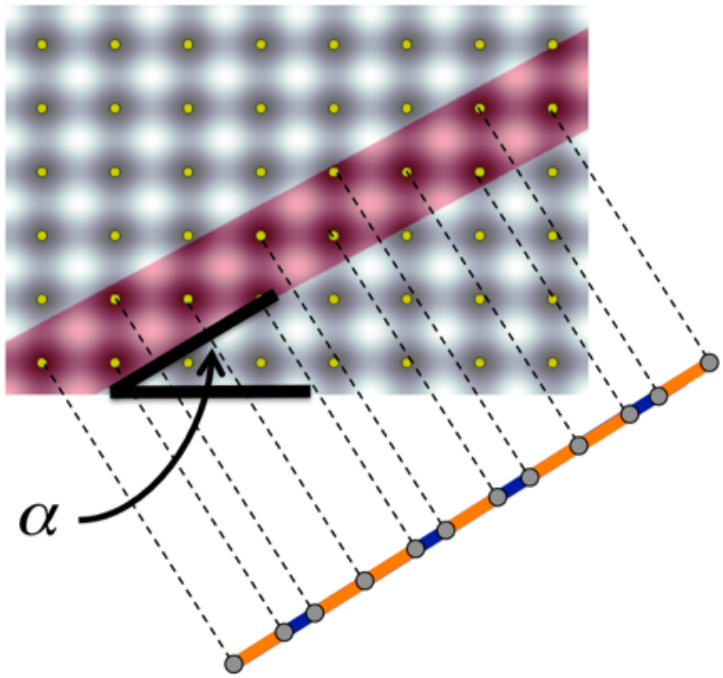

Figure B.1: All quasiperiodic lattice can be created via a "cut-and-project" construction

concatenated together.

The Fibonacci tiling is not the only quasiperiodic tiling you can construct from this method. A quasiperiodic tiling of the line will emerge whenever the cut slope is irrational. This means we can construct a continuous family of quasicrystals by varying the angle α. We refer to this family of quasicrystals as generalized Fibonacci quasicrystals.

A straightforward way to do this cut-and-project construction in the cold atoms context is to take a square optical lattice and intersect it with a red-detuned Gaussian "cutting" beam, as shown in Figure B.2. If $\tan(\alpha) = 1/\tau$, then the minima of this optical potential down the center-line of the optical dipole trap will be spaced according to the Fibonacci tiling, as shown in Figure B.3. A quantum gas loaded into such an optical potential emulates the physics of the Aubrey-André Hamiltonian and has a number of interesting properties, including the ability to pump edge-states via phason driving. These properties are discussed at length in our paper [22].

Experimentally, a convenient way to construct the optical configuration for the cut-and-project construction is to use a square lattice that rotates on top of a static optical dipole trap that already holds a BEC. As a proof of principle, we purchased a 2D grating (MS-203-I-Y-A from Holo/Or) to produce four optical lattice beams that are then focused down by a lens to create a square lattice interference pattern. The grating itself is a circular disk with a 1 inch diameter so that it can be placed in a Thorlabs waveplate rotation mount for easy rotation. Additionally, the grating is optimized to maximize light in the first orders in the x and y directions so that there is minimal light in the $(0, 0)$ or other diffracted modes. The lattice spacing can be controlled by using a larger focusing lens to increase the angle between the beams as they focus onto the atoms. In general, the lattice spacing d between laser beams of wavelength λ with angle θ between them is:

$$d = \frac{\lambda}{2\sin(\theta/2)}. \tag{B.3}$$

Figure B.4 shows measurements of the square lattice resulting from our 2D grating using a 1064 nm seed beam. The lattice spacing here is 15 μm. This square lattice can be installed on the machine by using a telescope to pass a 1064 nm beam through the 2D grating and subsequently focusing the four emerging parallel beams onto the atoms through one of the windows of the main chamber.

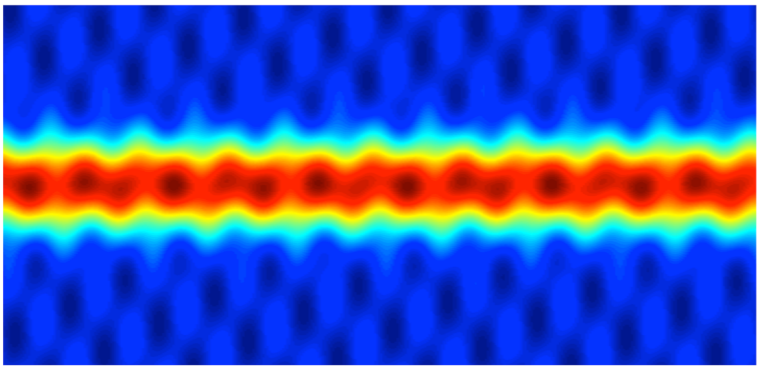

$$V_L(x,y) = -A_L \sin^2\left(\frac{2\pi x}{\lambda_L}\right) - A_L \sin^2\left(\frac{2\pi y}{\lambda_L}\right)$$
$$V_C(x,y) = -A_C \exp\left[-2\left(\frac{-x\sin(\alpha) + y\cos(\alpha)}{\omega_0}\right)^2\right]$$
$$U(x,y) = V_L(x,y) + V_C(x,y,\alpha)$$

Figure B.2: How one can use an optical lattice and an optical dipole trap to create a 1D quasicrystal. V_L is the potential for a square lattice. V_C is the potential for the deep optical dipole trap. $U(x,y)$ is the combined potential, shown in the plot.

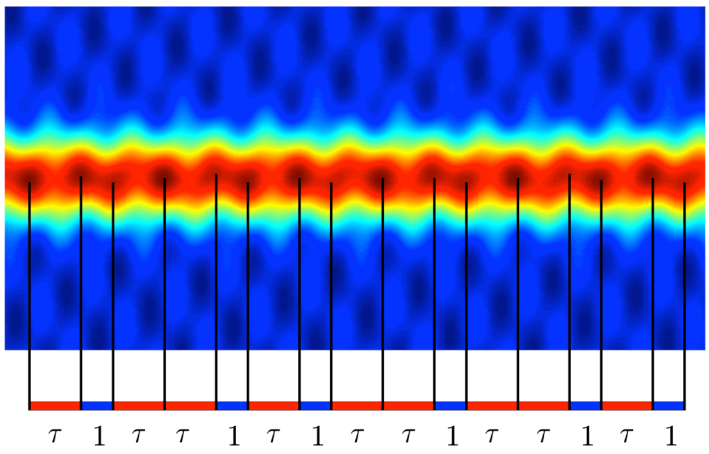

Figure B.3: The spacing of optical lattice minima follow the Fibonacci tiling.

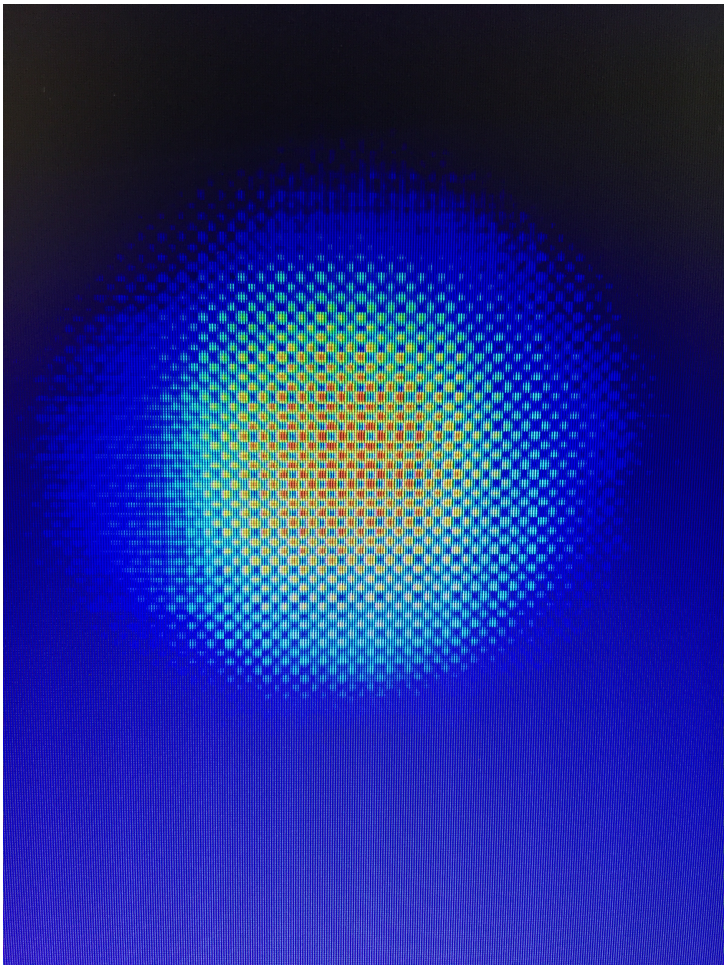

Figure B.4: Picture of the lattice produced from the 2D grating using 1064 nm light and imaged with a beam profiler. Lattice sites are spaced by 15 μm.

Appendix C

Controlling relative spatial phase in the combined lattice

In this appendix, we will use Jones matrices to analyze what happens to the vertical and horizontal components of a laser beam after passing through a quarter waveplate, then a half waveplate and then another quarter waveplate. Let's assume that both of the quarter waveplates have their axis set to 45°.

In the Jones calculus, horizontal polarized light is given by:

$$\mathbf{E}_H = \begin{bmatrix} 1 \\ 0 \end{bmatrix} \tag{C.1}$$

and vertically polarized light is given by:

$$\mathbf{E}_V = \begin{bmatrix} 0 \\ 1 \end{bmatrix}. \tag{C.2}$$

Each waveplate can be thought of as a matrix operator on these initial polarizations.

The effect of a quarter waveplate with the fast axis at 45° is:

$$M_{\lambda/4,45^\circ} = \frac{1}{\sqrt{2}} \begin{bmatrix} 1 & -i \\ -i & 1 \end{bmatrix} \tag{C.3}$$

and the effect of a half waveplate with its fast axis at angle θ with respect to the horizontal axis is:

$$M_{\lambda/2} = \begin{bmatrix} \cos(2\theta) & \sin(2\theta) \\ \sin(2\theta) & -\cos(2\theta) \end{bmatrix}. \tag{C.4}$$

Putting all of this together, we find that the effect of all three waveplates on horizontally polarized light is:

$$M_{\lambda/4,45^\circ} M_{\lambda/2} M_{\lambda/4,45^\circ} \mathbf{E}_H = e^{-2\theta} \mathbf{E}_H \tag{C.5}$$

and that the effect of all three waveplates on vertically polarized light is:

$$M_{\lambda/4,45^\circ} M_{\lambda/2} M_{\lambda/4,45^\circ} \mathbf{E}_V = e^{i(2\theta+\pi)} \mathbf{E}_V \tag{C.6}$$

What we see from the above is that the effect of the half-wave plate is to induce a phase shift of 4θ between the horizontal and vertical components of the electric field. This means a 1° change in the half-waveplate will cause a $4^\circ = 0.02\pi = 0.01\lambda$ relative spatial phase shift (thanks to Peter Dotti for showing me this!). In the experiment, we actually use two quarter waveplates and then retro-reflect the lattice light back through the waveplates. The quarter waveplate closest to the mirror and the mirror reflection work together to effectively act as a single half-waveplate.

Bibliography

[1] P. A. M. Dirac, *The Principles of Quantum Mechanics*. Oxford University Press, 1930.

[2] A. M. Kaufman, B. J. Lester, and C. A. Regal, *Cooling a single atom in an optical tweezer to its quantum ground state*, *Phys. Rev. X* **2** (Nov, 2012) 041014.

[3] M. Endres, H. Bernien, A. Keesling, H. Levine, E. R. Anschuetz, A. Krajenbrink, C. Senko, V. Vuletic, M. Greiner, and M. D. Lukin, *Atom-by-atom assembly of defect-free one-dimensional cold atom arrays*, *Science* **354** (2016), no. 6315 1024–1027, [http://science.sciencemag.org/content/354/6315/1024.full.pdf].

[4] A. E. Leanhardt, T. A. Pasquini, M. Saba, A. Schirotzek, Y. Shin, D. Kielpinski, D. E. Pritchard, and W. Ketterle, *Cooling bose-einstein condensates below 500 picokelvin*, *Science* **301** (2003), no. 5639 1513–1515, [http://science.sciencemag.org/content/301/5639/1513.full.pdf].

[5] C. Chin, R. Grimm, P. Julienne, and E. Tiesinga, *Feshbach resonances in ultracold gases*, *Rev. Mod. Phys.* **82** (Apr, 2010) 1225–1286.

[6] C. Pethick and H. Smith, *Bose-Einstein Condensation in Dilute Gases*. Cambridge University Press, 2002.

[7] H. Friedrich, *Theoretical Atomic Physics*. Springer, Berlin, Heidelberg, 2006.

[8] C. Gross and I. Bloch, *Quantum simulations with ultracold atoms in optical lattices*, *Science* **357** (2017), no. 6355 995–1001, [http://science.sciencemag.org/content/357/6355/995.full.pdf].

[9] A. Eckardt, *Colloquium: Atomic quantum gases in periodically driven optical lattices*, *Rev. Mod. Phys.* **89** (Mar, 2017) 011004.

[10] M. Lewenstein, A. Sanpera, and V. Ahufinger, *Ultracold Atoms in Optical Lattices: Simulating quantum many-body systems*. Oxford University Press, 2012.

[11] M. Greiner, O. Mandel, T. Esslinger, T. W. Hänsch, and I. Bloch, *Quantum phase transition from a superfluid to a mott insulator in a gas of ultracold atoms*, *Nature* **415** (01, 2002) 39.

[12] M. Schreiber, S. S. Hodgman, P. Bordia, H. P. Lüschen, M. H. Fischer, R. Vosk, E. Altman, U. Schneider, and I. Bloch, *Observation of many-body localization of interacting fermions in a quasirandom optical lattice*, *Science* **349** (2015), no. 6250 842–845, [http://science.sciencemag.org/content/349/6250/842.full.pdf].

[13] W. S. Bakr, J. I. Gillen, A. Peng, S. Fölling, and M. Greiner, *A quantum gas microscope for detecting single atoms in a hubbard-regime optical lattice*, *Nature* **462** (11, 2009) 74.

[14] L. W. Cheuk, M. A. Nichols, M. Okan, T. Gersdorf, V. V. Ramasesh, W. S. Bakr, T. Lompe, and M. W. Zwierlein, *Quantum-gas microscope for fermionic atoms*, *Phys. Rev. Lett.* **114** (May, 2015) 193001.

[15] M. H. Anderson, J. R. Ensher, M. R. Matthews, C. E. Wieman, and E. A. Cornell, *Observation of bose-einstein condensation in a dilute atomic vapor*, *Science* **269** (1995), no. 5221 198–201, [http://science.sciencemag.org/content/269/5221/198.full.pdf].

[16] K. B. Davis, M. O. Mewes, M. R. Andrews, N. J. van Druten, D. S. Durfee, D. M. Kurn, and W. Ketterle, *Bose-einstein condensation in a gas of sodium atoms*, *Phys. Rev. Lett.* **75** (Nov, 1995) 3969–3973.

[17] C. C. Bradley, C. A. Sackett, and R. G. Hulet, *Bose-einstein condensation of lithium: Observation of limited condensate number*, *Phys. Rev. Lett.* **78** (Feb, 1997) 985–989.

[18] S. E. Pollack, D. Dries, M. Junker, Y. P. Chen, T. A. Corcovilos, and R. G. Hulet, *Extreme tunability of interactions in a* ^{7}Li *bose-einstein condensate*, *Phys. Rev. Lett.* **102** (Mar, 2009) 090402.

[19] Z. A. Geiger, K. M. Fujiwara, K. Singh, R. Senaratne, S. V. Rajagopal, M. Lipatov, T. Shimasaki, R. Driben, V. V. Konotop, T. Meier, and D. M. Weld, *Observation and uses of position-space bloch oscillations in an ultracold gas*, *Phys. Rev. Lett.* **120** (May, 2018) 213201.

[20] C. J. Fujiwara, K. Singh, Z. A. Geiger, R. Senaratne, S. V. Rajagopal, M. Lipatov, and D. M. Weld, *Transport in floquet-bloch bands*, *Phys. Rev. Lett.* **122** (Jan, 2019) 010402.

[21] K. Singh, K. M. Fujiwara, Z. A. Geiger, E. Q. Simmons, M. Lipatov, A. Cao, P. Dotti, S. V. Rajagopal, R. Senaratne, T. Shimasaki, M. Heyl, A. Eckardt, and D. M. Weld, *Controlling and characterizing floquet prethermalization in a driven quantum system*, (2018) https://arxiv.org/abs/1809.05554.

[22] K. Singh, K. Saha, S. A. Parameswaran, and D. M. Weld, *Fibonacci optical lattices for tunable quantum quasicrystals*, *Phys. Rev. A* **92** (Dec, 2015) 063426.

[23] A. Lazarides, A. Das, and R. Moessner, *Periodic thermodynamics of isolated quantum systems*, *Phys. Rev. Lett.* **112** (Apr, 2014) 150401.

[24] M. Kardar, *Statistical Physics of Particles*. Cambridge University Press, 2007.

[25] A. L. Fetter and J. D. Walecka, *Quantum Theory of Many-Particle Systems*. Dover, 2003.

[26] T. Mori, T. N. Ikeda, E. Kaminishi, and M. Ueda, *Thermalization and prethermalization in isolated quantum systems: a theoretical overview*, *Journal of Physics B: Atomic, Molecular and Optical Physics* **51** (2018), no. 11 112001.

[27] T. Langen, T. Gasenzer, and J. Schmiedmayer, *Prethermalization and universal dynamics in near-integrable quantum systems*, *Journal of Statistical Mechanics: Theory and Experiment* **2016** (2016), no. 6 064009.

[28] M. Rigol, V. Dunjko, V. Yurovsky, and M. Olshanii, *Relaxation in a completely integrable many-body quantum system: An ab initio study of the dynamics of the highly excited states of 1d lattice hard-core bosons*, *Phys. Rev. Lett.* **98** (Feb, 2007) 050405.

[29] A. C. Cassidy, C. W. Clark, and M. Rigol, *Generalized thermalization in an integrable lattice system*, *Phys. Rev. Lett.* **106** (Apr, 2011) 140405.

[30] T. Barthel and U. Schollwöck, *Dephasing and the steady state in quantum many-particle systems*, *Phys. Rev. Lett.* **100** (Mar, 2008) 100601.

[31] M. Kollar, F. A. Wolf, and M. Eckstein, *Generalized gibbs ensemble prediction of prethermalization plateaus and their relation to nonthermal steady states in integrable systems*, *Phys. Rev. B* **84** (Aug, 2011) 054304.

[32] T. Kinoshita, T. Wenger, and D. S. Weiss, *A quantum newton's cradle*, *Nature* **440** (04, 2006) 900.

[33] M. Gring, M. Kuhnert, T. Langen, T. Kitagawa, B. Rauer, M. Schreitl, I. Mazets, D. A. Smith, E. Demler, and J. Schmiedmayer, *Relaxation and prethermalization in an isolated quantum system*, *Science* **337** (2012), no. 6100 1318–1322, [http://science.sciencemag.org/content/337/6100/1318.full.pdf].

[34] Y. Tang, W. Kao, K.-Y. Li, S. Seo, K. Mallayya, M. Rigol, S. Gopalakrishnan, and B. L. Lev, *Thermalization near integrability in a dipolar quantum newton's cradle*, *Phys. Rev. X* **8** (May, 2018) 021030.

[35] B. Neyenhuis, J. Zhang, P. W. Hess, J. Smith, A. C. Lee, P. Richerme, Z.-X. Gong, A. V. Gorshkov, and C. Monroe, *Observation of prethermalization in long-range interacting spin chains*, *Science Advances* **3** (2017), no. 8 [http://advances.sciencemag.org/content/3/8/e1700672.full.pdf].

[36] R. Vosk and E. Altman, *Many-body localization in one dimension as a dynamical renormalization group fixed point*, *Phys. Rev. Lett.* **110** (Feb, 2013) 067204.

[37] C. Gogolin, M. P. Müller, and J. Eisert, *Absence of thermalization in nonintegrable systems*, *Phys. Rev. Lett.* **106** (Jan, 2011) 040401.

[38] F. Alet and N. Laflorencie, *Many-body localization: Introduction and selected topics*, *C.R. Physique* **19** (2018) 498–525.

[39] R. Moessner and S. L. Sondhi, *Equilibration and order in quantum floquet matter*, *Nat. Phys.* **13** (04, 2017) 424.

[40] A. Lazarides, A. Das, and R. Moessner, *Equilibrium states of generic quantum systems subject to periodic driving*, *Phys. Rev. E* **90** (Jul, 2014) 012110.

[41] A. Russomanno, A. Silva, and G. E. Santoro, *Periodic steady regime and interference in a periodically driven quantum system*, *Phys. Rev. Lett.* **109** (12, 2012) 257201.

[42] M. Holthaus, *Floquet engineering with quasienergy bands of periodically driven optical lattices*, *Journal of Physics B: Atomic, Molecular and Optical Physics* **49** (2016), no. 1 013001.

[43] P. Bordia, H. Lüschen, U. Schneider, M. Knap, and I. Bloch, *Periodically driving a many-body localized quantum system*, *Nat. Phys.* **13** (01, 2017) 460.

[44] S. A. Weidinger and M. Knap, *Floquet prethermalization and regimes of heating in a periodically driven, interacting quantum system*, *Sci. Rep.* **7** (Apr, 2017) 45382.

[45] C. J. Sansonetti, C. E. Simien, J. D. Gillaspy, J. N. Tan, S. M. Brewer, R. C. Brown, S. Wu, and J. V. Porto, *Absolute transition frequencies and quantum interference in a frequency comb based measurement of the* ^{6,7}Li *d lines*, *Phys. Rev. Lett.* **107** (Jul, 2011) 023001.

[46] F. Schreck., *Mixtures of ultracold gases: Fermi sea and bose-einstein condensate of lithium isotopes*, *Ph.D. Thesis, Universite Pierre et Marie Curie - Paris VI* (2002).

[47] C. J. Foot, *Atomic physics*. Oxford University Press, 2005.

[48] A. T. Grier, I. Ferrier-Barbut, B. S. Rem, M. Delehaye, L. Khaykovich, F. Chevy, and C. Salomon, Λ*-enhanced sub-doppler cooling of lithium atoms in* D_1 *gray molasses*, *Phys. Rev. A* **87** (Jun, 2013) 063411.

[49] M. Lara, B. L. Lev, and J. L. Bohn, *Loss of molecules in magneto-electrostatic traps due to nonadiabatic transitions*, *Phys. Rev. A* **78** (Sep, 2008) 033433.

[50] R. Senaratne, S. V. Rajagopal, Z. A. Geiger, K. M. Fujiwara, V. Lebedev, and D. M. Weld, *Effusive atomic oven nozzle design using an aligned microcapillary array*, *Review of Scientific Instruments* **86** (2015), no. 2 023105, [https://doi.org/10.1063/1.4907401].

[51] D. McKay, M. White, and B. DeMarco, *Lattice thermodynamics for ultracold atoms*, *Phys. Rev. A* **79** (06, 2009) 063605.

[52] B. Gadway, D. Pertot, R. Reimann, M. G. Cohen, and D. Schneble, *Analysis of kapitza-dirac diffraction patterns beyond the raman-nath regime*, *Opt. Express* **17** (Oct, 2009) 19173–19180.

[53] T. Hartmann, F. Keck, H. J. Korsch, and S. Mossmann, *Dynamics of bloch oscillations*, *New Journal of Physics* **6** (2004), no. 1 2.

[54] Z. Geiger, *An apparatus for dynamical quantum emulation using ultracold lithium*, *Ph.D. Thesis, UC Santa Barbara* (2017).

[55] K. M. Fujiwara, Z. A. Geiger, K. Singh, R. Senaratne, S. V. Rajagopal, M. Lipatov, T. Shimasaki, and D. M. Weld, *Experimental realization of a relativistic harmonic oscillator*, *New Journal of Physics* **20** (2018), no. 6 063027.

[56] J. Zhang, P. W. Hess, A. Kyprianidis, P. Becker, A. Lee, J. Smith, G. Pagano, I.-D. Potirniche, A. C. Potter, A. Vishwanath, N. Y. Yao, and C. Monroe, *Observation of a discrete time crystal*, *Nature* **543** (03, 2017) 217–220.

[57] S. Choi, J. Choi, R. Landig, G. Kucsko, H. Zhou, J. Isoya, F. Jelezko, S. Onoda, H. Sumiya, V. Khemani, C. von Keyserlingk, N. Y. Yao, E. Demler, and M. D. Lukin, *Observation of discrete time-crystalline order in a disordered dipolar many-body system*, *Nature* **543** (03, 2017) 221–225.

[58] A. Eckardt, *Colloquium: Atomic quantum gases in periodically driven optical lattices*, *Reviews of Modern Physics* **89** (03, 2017) 011004.

[59] P. Roushan, C. Neill, A. Megrant, Y. Chen, R. Babbush, R. Barends, B. Campbell, Z. Chen, B. Chiaro, A. Dunsworth, A. Fowler, E. Jeffrey, J. Kelly, E. Lucero, J. Mutus, P. J. J. O'Malley, M. Neeley, C. Quintana, D. Sank, A. Vainsencher, J. Wenner, T. White, E. Kapit, H. Neven, and J. Martinis, *Chiral ground-state currents of interacting photons in a synthetic magnetic field*, *Nat. Phys.* **13** (10, 2016) 146.

[60] N. Fläschner, B. S. Rem, M. Tarnowski, D. Vogel, D. S. Lühmann, K. Sengstock, and C. Weitenberg, *Experimental reconstruction of the berry curvature in a floquet bloch band*, *Science* **352** (05, 2016) 1091.

[61] G. Jotzu, M. Messer, R. Desbuquois, M. Lebrat, T. Uehlinger, D. Greif, and T. Esslinger, *Experimental realization of the topological haldane model with ultracold fermions*, *Nature* **515** (11, 2014) 237.

[62] M. Aidelsburger, M. Lohse, C. Schweizer, M. Atala, J. T. Barreiro, S. Nascimbène, N. R. Cooper, I. Bloch, and N. Goldman, *Measuring the chern number of hofstadter bands with ultracold bosonic atoms*, *Nat. Phys.* **11** (12, 2014) 162.

[63] M. C. Rechtsman, J. M. Zeuner, Y. Plotnik, Y. Lumer, D. Podolsky, F. Dreisow, S. Nolte, M. Segev, and A. Szameit, *Photonic floquet topological insulators*, *Nature* **496** (04, 2013) 196.

[64] T. Kuwahara, T. Mori, and K. Saito, *Floquet–magnus theory and generic transient dynamics in periodically driven many-body quantum systems*, *Annals of Physics* **367** (2016) 96 – 124.

[65] D. A. Abanin, W. De Roeck, and F. Huveneers, *Exponentially slow heating in periodically driven many-body systems*, *Phys. Rev. Lett.* **115** (12, 2015) 256803.

[66] D. A. Abanin, W. De Roeck, W. W. Ho, and F. Huveneers, *Effective hamiltonians, prethermalization, and slow energy absorption in periodically driven many-body systems*, *Phys. Rev. B* **95** (01, 2017) 014112.

[67] F. Machado, G. D. Meyer, D. V. Else, C. Nayak, and N. Y. Yao, (2017) https://arxiv.org/abs/1708.01620.

[68] J. Berges, S. Borsányi, and C. Wetterich, *Prethermalization*, *Physical Review Letters* **93** (2004), no. 14 142002.

[69] M. Moeckel and S. Kehrein, *Interaction Quench in the Hubbard model*, *Phys. Rev. Lett.* **100** (2008) 175702.

[70] M. Rigol, V. Dunjko, V. Yurovsky, and M. Olshanii, *Relaxation in a completely integrable many-body Quantum system: An Ab initio study of the dynamics of the highly excited states of 1D lattice hard-core bosons*, *Physical Review Letters* **98** (2007), no. 5 50404–50405.

[71] A. Polkovnikov, K. Sengupta, A. Silva, and M. Vengalattore, *Nonequilibrium dynamics of closed interacting quantum systems*, *Rev. Mod. Phys.* **83** (2011) 1–23.

[72] T. Langen, S. Erne, R. Geiger, B. Rauer, T. Schweigler, M. Kuhnert, W. Rohringer, I. E. Mazets, T. Gasenzer, and J. Schmiedmayer, *Experimental observation of a generalized gibbs ensemble*, *Science* **348** (2015), no. 6231 207–211, [http://science.sciencemag.org/content/348/6231/207.full.pdf].

[73] Y. Tang, W. Kao, K.-Y. Li, S. Seo, K. Mallayya, M. Rigol, S. Gopalakrishnan, and B. L. Lev, *Thermalization near integrability in a dipolar quantum newton's cradle*, *Phys. Rev. X* **8** (05, 2018) 021030.

[74] E. Canovi, M. Kollar, and M. Eckstein, *Stroboscopic prethermalization in weakly interacting periodically driven systems*, *Phys. Rev. E* **93** (Jan, 2016) 012130.

[75] M. Bukov, S. Gopalakrishnan, M. Knap, and E. Demler, *Prethermal floquet steady states and instabilities in the periodically driven, weakly interacting bose-hubbard model*, *Phys Rev Lett* **115** (11, 2015).

[76] M. Reitter, J. Näger, K. Wintersperger, C. Sträter, I. Bloch, A. Eckardt, and U. Schneider, *Interaction dependent heating and atom loss in a periodically driven optical lattice*, *Phys. Rev. Lett.* **119** (11, 2017) 200402.

[77] M. Messer, K. Sandholzer, F. Görg, J. Minguzzi, R. Desbuquois, and T. Esslinger, *Floquet dynamics in driven fermi-hubbard systems*, *Phys. Rev. Lett.* **121** (Dec, 2018) 233603.

[78] J. Nager, K. Wintersperger, M. Bukov, S. Lellouch, E. Demler, U. Schneider, I. Bloch, N. Goldman, and M. Aidelsburger, *Parametric instabilities of interacting bosons in periodically-driven 1d optical lattices*, (2018) https://arxiv.org/abs/1808.07462.

[79] M. Weinberg, C. Ölschläger, C. Sträter, S. Prelle, A. Eckardt, K. Sengstock, and J. Simonet, *Multiphoton interband excitations of quantum gases in driven optical lattices*, *Phys. Rev. A* **92** (Oct, 2015) 043621.

[80] C. Strater and A. Eckardt, *Interband Heating Processes in a Periodically Driven Optical Lattice*, *Zeitschrift fr Naturforschung* **71** (2016) 909–920.

[81] J. Martin, B. Georgeot, D. Guéry-Odelin, and D. L. Shepelyansky, *Kapitza stabilization of a repulsive bose-einstein condensate in an oscillating optical lattice*, *Phys. Rev. A* **97** (Feb, 2018) 023607.

[82] R. Citro, E. G. D. Torre, L. D'Alessio, A. Polkovnikov, M. Babadi, T. Oka, and E. Demler, *Dynamical stability of a many-body kapitza pendulum*, *Annals of Physics* **360** (2015) 694 – 710.

[83] I. Gilary, N. Moiseyev, S. Rahav, and S. Fishman, *Trapping of particles by lasers: the quantum kapitza pendulum*, *Journal of Physics A: Mathematical and General* **36** (2003), no. 25 L409.

[84] I. Martin, G. Refael, and B. Halperin, *Topological frequency conversion in strongly driven quantum systems*, *Phys. Rev. X* **7** (Oct, 2017) 041008.

[85] D. Shechtman, I. Blech, D. Gratias, and J. W. Cahn, *Metallic phase with long-range orientational order and no translational symmetry*, *Phys. Rev. Lett.* **53** (Nov, 1984) 1951–1953.

[86] Y. E. Kraus, Y. Lahini, Z. Ringel, M. Verbin, and O. Zilberberg, *Topological states and adiabatic pumping in quasicrystals*, *Phys. Rev. Lett.* **109** (Sep, 2012) 106402.

[87] M. P. Marder, *Condensed Matter Physics*. John Wiley and Sons, Inc, 2010.